学位論文

Response of tropical cyclone structure to a global warming using a high-resolution global nonhydrostatic model

（高解像度全球非静力学モデルを用いた熱帯低気圧の温暖化による構造変化に関する研究）

平成 27 年 7 月博士（理学）申請

東京大学大学院理学系研究科

地球惑星科学専攻 山田 洋平

Abstract

Atmospheric general circulation models (AGCMs) predict reductions in global tropical cyclone (TC) frequency along with increases in genesis rate of intense TCs relative to total TCs. Because computational resources restricted high-resolution simulation using AGCMs, many previous studies have not discussed future changes in elements of TC structure such as the radius of maximum wind (RMW). A regional circulation model predicted that RMW decreases under warmer climates. This model simulated a small number of TCs and a large difference between the mean intensities of present-day and future TCs. Observational studies indicated that RMW varies from TC to TC and slightly depends on TC intensity.

Herein, the response of TC structure to global warming is statistically investigated for TCs with the same intensities in different climate conditions. Many samples were required to complete this effort. Due to the development of supercomputers, the present-day and global warming simulations were conducted using a Nonhydrostatic ICosahedral Atmospheric Model (NICAM) without a cumulus convection scheme. The simulation span was more than 30 years, and the horizontal grid interval was 14 km. The model output was useful to investigate future changes in TC structure.

To discuss future changes in TC structure, the model needs to reproduce characteristics of TC structure, such as the TC primary and secondary circulations and the outward slope of TC eyewall. NICAM accurately reproduces the TC primary and secondary circulations, particularly the updrafts along the outward slope of the eyewall slope with height in intense TCs, as reported in observational studies.

Simulations (14 km) have predicted that TCs in the same sea-level pressure (SLP) have higher eyewall, water contents, and greater RMWs under warmer climate conditions. Moreover, their swirling flows increase outside the eyewalls and decrease inside. An elevation of tropopause height extends the top of eyewall. TCs contain more water contents due to the vertical extent of eyewall. Unfortunately, the future changes in RMW could not be predicted because the changes are not statistically significant, and the 7-km simulation predicts the opposite change as the 14-km simulation. However, the increases in the swirling flows outside the eyewall appear to be a robust response, with both 14- and 7-km simulations predicting the same signal. The Sawyer–Eliassen model supports this finding.

The increases in the swirling flows are related to the elevation of the tropopause caused by global warming. The rising tropopause induces an upward extension of the eyewall cloud, consequently increasing diabatic heating. Thus, the air is warmed, and the SLP is reduced underneath the warmed area. This mechanism is called hydrostatic adjustment. The altered distribution of SLP enhances the tangential wind under and outward of the eyewall cloud. The outward slope of the updrafts with height plays an important role in this mechanism.

Table of contents

Chapter 1 General Introduction

Tropical cyclones (TCs) form over warm tropical oceans, and their primary energy source is heat derived from the ocean (Emanuel 2003). It is reasonable to expect that global warming might influence TC activities. TCs cause severe natural disasters, and the scale of damage is modulated by the frequency, intensity, and horizontal size of the TC. To reduce the damages caused by TCs, it is important to understand how global warming influences TC activities.

1.1 Tropical cyclones and global warming

Broccoli and Manabe (1990) applied a general circulation model (GCM) with grid spacing of a few hundred kilometers to estimate the effects of global warming on the frequency of TC formation for the first time. They suggested that GCMs with finer resolutions are appropriate tools for understanding the relationship between global warming and TC activity. Since that is pioneering study, GCMs have been widely used to project future changes in global TC activities under global warming conditions (e.g., Bengtsson et al. 1996; Sugi et al. 2002; Oouchi et al. 2006; Zhao et al. 2009; Murakami et al. 2012). Summarizing these previous studies, Knutson et al. (2010) reported a reduction in the frequency of global TCs but an increase in ratio of intense TCs to total TCs.

The reduction in TC formation is thought to be linked to a reduction in upward mass flux associated with the weakening of tropical circulation (Sugi et al. 2002; Sugi and Yoshimura 2012; Walsh et al. 2014) or an increase in the saturation deficit of the

middle troposphere (Emanuel et al. 2008). These theories explain the reduction in the TC formation, but cannot account for the increase in the proportion of intense TCs.

As the world warms, sea surface temperature (SST) will rise, resulting in increased TC intensity. On the basis of the assumptions of hydrostatic and gradient balance and slantwise neutrality, Emanuel (1986) derived the minimum attainable central surface pressure (p_{cs}) for a TC under ideal conditions (i.e., not including the effects of vertical wind shear, troughs, and other environmental factors). Emanuel defined p_{cs} as

$$\ln p_{cs} = \ln p_{as} - \frac{C_p}{R} \frac{\left(\frac{T_b - \overline{T}_{out}}{T_b}\right) \frac{Lq_a^*}{C_p T_s} \left(RH_c - RH_a\right)_s - \frac{1}{4} \frac{f^2 r_0^2}{C_p T_b}}{1 - \left(\frac{T_b - \overline{T}_{out}}{T_b}\right)\left(1 + \frac{Lq_a^* RH_{cs}}{C_p T_s}\right)}, \qquad (1.1)$$

where C_p is the specific heat of dry air at constant pressure, R is the gas constant for dry air, f is the Coriolis parameter, L is the latent heat of condensation, p is pressure, T is temperature, q^* is saturation specific humidity, RH is relative humidity, and r is distance from the center of the TC. The surface pressure gradient vanishes at $r = r_0$. Subscripts a and c denote the ambient and the center of the TC, respectively. The subscripts s and b denote the surface and top of the boundary layer, respectively. $\overline{T}_{out}$ indicates the average outflow temperature.

Figure 1.1 shows plots of p_{cs} as a function of T_s. Following Emanuel (1986), we assumed that $T_B = T_S - 5\,^{\circ}\mathrm{C}$; p_{cs} = 1015 hPa; RH_{cs} = 100%; and RH_{as} = 80%. p_{cs} deepens as T_s increases; its change rate is sensitive to $\overline{T}_{out}$ (Fig. 1.1). Assuming an increase in T_S to be due to global warming, TC is intensified under warmer climates.

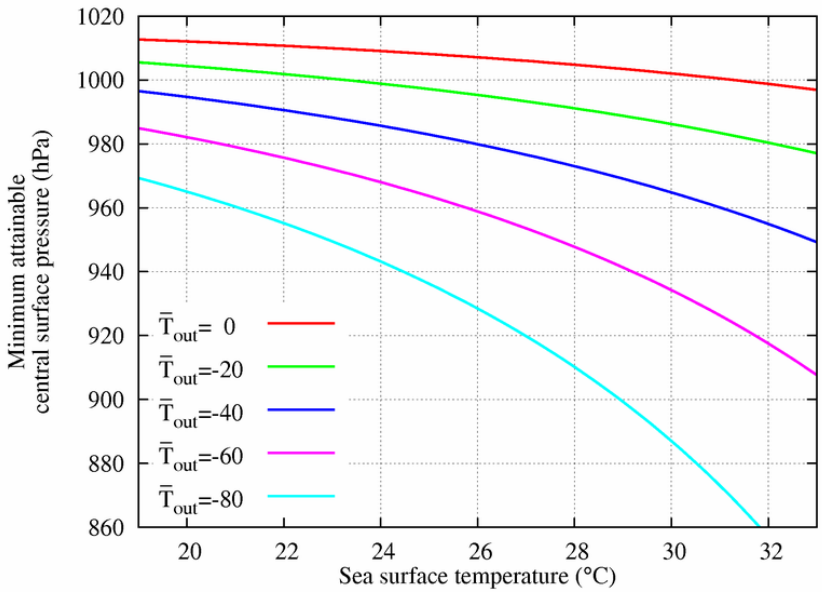

Fig. 1.1 Minimum attainable central surface pressure (hPa) computed from Eq. 1.1 [Eq. 26 of Emanuel (1986)] as a function of sea surface temperature assuming an ambient surface pressure of 1015 hPa, ambient surface relative humidity of 80%, the Coriolis evaluated at 20 degrees latitude, and r_0 = 500 km.

Using the outputs (Kodama et al. 2015) of the Nonhydrostatic ICosahedral Atmospheric Model (NICAM; Tomita and Satoh 2004; Satoh et al. 2008; 2014), Satoh et al. (2015) found that the ratio (R_{mf}) of convective mass flux associated with TC (M_{tc}) to total convective mass flux in the tropics (M_T) is proportional to the intensity of the *TC*; R_{mf} remains almost unchanged between the present-day and future climates in the simulation. They proposed a constraint on the genesis of TCs through a diagnostic relationship on the basis of the convective mass flux (i.e., intense TCs increase due to global warming, consuming $R_{mf} \times M_T$, and the number of TCs consequently decrease).

Regarding the genesis of regional TCs, various studies have predicted different effects of global warming on TC formation rate (Knutson et al. 2010). This discrepancy appears to arise from responses of relative SST change distribution (Sugi et al. 2009).

The difficulty in reproducing the observed TCs also contributes to the discrepancy (Murakami et al. 2014). TC formation is sensitive to the choice of convective parameterization and to dynamical cores in the model (Walsh et al. 2013). To more reliably predict future TC activity, Murakami et al. (2012) proposed the use of multiple models, emission scenarios, and SST changes. In past studies, projections of future TC activity have been reported on the basis of primitive equation models. This study projects future TC activity using a nonhydrostatic GCM, NICAM.

1.2 Structure of tropical cyclone

Although horizontal sizes of TCs along with their number and intensities modulate the magnitudes of the resulting natural disasters (Kimball and Mulekar 2004), future changes in the horizontal sizes of TCs have not yet been fully investigated (Knutson et al. 2010; IPCC 2013; Walsh et al. 2014) using GCMs or Atmospheric GCMs (AGCMs). TCs simulated by low-resolution AGCMs are much weaker and larger than observed TCs (McDonald et al. 2005; Camargo 2013), indicating that the previous AGCM studies are insufficient to predict future changes in TC structure.

What kinds of structural models should be used to study future changes in TC? Figure 1.2 shows a schematic of TC structure based on Jorgensen (1984b). TCs are rapidly rotating storm systems characterized by primary and secondary circulation. The primary circulation (blue vector in Fig. 1.2) is influenced by the surface friction within the boundary layer, inducing inflow (yellow vector in Fig. 1.2). The inflow transports water vapor and angular momentum to the center of the TC. The concentrated inflow forms updrafts and the eyewall. Air parcels lifted by the updrafts then gain latent heat through the condensation of water vapor. The effect of surface friction weakens with

increasing altitude, and updrafts have outward slope. Since the radius is widened with conserving angular momentum, tangential wind weakens at higher altitude. As this vertical gradient of tangential wind must satisfy the thermal wind balance, the horizontal gradient of temperature (i.e., the warm core) must form in the center of the TC.

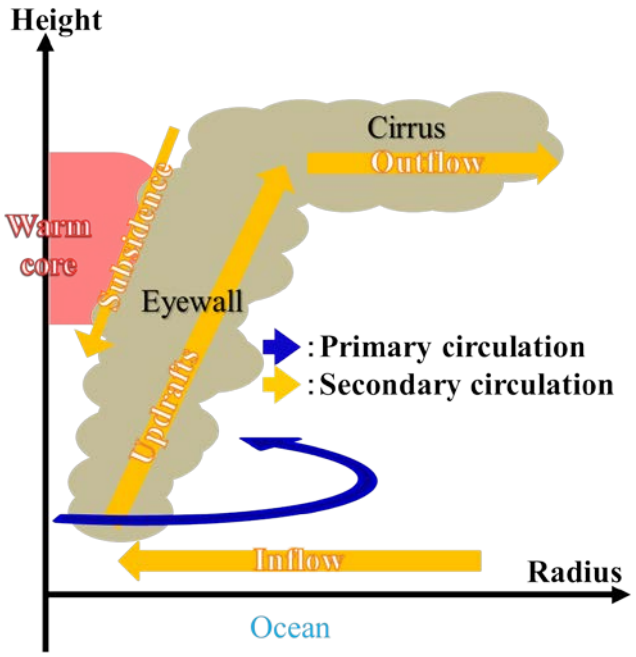

Fig. 1.2. Schematic of TC structure based on Jorgensen (1984b). CTC and RMW are the center of the TC and the radius of maximum wind, respectively.

The updrafts diverge at the upper troposphere or lower stratosphere, shaping the outflow outside the eyewall and the downward flow within the eyewall. The downward flow is dry and warm due to adiabatic expansion, resulting in the forming of a warm core in the upper troposphere and a clear eye. The warm core induces a thermal gradient in the radial direction, and the downward flow transports weak momentum from the upper atmosphere to the lower atmosphere within the eyewall (Malkus 1958).

Secondary circulation was theoretically modeled by Eliassen (1951),

Willoughby (1979), Shapiro and Willoughby (1982), and Pendergrass and Willoughby (2009) using the Sawyer–Eliassen model. The results indicated that secondary circulation is induced by latent heating and surface momentum in TCs. Therefore, to study future changes in TC structure, AGCM should reproduce the secondary circulation along with the eyewall, which is the source of latent heating.

The outward slope of the eyewall (Fig. 1.2) is a characteristic feature of TCs and influences the locus of latent heating. According to observational studies, the radius of maximum wind (RMW) locates relative to maxima of vertical updraft and radar reflectivity (Jorgensen 1984a; 1984b); particularly, it locates outward of the updrafts from the cyclone center (Jorgensen 1984b; see Fig. 1.2). Within the eyewall, the secondary circulation merges larger angular momentum transported from outer radii of the eyewall and weaker momentum transported from upper atmosphere (Malkus 1958). Therefore, it appears that the maxima of updrafts and radar reflectivity locate inside of the RMW.

Although slope of eyewall could not be explained, thermal wind balance and conservation of angular momentum explain the outward slope of the isoline that connects the RMWs at each altitude, and its slope is in the range of

$$0 < \frac{\Delta z}{\Delta r} < -\left(\frac{v}{r} + f\right)\left(\frac{\partial v}{\partial z}\right)^{-1} \quad , \tag{1.2}$$

where z is altitude, r is RMW, v is the maximum wind speed, and f is the Coriolis parameter. The derivation of Eq. 1.2 is described in the Appendix. Since the vertical gradient of v is negative due to the limitation of thermal wind balance, the isoline of RMW has an outward slope.

Observational studies demonstrated that the outward slope of eyewall depends

on the RMW at a low altitude of 2 km (Stern and Nolan 2009; Stern et al. 2014) or on the intensity of the TC (Hazelton and Hart 2013). They estimated the eyewall slope from the RMW, updrafts, absolute angular momentum, and 20-dBZ reflectivity isosurface. Stern and Nolan (2009) argued that the eyewall becomes more upright as RMW decreases, while the slope of eyewall is independent of TC intensity. However, Hazelton and Hart (2013) reported that the slope becomes more upright as the TC becomes more intense. The findings of these two studies are conflicting even though they were derived from similar datasets.

Stern et al. (2014) discussed why the findings of Stern and Nolan (2009) conflicted with those of Hazelton and Hart (2013). Both studies employed different definitions of slope. Stern and Nolan (2009) defined the slope by the best-fit line used to connect each RMW between 2 and 8 km. Hazelton and Hart (2013) estimated the slope between heights of 2 and 11 km. Thus, the methods used to study the outward slope of the eyewall remain controversial.

The convergence of simulated TC structure and intensity was investigated with a regional circulation model (RCM) with a super-high resolution of less than 10 km (Fierro et al. 2009; Gentry and Lackmann 2010). Both studies used the same RCM, Weather Research and Forecasting model (Skamarock et al. 2005). Fierro et al. (2009) examined the impact of horizontal grid spacing on TC structure and intensity by simulating Hurricane Rita (2005). In their model, TC intensity converged in horizontal grid intervals between 1 and 5 km, whereas TC structure did not. Similarly, Gentry and Lackmann (2010) tested the relationship between horizontal grid spacing and TC structure and intensity by simulating Hurricane Ivan (2004). They found that both TC structure and intensity did not converge in grid intervals between 1 and 8 km. Gentry

and Lackmann (2010) speculated that the difference between the results of these studies is attributable to the size of the computational domain, the nesting method (one- or two-way), and/or case-dependent factors.

Both of the abovementioned studies simulated the eyewall sloping outward. The slopes of the eyewalls depended on horizontal resolution, which is consistent with the findings of Stern and Nolan (2009). As finer-resolution models simulate smaller RMWs than coarser ones, the eyewall slope becomes more upright as the horizontal grid spacing becomes smaller. Thus, the effect of horizontal resolution on the eyewall slope should be considered.

Sun et al. (2013) investigated the convergence of TC intensity and structure by simulating Typhoon Shanshan (2006) under different horizontal grid intervals and different convective parameterization schemes. They reported that the choice of convective parameterization scheme affected the convergence of TC intensity. The findings also indicated that the eyewall slope depended on TC intensity and RMW size, which is in agreement with the findings of Hazelton and Hart (2013). Herein, we do not examine the effect of the convective parameterization scheme. However, note that TC structure and intensity are sensitive to the convective parameterizations as well as the horizontal grid spacing.

1.3 Recent studies on the effects of global warming on tropical cyclone structure

Recently, improvements in available resources have allowed many studies to use higher-resolution AGCMs to study the global climatology of TCs (Oouchi et al. 2006; Sugi et al. 2009; Murakami et al. 2012; Satoh et al. 2012, 2015; Roberts et al. 2015; Wehner et al. 2015; Kodama et al. 2015; Satoh et al. 2015). By reducing the grid interval, AGCMs are able to simulate more realistic TC structures including the RMW and the warm core (Manganello et al. 2012; Roberts et al. 2015).

Manganello et al. (2014) showed that the RMW is slightly diminished in warmer climates using the European Centre for Medium-Range Weather Forecasts (ECMWF) Integrated Forecast System (Jung et al. 2012) with a horizontal resolution of 16 km. However, despite realistically simulating the RMW and warm core, their results indicated that the composite structure for upward velocity of the simulated TCs was located at the center of the TC, while the downward velocity within the eye was unclear. To explain these deficiencies, Manganello et al. (2014) speculated that the resolution was still extremely coarse to completely resolve the inner-core processes, and convection scheme produced inaccurate horizontal diffusion.

Murakami et al. (2012) depicted composite horizontal distributions of precipitation around TCs using high-resolution Meteorological Research Institute (MRI) atmospheric circulation models (see Fig. 6 of Murakami et al. 2012). These models simulated weaker precipitation in the center of the TC compared to areas outside the center. This suggests that the eye of a TC could be simulated even though the models used convective parameterization. As discussed in Sun et al. (2013), the treatment of

convective parameterization is more important for simulating TC structure rather than whether or not it is employed.

Previous studies using RCM (Fierro et al. 2009; Gentry and Lackmann 2010; Sun et al. 2013) suggested that a horizontal grid spacing of more than 2 km is extremely coarse to resolve TC structure. In general, RCMs adopt a finer horizontal mesh than AGCMs. Using a 2-km horizontal mesh nonhydrostatic RCM without a cumulus convection scheme, Kanada et al. (2013) conducted downscaling simulations of extremely intense TCs simulated in AGCM (Murakami et al. 2012). In their study, extremely intense TCs were defined as those with a minimum central pressure reaching below 900 hPa. They chose six examples of extremely intense TCs for present-day and global warming simulations. These simulations reproduced the realistic updraft structures of TCs. A comparison of the composite structures of six TCs in each simulation under warmer climate conditions indicated that the RMW decreases in this model. The central pressures of the TCs decreases by more than 20 hPa compared to those under present-day climates. Intense TCs have strong primary circulation, inducing intense surface inflow. The intense inflow irrupts inward towards the eye. Thus, the RMW decreases in warmer climates (Kanada et al. 2013).

When we examine the differences in the structures of TCs with the same intensities under present-day and future climate conditions, does it indicate the response of TCs to global warming? Structural aspects of TCs, such as the size of the RMW, vary from TC to TC (Weatherford and Gray 1988; Kimball and Mulekar 2004). To elucidate future changes in TC structure, we need to statistically compare TC structures between each climate condition with the number of sufficient TCs.

1.4 Purpose of this study

The previous studies using AGCMs summarized in Knutson et al. (2010) and IPCC (2013) discussed statistics-based future changes in TC frequency and intensity. These studies predicted reductions in global TC frequency and increases in the proportion of intense TCs relative to total TCs. However, a few studies focused on future changes in components of TC structure, such as RMW (Manganello et al. 2014). Kanada et al. (2013) investigated the response of TC structure to global warming and demonstrated that RMW is decreased by warming climate. However, the number of samples used in that study was small, and the difference between the mean TC intensities for the present-day and future simulations was large. RMW depends on TC intensity with large variation (Weatherford and Gray 1988; Kimball and Mulekar 2004).

The present study statistically investigates the response of TC structure to global warming for TCs with the same intensity in both present-day and global warming climate conditions. To achieve this, we need to simulate a large number of TCs for each climate condition. The development of supercomputers in recent years allows us to conduct long-term simulations with finer horizontal resolution. Kodama et al. (2015) ran an AMIP-type simulation for more than 30 years using 14-km mesh NICAM without a cumulus parameterization. This simulation indicated that the global frequency of TCs in NICAM is consistent with the observed global frequency.

The secondary circulation of TCs is affected by the heating source within the eyewall. To discuss future change in TC structure, the model should be able to simulate the outward slope of the eyewall (i.e., updrafts). Using the outputs of Kodama et al. (2015), Satoh et al. (2015) revealed that NICAM simulates the outward-sloping eyewall (see Fig. 4 in Satoh et al. 2015). Therefore, the output of the 14-km NICAM simulation

is expected to be useful to discuss future change in TC structure.

The remainder of the thesis is structured as follows: Chapter 2 describes the model settings, experimental design, method for detecting TCs in the model output, and the observations used in model validation. Chapter 3 overviews the reproducibility of the TC activity simulated by NICAM. The responses of TC activity to global warming are summarized in Chapter 4. Chapter 5 documents the predicted future changes in TC structure and proposes an underlying mechanism. In Chapter 6, we discuss on the effect of grid spacing on the results described in Chapter 5. In Chapter 7, using the Sawyer–Eliassen model, we estimate the effect of the degree of the eyewall slope on the results. Finally, general conclusions are presented in Chapter 8.

Chapter 2 Methodology and Data

2.1 Model settings and experimental design

This thesis is based on two numerical simulations conducted using NICAM, which is an AGCM (Tomita and Satoh 2004; Satoh et al. 2008, 2014). Both simulations were performed over a period of more than 30 years on the K computer (Yokokawa et al. 2011) at the RIKEN Advanced Institute for Computational Science. One of the simulations began on June 1, 1978, and the other began on June 1, 2074. Hereafter, the former is called the present-day simulation (PD), and the latter is called the global warming simulation (GW). The results of PD are documented in Kodama et al. (2015).

Table 2.1. Physical processes in both simulations.

Cloud microphysics	NICAM Single-moment Water 6 (Tomita 2008)
Cumulus convection	Not used
Radiation	mstrnX (Sekiguchi and Nkajima 2008)
Turbulence	Mellor-Yamada Nakanishi-Niino (Nakanishi and Niino 2006; Noda et al. 2010)
Gravity waves	Not used
Land surface	Minimal Advanced Treatments of Surface Interaction and RunOff (Takata et al. 2003)
Ocean model	Single layer slab-ocean

The model settings of both simulations were the same and are listed in Table

2.1. The horizontal grid spacing was approximately 14 km, and the cloud systems were explicitly calculated without a cumulus convective scheme. The water substances were classified into six categories (water vapor, liquid cloud, ice cloud, rain, snow, and graupel) and were calculated using a single-moment bulk cloud microphysics scheme (Tomita 2008). A broadband radiative transfer cord called MSTRNX (Sekiguchi and Nakajima 2008) was utilized for calculating atmospheric radiation processes. The simulations employed a second-order turbulence closure scheme based on Nakanishi and Niino (2006) and modified by Noda et al. (2010) for cloudy skies. The energy and water exchanges between atmosphere and land were solved using a land surface model called Minimal Advanced Treatments of Surface Interaction and RunOff (MATSIRO; Takata et al. 2003).

Table 2.2 shows the experimental designs. The performance of PD is reported in Kodama et al. (2015). Apart from adopting a single-layer slab-ocean model, this simulation followed the Atmospheric Model Intercomparison Project (AMIP; Gates 1992). The SST and sea ice (SIC) in the present-day experiment were nudged toward the Hadley Centre SIC and SST dataset (Rayner et al. 2003).

Future changes in SST and SIC were determined by the method of Mizuta et al. (2008) using the 18-model ensemble mean of the World Climate Research Program (WCRP) Coupled Model Intercomparison Project Phase 3 (CMIP3; Meehl et al. 2007). The climate forcing in GW was created by computing the differences between the average SSTs and SICs from 1979–2003 and 2075–2099 (recorded in the CMIP3 A1B scenario data) and adding these differences to each observed dataset. The SST difference revealed an El Niño-like SST pattern (Mizuta et al. 2008), and the emission scenario of CO_2 concentration followed the SRES A1B scenario.

Table 2.2. Experimental designs of the PD and GW.

	PD	GW
Periods	June 1, 1978 to December 31, 2008	June 1, 2074 to December 31, 2104
Initial condition	European Centre for Medium-Range Weather Forecasts Reanalysis-40 (Dee et al. 2011)	
Boundary condition	Hadley Centre Sea Ice and Sea Surface Temperature (HadISST; Rayner et al. 2003)	HadISST + ΔSST (Mizuta et al. 2008)

The initial atmospheric conditions in both simulations were taken from the European Centre for Medium-Range Weather Forecasts Reanalysis-40 (ERA-40; Dee et al. 2011). As described in the beginning of this subchapter, PD began on June 1, 1978, and GW began on June 1, 2074. Both simulations were run for 30 years and seven months. The first seven months in each simulation were regarded as the spin-up period, and the final 30 years were analyzed.

2.2 Tracking methods

When TCs are discussed using a GCM, TCs in the GCM must first be detected with a tracking method. A tracking method includes thresholds for classifying disturbances as TCs or tropical depressions according to their strengths and structures. Wind speed and/or vorticity are employed as the strength thresholds. The structural requirements of a TC are a warm core and a low-level wind speed that is greater than the upper-level wind speed. The maximum wind speed of a TC is quite sensitive to the

horizontal grid spacing of the GCM (Murakami et al. 2012; Manganello et al. 2012; Roberts et al. 2015). Various thresholds for the wind speed have been used in previous studies (Walsh et al. 2007), complicating the comparison among the results of previous studies. Walsh et al. (2007) developed an objectively determined resolution-dependent threshold for wind speed. They constructed a typical radial wind profile using observational data (Kimball and Mulekar 2004) and an analytic method (Holland 1980). The constructed wind profile was subsampled at a horizontal grid interval. The large grid interval underestimated the maximum wind speed relative to observed wind profiles. In their study, the maximum wind speed for the 14-km mesh was approximately 17.5 m s^{-1}, which is equal to the observed value.

Herein, the method used to detect TCs in each simulation followed Sugi et al. (2002) and Oouchi et al. (2006). The employed method uses the wind speed threshold, which is objectively determined from the horizontal grid spacing (Walsh et al. 2007), and consists of the following two steps. First, at six-hourly intervals, grid points on which the surface pressure and its mean (computed over the 7° × 7° grid box surrounding each point) differs more than 0.5 hPa less at each time step are gathered. These grid points are candidates for the center of the TC.

The next step combines these grid points into a TC track, which must satisfy the following criteria.

1) The maximum wind speed at a height of 10 m exceeds 17.5 m s^{-1}, which is searched over the 3° × 3° grid box surrounding the candidate grid for TC center.
2) The maximum relative vorticity at 850 hPa exceeds 1.0×10^{-3} s^{-1}.

3) The temperature structure aloft has a marked warm core; that is, the temperature deviations at 300, 500, and 700 hPa sum to more than 2 K. The temperature deviation is defined as the difference between the temperature at the candidate grid and the mean temperature over the 7° × 7° grid box surrounding the candidate grid.
4) At each grid point, the regional mean difference between the wind velocity components at 850 and 300 hPa exceeds 0 m s^{-1}.
5) The duration of each detected storm exceeds 36 h.

These thresholds are independent of the ocean basin. TCs can form within a limited range of latitudes (30° S–30° N).

The relative vorticity in Criterion (2) is larger than in previous studies. This value was optimized to match the number of annual global mean TCs in the present-day simulation with the observed number. The formation position of a TC is defined as the grid point at which the abovementioned thresholds are first satisfied.

2.3 Best-track data

To evaluate whether NICAM can simulate TC formation under present-day climate, the simulated TCs were compared with the best-track datasets compiled by the International Best Track Archive for Climate Stewardship (IBTrACS; Knapp et al. 2010), which comprise data from the World Meteorological Organization Regional Specialized Meteorological Centers, Tropical Cyclone Warning Centers, and other national agencies. IBTrACS contains the position and maximum wind speed of cyclones

over all ocean basins in addition to central sea-level pressure (SLP) over some ocean basins. The duplicate records of various agencies were consolidated into one record. Thus, these data are available to evaluate the ability of a GCM to simulate global TC activity, although a definition of the maximum wind speed are non-homogeneous (Knapp et al. 2010).

The maximum wind speeds in IBTrACS are time-averaged values, and the averaging periods are dependent on the agencies that furnished their best-track datasets (Knapp and Kruk 2010). We selected the National Hurricane Center (the North Atlantic and eastern North Pacific; Jarvinen et al. 1984) and the Joint Typhoon Warning Center (the western North Pacific, north Indian Ocean, and Southern Hemisphere; Chu et al. 2002) from the data archived in IBTrACS because these datasets both use 1-min average wind speeds.

This best-track datasets include a parameter which characterize TC natures in its lifecycle: tropical depression, tropical cyclone, extratropical cyclone. Since we are interested in TCs, we excluded the tropical depressions and the extratropical cyclones. However, this parameter was not complete in all of the historical records. We defined a tropical depression as a system in which the maximum intensity did not exceed 17.5 m s^{-1} and excluded them from the present study. Therefore, we decided that any grid point at which the maximum wind speed first equals or exceeds 17.5 m s^{-1} was the formation site of a TC.

Chapter 3 Reproducibility of Tropical Cyclone Activities

In this chapter, we review the performance of NICAM in simulating the activities of TCs, including their geographical distribution, seasonal cycles, interannual variations, and intensities. The PD simulation has been documented by Kodama et al. (2015). Based on the present-day climatological TC activity simulated between 1979 and 2003, they derived the geographical distribution and seasonal cycle of TC formation for each ocean basin listed below. Herein, we consider the entire globe, including the northern and southern hemispheres and six ocean basins: the North Indian Ocean, the western North Pacific, the eastern North Pacific, the North Atlantic, the South Indian Ocean, and the South Pacific. These ocean basins are separated by dotted lines in Fig. 3.1.

3.1 Genesis and seasonal cycle

Figure 3.1 shows the observed and simulated geographical distributions of the density of generated TCs. Here, density of generated TCs is defined as the number of TCs formed per year in each 5° × 5° grid box. In general, the simulated geographical distribution (Fig. 3.1b) resembles the observed distribution (Figs. 3.1a). Table 3.1 lists the number of generated TCs in the six ocean basins, the northern and southern hemispheres, and around the globe. Although the model predicts a smaller number of TCs than observed over the North Atlantic, the annual number of TCs simulated over the western North Pacific (25.1) agrees with the observed value (25.4).

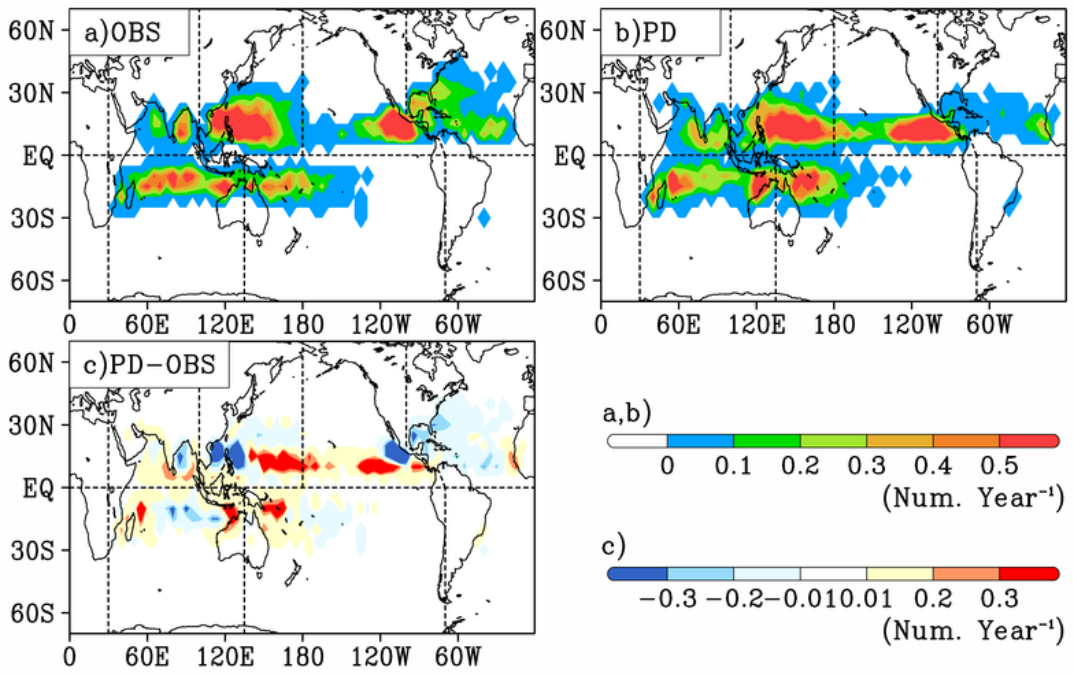

Fig. 3.1. Geographical distribution of the density of generated TCs between 1979 and 2008. Density is defined as the number of cyclones per year formed in a 5° × 5° grid box. Panels (a) and (b) show the observed (OBS; IBTrACS) and the PD simulation densities, respectively. OBS data were calculated from the IBTrACS dataset. Panel (c) plots the difference between the PD and OBS results. The dotted lines separate the six ocean basins. The boundary between the eastern North Pacific and North Atlantic lies along Central America.

The plot showing the difference in the observed and simulated densities of generated TCs (Fig. 3.1c) indicates that the model underestimates the number of TCs over the Bay of Bengal, the South China Sea, the western coast of Mexico, the Gulf of Mexico, the North Atlantic, and the central South Indian Ocean. In contrast, the model overestimates the number of TCs over the Arabian sea, the Central and Eastern North Pacific (longitude 140° E–80° W; latitude 5° N–15° N), near the Island of Madagascar, and north of Australia. These differences mirror the results of Kodama et al. (2015), who plotted the geographical distributions of the simulated and observed seasonal mean climatological precipitation rate (see Fig. 1 of their paper). As demonstrated by

McDonald et al. (2005), the geographical distributions of the simulated and observed precipitation rates differ similarly to those of TC formation.

Table 3.1. Numbers of TCs generated per year above various ocean regions obtained from the IBTrACS dataset (OBS) and from the PD simulation. Standard deviations are shown in parentheses. The regions are six ocean basins: the North Indian Ocean (NIO), the western North Pacific (WNP), the eastern North Pacific (ENP), the North Atlantic (NA), the South Indian Ocean (SIO), and the South Pacific (SP), the Northern and Southern Hemispheres (NH and SH, respectively), and the entire globe (GL). The six ocean basins are delineated in Fig. 3.1.

	NI	WNP	ENP	NA	SI	SP	NH	SH	GL
OBS	4.4	25.4	16.0	11.5	15.5	9.3	57.3	24.8	82.1
(Num.)	(0.34)	(0.78)	(0.82)	(0.81)	(0.55)	(0.64)	(1.20)	(0.83)	(1.55)
PD	5.6	25.1	19.5	4.5	17.4	12.2	54.7	29.7	84.4
(Num.)	(0.42)	(1.05)	(0.88)	(0.44)	(0.86)	(0.85)	(1.38)	(0.91)	(1.47)

As shown in Fig. 3.2, the PD successfully captures the climatological number of TCs generated per month in most ocean basins (the exception is the North Atlantic). This finding is consistent with Kodama et al. (2015). To evaluate the relationship between TC formation and convection, we defined the active seasons of TC genesis as the months in which the genesis ratio of monthly TCs to annual cyclones exceeds 5% in IBTrACS. The active months are superimposed as triangles on Fig. 3.2.

Figure 3.3 depicts the seasonal mean precipitation rates in the active season. These data are based on Fig. 3.2 in the present-day experiment and the Global Precipitation Climatology Project version 2.2 (GPCP; Adler et al. 2003). We found a close correspondence between the geographical distributions of the differences in precipitation rates and those in TC genesis, except in the vicinity of the equator. TCs seldom or never form near the equator due to the absence of the Coriolis force.

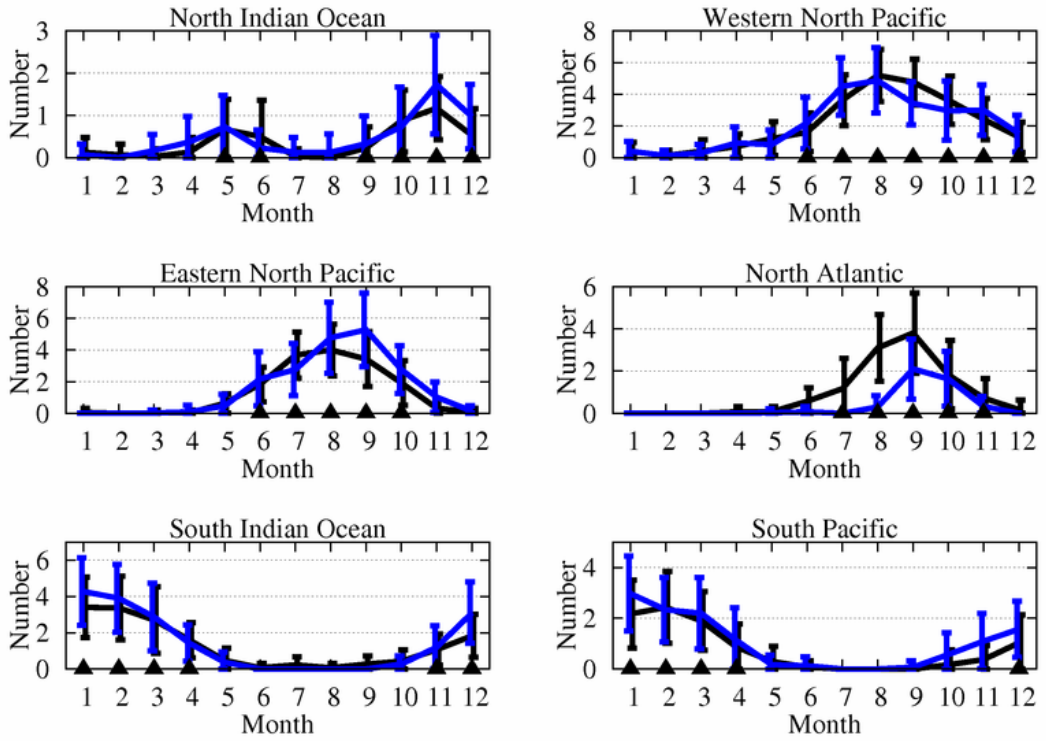

Fig. 3.2. Monthly mean climatological numbers of TCs generated in each ocean basin defined in Fig. 3.1. Bars represent the standard deviations. The IBTrACS and PD results are indicated in black and blue, respectively. Triangles indicate months of active TC genesis. The active season is defined as the months in which the genesis ratio of monthly to annual TCs exceeds 5% in the ocean basin (based on IBTrACS).

For instance, cyclone genesis is reduced in areas of dry bias, such as the North Atlantic (Figs. 3.1c and 3.3c). Although TC formation was significantly reduced in the PD simulation from June to September (Fig. 3.2), this disagreement diminished in October and November. The dry biases were more conspicuous between June and August than between September and November [see Fig. 1 in Kodama et al. (2015)]. Therefore, the discrepancy in TC genesis appears to be strongly related to biases in total precipitation.

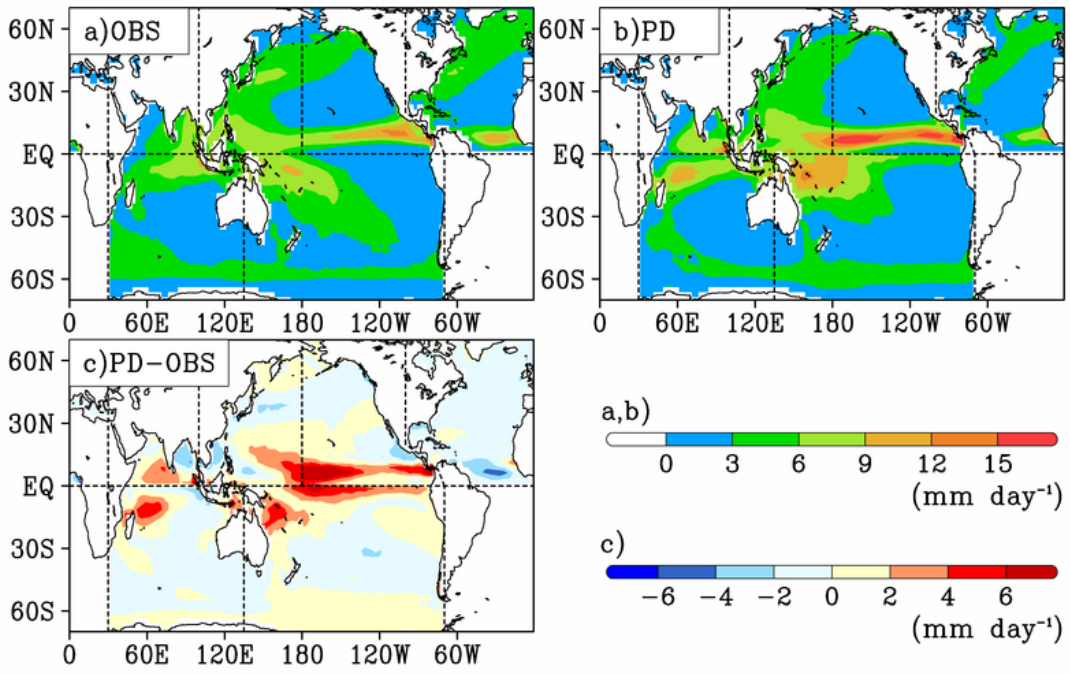

Fig. 3.3. Seasonal mean precipitation rates (mm day^{-1}) during an active season of TC genesis in the six ocean basins analyzed from January 1979 to December 2008. Panels (a) and (b) plot the results of GPCP Ver. 2.2 and the PD, respectively, and the differences between the two methods are plotted in panel (c). The dotted lines are explained in Fig. 3.1. Each ocean basin exhibits its precipitation seasonal mean in the seasons of active TC formation. The active seasons are defined as the months in which the ratio of monthly to annual formation of TCs exceeds 5% in the ocean basin (see Fig. 3.2).

3.2 Large-scale environmental conditions

In the previous subchapter, we demonstrated that underestimations and overestimations in TC genesis are coincident with those of precipitation. TC genesis and precipitation are both controlled by large-scale environmental conditions. Gray (1968) documented relationships between TC development in each ocean basin and large-scale environmental conditions such as troughs and vertical wind shear. In this subchapter, we discuss TC formation and large-scale environmental conditions.

Gray (1998) reported that seasonal TC formation is closely related to the climatological environmental conditions, including (1) the Coriolis parameter, (2) low-level relative vorticity, (3) relative humidity in the mid-troposphere, (4) ocean thermal energy, (5) equivalent potential temperature, and (6) the tropospheric vertical wind shear, and developed a Genesis Potential Index (GPI) based on the above six parameters. Tropospheric vertical wind shear (6) inhibits the development of convection, producing a less-favorable environment, while the other conditions are favorable for TC formation. Emanuel and Nolan (2004) also developed a GPI. GPIs provide good estimates of seasonal TC formation (Gray 1998; Emanuel and Nolan 2004).

GPIs have been employed to examine the ability of GCM to reproduce TC formation (McDonalds et al. 2005; Camargo et al. 2007; Yokoi et al. 2009; Walsh et al. 2013). Although Gray's GPI uses a specific threshold of 26°C based on observation, Emanuel and Nolan's GPI (*EGPI*) does not have a specific threshold value (Yokoi et al. 2009). Because we will apply *EGPI* to the GW simulation in the next chapter, we use *EGPI* to examine the relationships between TC formation and large-scale environmental conditions. *EGPI* was defined as

$$EGPI \equiv \left|10^5 \eta\right|^{\frac{3}{2}} \left(\frac{RH}{50}\right)^3 \left(\frac{PI}{70}\right)^3 \left(1+\frac{V_{sh}}{10}\right)^{-2}, \tag{3.1}$$

where η (s^{-1}) is the absolute vorticity at 850 hPa, *RH* (%) is the relative humidity at 700 hPa, *PI* (m s^{-1}) is the potential intensity (Emanuel 1986, 1995; Bister and Emanuel 1998), and V_{sh} (m s^{-1}) is the magnitude of the shear vector from 850 to 200 hPa. *PI* indicates an intensity which a TC achieves for a given environmental conditions, being defined as Eq. 3 of Bister and Emanuel (2002):

$$PI^2 = \frac{T_s}{T_{out}} \frac{C_k}{C_D} \left(CAPE^* - CAPEb \right), \tag{3.2}$$

where T_s and T_{out} are the temperatures at the sea surface and outflow regions in the upper troposphere, respectively, C_k is the exchange coefficient for enthalpy, C_D is the drag coefficient, and *CAPE* is the convective available potential energy. *CAPE** is the *CAPE* of air lifted from saturation at sea level in reference to the environmental soundings, and *CAPEb* is that of air in the boundary layer. A FORTRAN subroutine to calculate the *PI* is available at http://eaps4.mit.edu/faculty/Emanuel/products.

We calculated the *EGPI* from the Japanese 55-year reanalysis (JRA-55; Ebita et al. 2011) and PD simulation. This analysis was limited to the active seasons of the various ocean basins, as indicated in Figs. 3.2 and 3.3. Figure 3.4 depicts the geographical distributions of the seasonal mean *EGPI* (Fig. 3.4a) and its components (Figs. 3.4b-e). The numbers 1, 2, and 3 appended to the alphabetical symbols refer to JRA-55, PD simulation, and the difference between JRA-55 and PD simulation, respectively. The *EGPI*s in JRA-55 and PD (Fig. 3.3a1 and a2) are consistent with the observed and simulated TC genesis (Fig. 3.1a and b), respectively. PD reproduces underestimations in TC geneses and *EGPI* over the North Atlantic (Figs. 3.1c and 3.3a3), although the *EGPI* in PD is greater than that in JRA-55 over all the ocean basins except the North Atlantic (Fig. 3.4a3). This overestimation of *EGPI* appears to originate from biases in the magnitude of *PI*. These biases are attributable to temperature profiles in convective regions. The temperature profiles are sensitive to models with thermodynamic constants and assumptions (Emanuel et al. 2008; Yokoi et al. 2009). It is difficult to compare the amplitudes of *EGPI* and *PI* between JRA-55 and PD. Therefore, we compare the overestimations and underestimations in formed TCs, as described in

Chapter 3.1, with those of the other components of *EGPI* (i.e., the relative humidity, absolute vorticity, and vertical wind shear).

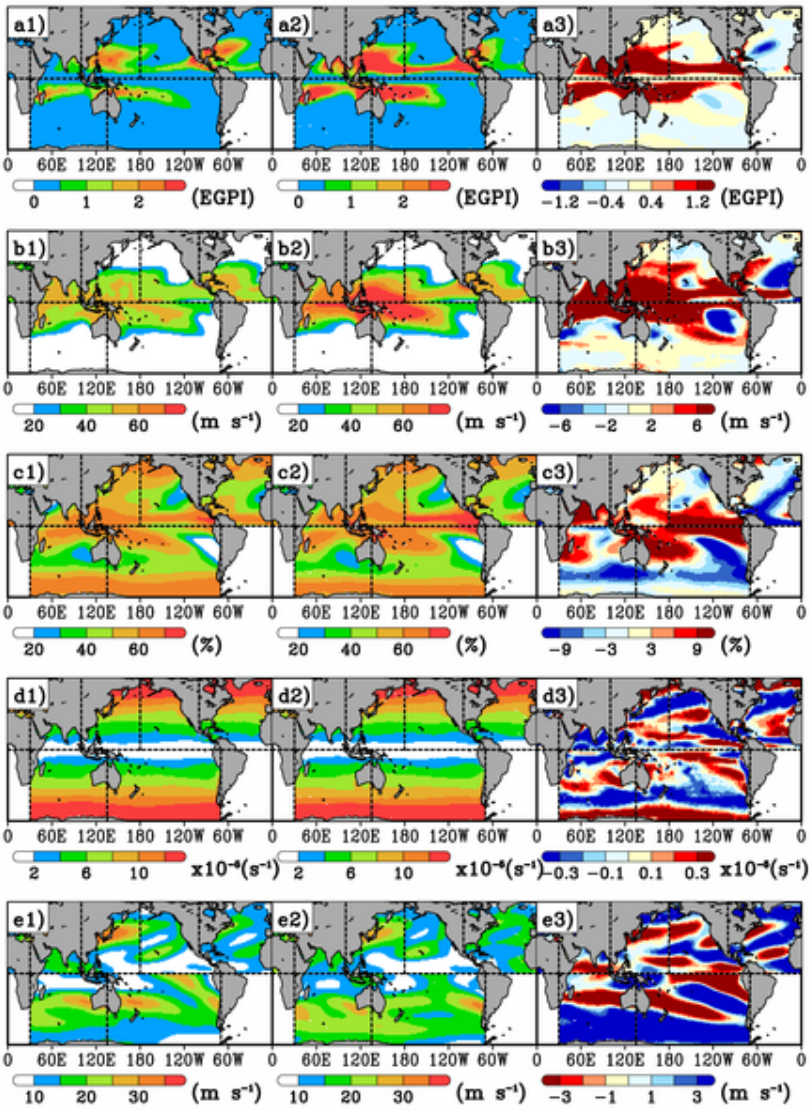

Fig. 3.4. Seasonal mean genesis potential index (*EGPI*) and its components in six ocean basins during their active seasons of TC formation computed from a reanalysis (JRA-55) and the PD simulation. The active seasons are the same as those in Fig. 3.3 for the respective ocean basins. Panel (a) plots *EGPI*, panels (b), (c), (d), and (e) plot the potential intensities (m s^{-1}), relative humidity at 700 hPa (%), absolute vorticities (s^{-1}), and magnitudes of vertical wind shear (m s^{-1}), respectively. The numbers 1, 2, and 3 appended to each alphabetical symbol refer to JRA-55, PD, and their difference, respectively. The dotted lines are those of Fig. 3.1.

As described in Chapter 3.1, TC geneses are underestimated over the Bay of

Bengal, the South China Sea, the western coast of Mexico, the Gulf of Mexico, the North Atlantic, and the central South Indian Ocean (Fig. 3.1c). *EGPI* reproduces the underestimation of TC geneses over the Gulf of Mexico and the North Atlantic. Other ocean sub-basins show that the relative humidity in the PD is less favorable than that of JRA-55, with the exceptions of the Bay of Bengal and South China Sea (Fig. 3.3c3). Over both ocean sub-basins in PD, the relative humidity is more favorable than in JRA-55, whereas the absolute vorticity and vertical wind shear are less favorable (Figs. 3.3d3 and e3). This indicates that the intense vertical wind shear inhibits convection and the genesis of TCs, even though the thermodynamic conditions are favorable for TC genesis.

In contrast, more TCs are generated in PD than are observed over the Arabian Sea, the Central and Eastern North Pacific, near the Island of Madagascar, and north of Australia (Fig 3.1c). The relative humidity is favorable for TC formation over these ocean sub-basins, and vertical wind shear is also favorable with the exception of the north of Australia. In the NICAM simulation, it is appeared that the effect of vertical wind shear is larger than those of the other components of *EGPI*.

3.3 Interannual variability

As emphasized by Walsh et al. (2014), GCMs cannot adequately predict the interannual variability in TC formation in different ocean basins. Improving these models is important to capture the essential physical relationships that link TCs to climate. The interannual variabilities in annual TC formation determined in recent high-resolution AGCM studies (Manganello et al. 2012; Murakami et al. 2012; Strachan et al. 2013; Roberts et al. 2015) correlate well with observation. The degree of

correlation differs among ocean basins, being higher in the North Atlantic basin than in the other basins.

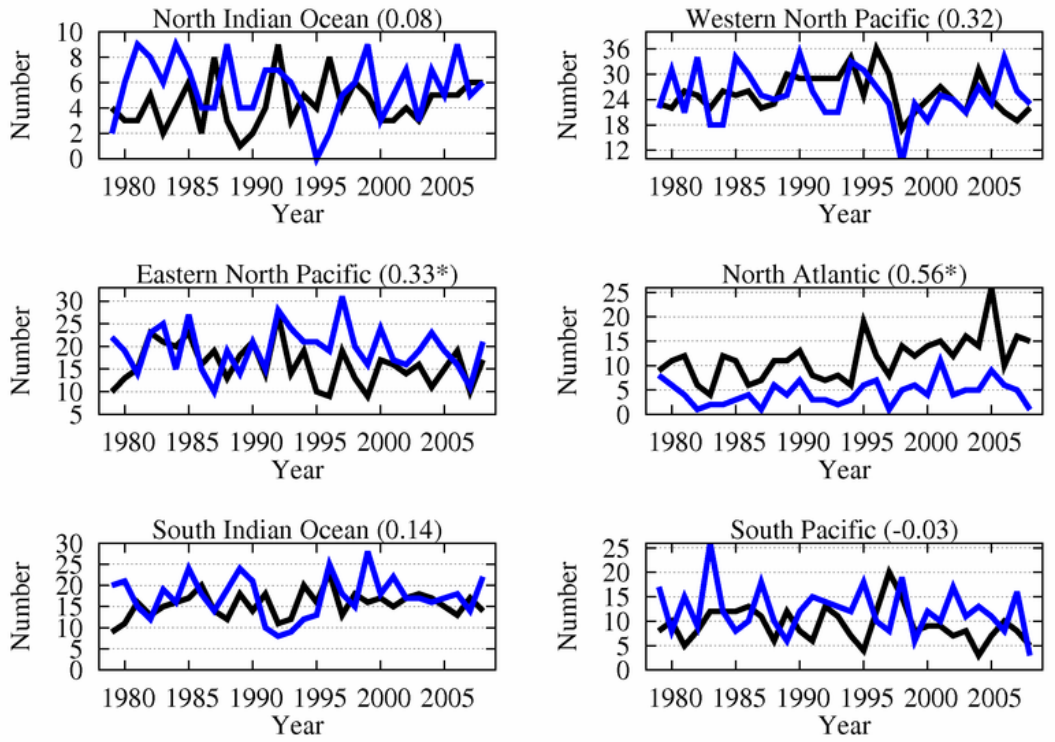

Fig. 3.5. Interannual variability in TC genesis in each ocean basin, as defined in Fig. 3.1. The results of IBTrACS and the PD simulation are plotted in black and blue, respectively. Correlation coefficients between IBTrACS and PD are given in parentheses for each ocean basin. Asterisks indicate that the correlation coefficient is statistically significant at the 95% level (Pearson's product-moment correlation significance test).

Figure 3.5 shows the interannual variability in TC genesis in each ocean basin; the corresponding correlations between the present-day simulations and observations are also given in parentheses. The correlation coefficients are statistically significant at the 95% level (Pearson's product moment correlation significance test) over the Eastern North Pacific and North Atlantic. The higher correlation in the North Atlantic than in the other basins is echoed in the NICAM results. Strachan et al. (2013) reported that the number of TCs in the North Atlantic depends on the underlying SST. The present-day

simulation follows the AMIP experiment but employs a slab-ocean model. Nonetheless, the simulated sea surface forcing matches the observations. Therefore, among the six ocean basins, the correlation between the simulated and observed interannual variability is highest in the North Atlantic.

3.4 Intensity

Simulated TC intensities are sensitive to the model resolution (Manganello et al. 2012). Figure 3.6 shows the present-day simulated and observed probability density functions of the lifetime maximum wind speeds at a height of 10 m. The intensities of the TCs in the present-day simulation only just exceed Category 4 (more than 59 m s^{-1}) on the Saffir–Simpson Hurricane Scale. The TCs with the strongest wind speeds appear not to be simulated, while those with intensities between 30 and 50 m s^{-1} are overrepresented. Observational studies have shown that the horizontal scale of weak and intense TCs is smaller than that of moderate TCs (Weatherford and Gray 1988). The discrepancy was also reported in Zhao et al. (2009), who used a lower-resolution (50-km) mesh compared to the PD. They documented that a resolution of 50-km is not sufficient to resolve storm intensity. It appears that the 14-km mesh employed in the PD is still insufficient to resolve small TCs.

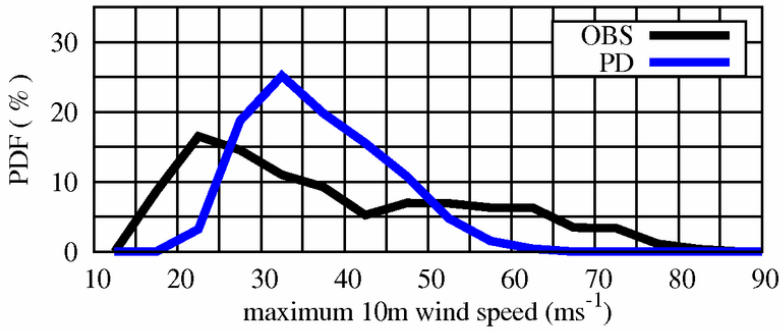

Fig. 3.6. Probability density function (PDF) of the lifetime maximum wind speed at a height of 10 m (m s^{-1}). The bin width is 5 m s^{-1}. The results of IBTrACS (OBS) and the PD simulation are plotted in black and blue, respectively.

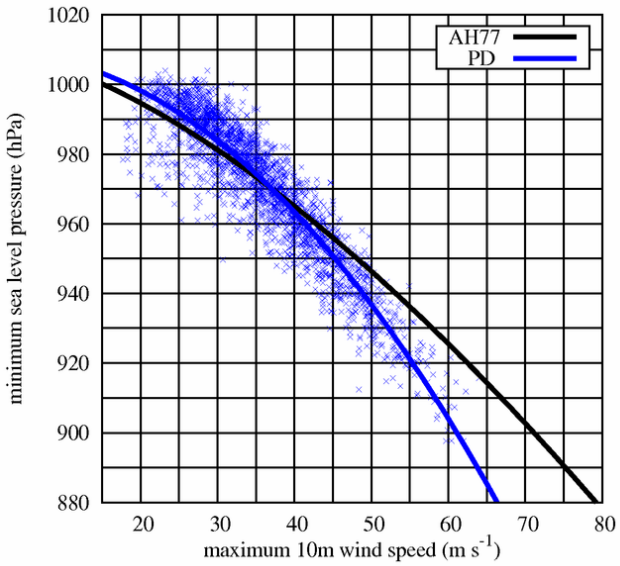

Fig. 3.7. Scatter diagram of lifetime minimum central SLP (hPa) versus maximum 10-m wind speed (m s^{-1}) for TCs simulated by the PD simulation (blue crosses). The blue curved line is the second-order polynomial fit to the data points. The black line shows the empirical relationship between the central SLP and maximum wind speed based on observed data (Atkinson and Holiday 1977).

Considering the gradient wind balance, we speculated that as central SLP decreases, the pressure gradient at RMW would increase when RMW remains unchanged. However, the relationship between the maximum wind speed and minimum

SLP is parabolic because RMW changes with the individual TC. This relationship was documented by Atkinson and Holliday (1977). Comparing the NICAM-simulated and empirical relationships (Atkinson and Holliday 1977) between the maximum wind speed and minimum SLP, we found that NICAM underestimates the maximum wind speed of intense TCs (see Fig. 3.7). Similar biases in the relationship between maximum wind speed and minimum SLP have been reported in previous studies that employed horizontal grid intervals of 7 km (Satoh et al. 2012), 10 km (Manganello et al. 2012), and 20 km (Murakami and Sugi 2010). Refining the horizontal grid spacing and parametrizing the cumulus are known to reduce this bias (Manganello et al. 2012; Murakami et al., 2012; Roberts et al. 2015). By reducing the horizontal grid spacing, this bias is also alleviated in the NICAM simulations, as will be illustrated in Chapter 6 (Fig. 6.2).

Chapter 4 Response of Tropical Cyclone Activities to Global Warming

Using the outputs of the PD and GW, we show future changes in TC activities, including the geographical distribution TC genesis, the seasonal cycle of TC genesis, and TC intensity. In Chapter 4.1, we discuss the relationship between TC genesis and large-scale environmental conditions using a genesis potential index, (*EGPI*; Emanuel and Nolan 2004). The response of TC intensity to global warming is described in Chapter 4.2.

4.1 Genesis and large-scale environmental conditions

Figure 4.1 shows the geographical distribution of TCs formed in the GW simulation and compares it to the distribution determined in the PD simulation. Global warming reduces the annual formation rate of TCs around the globe; the rate increases only in the South Pacific (Table 4.1). Differences marked with * and ** in Table 4.1 are statistically significant at the 90% and 95% confidence levels, respectively (two-sided Welch's *t*-test; Welch 1947). Welch's *t*-test assesses the statistical significance of difference between means of samples that have non-homogeneous sample variances. The variances of TC genesis are not necessarily the same between the present-day and future climate conditions; thus, we used the Welch's *t*-test instead of the Student's *t*-test.

The globally averaged frequency of TCs is reduced by 23.2% under warmer conditions (Table 4.1), which is within the uncertainty (6−34%) reported by Knutson et al. (2010). Satoh et al. (2015) proposed a mechanism for this global reduction, as

described in Chapter 1.1.

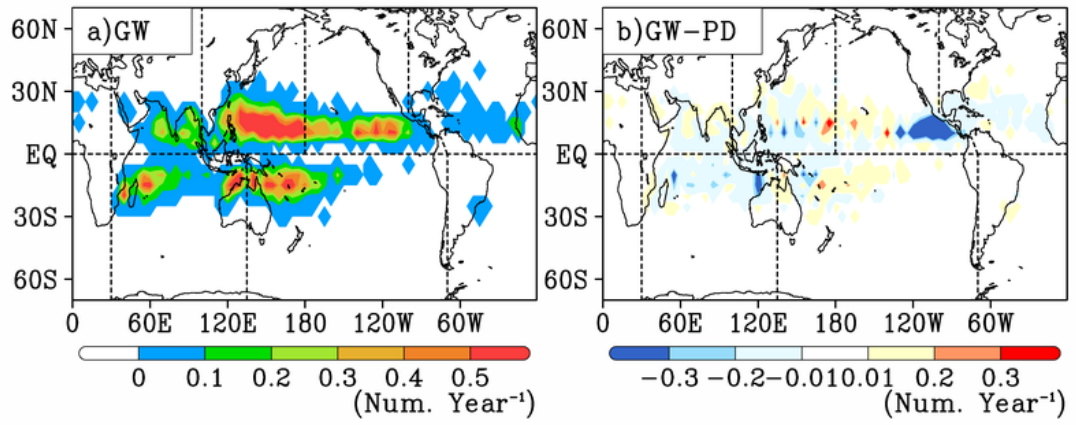

Fig. 4.1. Geographical distribution of the density of annual TC genesis between 2075 and 2104 in the GW simulation. The genesis density is defined as the number of cyclones per year formed in each 5° × 5° grid box. Panels (a) and (b) plot the GW results and their differences from the PD simulation, respectively. The dotted lines separate the six ocean basins. The boundary between the eastern North Pacific and North Atlantic lies along Central America.

Table 4.1. Frequencies of annual TCs in the GW simulation and their differences (DIFF) from the PD simulation. The regions are the North Indian Ocean (NIO), the western North Pacific (WNP), the eastern North Pacific (ENP), the North Atlantic (NA), the South Indian Ocean (SIO), and the South Pacific (SP) basins; the Northern and Southern Hemispheres (NH and SH, respectively); and the entire globe (GL). The ocean basins are delineated in Fig. 4.1. Differences marked with * and ** are statistically significant at the 90% and 95% confidence levels, respectively (two-sided Welch's *t*-test).

	NI	NWP	NEP	NA	SI	SP	NH	SH	GL
GW (Num.)	5.0	22.2	12.1	1.9	10.9	12.6	41.1	23.7	64.8
DIFF (%)	−11.3	−11.4**	−38.1**	−58.2*	−37.2**	2.8	−24.8**	−20.4**	−23.2**

All ocean basins show reductions in TC genesis with the exception of the South Pacific. The distribution of TC genesis shifts eastward over the South Pacific, and TC genesis decreases around Australia and increases over the central South Pacific. The

sum of TCs over both sub-basins is slightly more than that determined by the PD; however, this increase (+2.8%) is not statistically significant. Figure 4.1 shows that the reduction in genesis density is predominant off the shore of Central America over the eastern North Pacific.

Over the western North Pacific, the frequency of TC generation decreases in the western part of the western North Pacific and increases in the central North Pacific. Similar responses were documented by analyzing the outputs of CMIP3 models (Yokoi and Takayabu 2009). They revealed that the increase in the central North Pacific is caused by the relative vorticity in the lower troposphere and weak vertical wind shear, which are favorable for TC genesis, and the authors speculated that the decrease in the western part of the Western Pacific is associated with a weakening in the activity of tropical depression-type disturbances, which can be precursors to TCs. These favorable conditions in the central North Pacific are similar to the environmental conditions seen during El Niño. Chan (1985) showed that under El Niño conditions, the frequency of TC generation decreases over the western North Pacific but increases over the central North Pacific. In the GW simulation, future changes in SST estimated from the CMIP3 multi-model ensemble mean showed an El Niño-like distribution. Thus, we suggest that the future difference between the PD and GW results is analogous to the response of TCs to El Niño conditions.

TC formation is sensitive to large-scale environmental conditions (e.g., horizontal and vertical wind shear, thermodynamic instability, and humidity). As mentioned in Chapter 3.2, Emanuel and Nolan (2004)'s GPI (*EGPI*) does not include a specific threshold value in the thermodynamic component. Therefore, *EGPI* is applicable to assess TC response to global warming (Yokoi et al. 2009). However,

Wehner et al. (2015) warned that it is unsafe to employ *EGPI* to predict TC formation under global warming conditions because the constants in *EGPI* are not necessarily appropriate for warmer climates. Thus, *EGPI*'s applicability to warmer climates remains controversial, although the components of *EGPI* account for future change in TC formation. To explore the regional changes in TC formation, we calculated the *EGPI* (defined as Eq. 3.1) from the outputs of the GW as well as the PD. This analysis was limited to the active seasons of the various ocean basins, as indicated in Figs. 3.2 and 3.3.

Figure 4.2 depicts the geographical distributions of the seasonal mean *EGPI* (Fig. 4.2a) and its components (Figs. 4.2b–e). The numbers 1, 2, and 3 appended to the alphabetical symbols refer to the PD, GW, and future change, respectively. Global warming increases the *EGPI* over all ocean basins except for the North Atlantic (Fig. 4.2, a3). In general, these changes contradict the reduction in TC formation (Fig. 4.1b). The global *EGPI* seems to increase because its components, relative humidity (Fig. 4.2, c3) and potential intensity (Fig. 4.2, b3), both increase. The relative humidity and potential intensity are sensitive to changes in SST. Wehner et al. (2015) reported similar findings.

The *EGPI* predicts decreases in TC formation over the North Atlantic, and the components of the *EGPI* are partially consistent with the regional changes in TC formation. The vertical wind shear (Fig. 4.2, e3) and absolute vorticity (Fig. 4.2, d3) components actually decrease. For instance, over the eastern part of the eastern North Pacific, the density of generated TCs is significantly reduced, which is consistent with the decrease in the absolute vorticity and increase in vertical wind shear. This may indicate that it is necessary to adjust the constants in *EGPI* for warmer conditions, as

discussed in Wehner et al. (2015). The adjustment of the constants in *EGPI* is beyond the scope of this study. Thus, we focus on the relationships between future changes in the frequency of TC formation and the components of the *EGPI*.

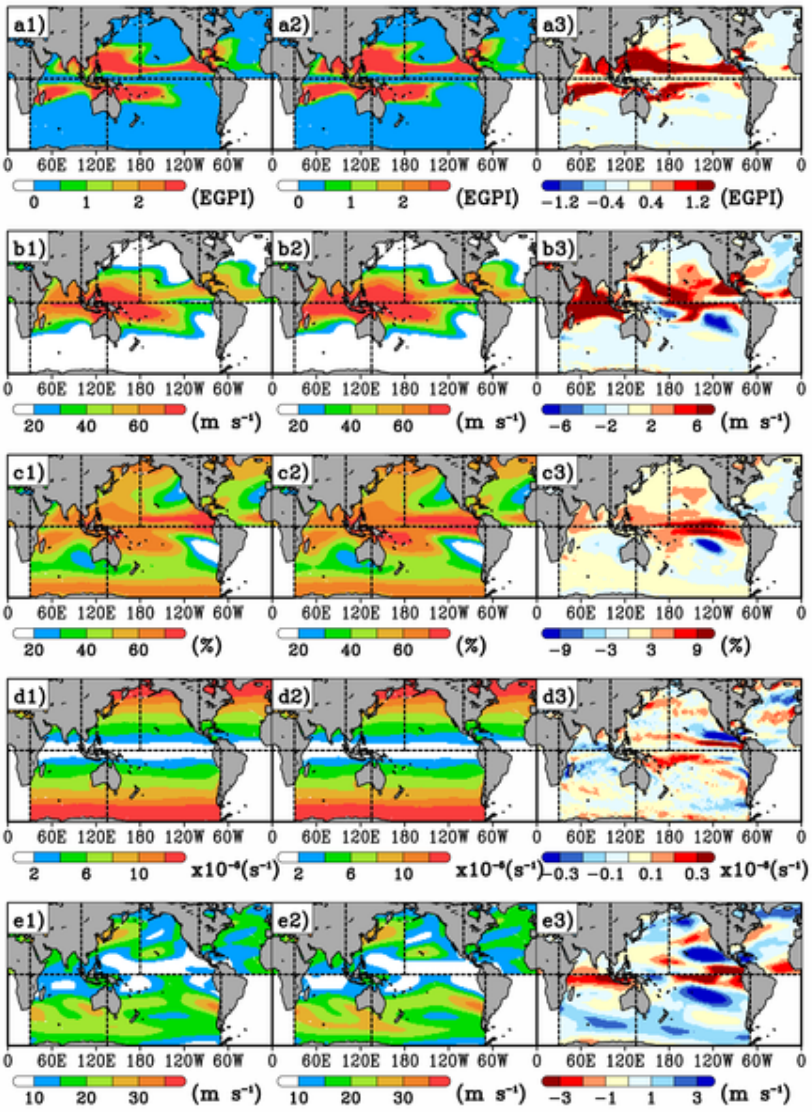

Fig. 4.2. Seasonal mean *EGPI* and its components in six ocean basins during their active seasons of TC formation computed from the PD and GW simulations. The active seasons are the same as those in Fig. 3.3 for the respective ocean basins. Panel (a) plots *EGPI*, panels (b), (c), (d), and (e) plot the potential intensities (m s^{-1}), relative humidity at 700 hPa (%), absolute vorticities (s^{-1}), and magnitudes of vertical wind shear (m s^{-1}), respectively. The numbers 1, 2, and 3 appended to each alphabetical symbol refer to PD, GW, and their difference, respectively. The dotted lines are those of Fig. 3.1.

The contributions of the *EGPI* components vary among the ocean basins. For instance, the geographical distributions of the changes in the potential intensity and vertical wind shear resemble those of the reduced TC genesis around the Philippines, while the distributions of all components are consistent with the increased genesis over the central North Pacific. The responses over the central North Pacific are similar to the responses to El Niño, as described at the beginning of this subchapter.

As mentioned in previous studies (McDonald et al. 2005; Sugi et al. 2009; Mori et al. 2013), the regional changes in TC genesis are related to changes in large-scale atmospheric circulation, which is dominated by the geographical distribution of the SST. Although *EGPI* tends to overestimate the formation of TCs because of the potential intensity, the components of *EGPI* account for the relationship between TC genesis and large-scale environmental conditions.

4.2 Intensity

Herein, TC intensity is categorized by the central SLP rather than using the official Saffir–Simpson hurricane scale which categorized TC intensity by the maximum wind speed. Following Roberts et al. (2015), we define the intensity categories as follows: C0 (> 994 hPa), C1 (980–994 hPa), C2 (965–979 hPa), C3 (945–964 hPa), C4 (920–944 hPa), and C5 (< 920 hPa). Table 4.3 lists the number of TCs at their lifetime minimum central SLPs in each category. Relative to the PD, the GW projects a decrease in the number of C0–C3 cyclones and an increase in the number of C4 and C5 cyclones. These findings are consistent with previous studies (Knutson et al. 2010; IPCC 2013). The frequency of C5 cyclones is expected to increase by 50% under global warming conditions. Figure 4.2, b3 shows that the potential intensity increases

over almost all ocean basins. This indicates that TC intensity increases under global warming conditions, as expected.

Table 4.2. TC frequencies categorized by lifetime minimum central SLP (Pc). Results are presented for the PD and GW simulations. The rate of change defines the difference in frequency between the GW and PD simulations relative to the frequency in the PD simulation.

Category	Central pressure	PD	GW	Change rate
C5	Pc < 920	34	51	50.0%
C4	920 ≦ Pc < 945	268	271	1.1%
C3	945 ≦ Pc < 965	567	408	−28.0%
C2	965 ≦ Pc < 980	686	464	−32.4%
C1	980 ≦ Pc < 994	732	575	−21.4%
C0	994 ≦ Pc	245	175	−28.6%

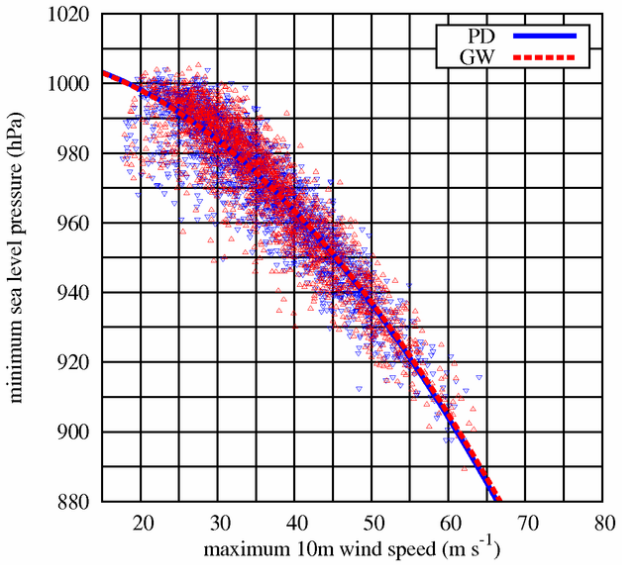

Fig. 4.3. Scatter diagram of lifetime minimum central SLP (hPa) versus maximum 10-m wind speed (m s^{-1}) for TCs determined by the PD (blue reversed triangles) and GW (red triangles) simulations. The blue and red curved lines are the second-order polynomial fits to the data points of both simulations.

Figure 4.3 depicts the relationships between the maximum wind speed and minimum SLP in the PD and GW. These relationships are almost the same in both simulations. Considering the gradient wind balance equation, this fact indicates two possibilities: either the radial distribution of pressure and RMW are unchanged or both change under warmer conditions. In the next chapter, we discuss changes in RMW and the radial distribution of pressure due to global warming.

Chapter 5 Response of Tropical Cyclone Structure to Global Warming

In this chapter, we investigate the effects of global warming on TC structure. Chapter 5.1 and 5.2 show the responses of TC vertical structure and water content, respectively. These results have been described in Yamada et al. (2010) and Yamada and Satoh (2013); however, all results are reconstructed using the output of Kodama et al. (2013) since their simulation offered a larger sample of TCs than those of Yamada et al. (2010) and Yamada and Satoh (2013).

Chapter 5.3, we elucidate how horizontal TC structures such as the distribution of tangential wind and RMW respond to global warming. Observational studies have noted that the variation of TC structure is large (Weatherford and Gray 1988; Kimball and Mulekar 2004). Herein, we compare the composite structures of TCs with the same intensities between the present-day and warmer climates.

5.1 Top height of the eyewall cloud

One advantage of explicitly calculating the cloud is that the model results reveal the mesoscale properties of the cloud. Figure 5.1 relates the minimum central SLP to the explicitly simulated cloud top height for all TCs at their lifetime maximum intensity. The more intense the cyclone, the higher its cloud top; moreover, cloud tops in the GW simulation become taller than those in the PD (as evidenced by the upward shifts of the best-fit regression line). This difference between the mean heights in both

simulations is statistically significant at the 99.9% confidence level (two-sided Welch's *t*-test; Welch 1947). It also supports the results of a regional model that revealed the upward shift of the warm core maximum under global warming (Knutson and Tuleya 1999).

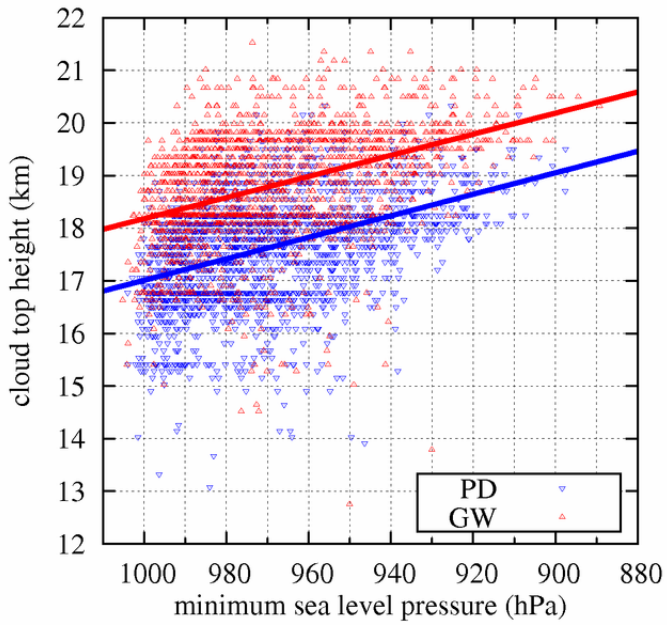

Fig. 5.1. Scatter plots of cloud top height versus minimum central SLP for the simulated TCs. Since vertical grid intervals are coarse at upper levels in the model, the cloud top height is estimated by linearly interpolating the vertical layer. The blue inverted and red upright triangles indicate the PD and GW simulations, respectively. The linear regression equations of the PD (blue line) and GW (red line) are $f(x)$ = 37.4–0.0204x and $g(x)$ =38.2–0.0201x, respectively, where x denotes the minimum SLP (hPa). The cloud top height is defined as the highest altitude below which the sum of the ice and liquid hydrometeors (snow, graupel, cloud ice, and water contents) exceeds 1.0×10^{-5} kg kg^{-1} in at least 30 grid points in a 10° × 10° box.

These results are consistent with the Carnot heat engine framework conceptualized by Emanuel (1986, 1987), which predicts that global warming conditions increase the SST and boundary layer moisture (warm source) and consequently the intensities of TCs. A schematic of this framework is shown in Fig. 5.2. Air flowing inward gains heat from the warm ocean in the boundary layer. The updrafts

around the center of the TC reach the lower stratosphere or upper troposphere and form an eyewall. The air lifted by the updrafts is warmer than that in the environmental field due to condensation heating and finally loses its heat through radiative cooling. In this simple framework, the thermodynamic efficiency (ε) is defined as

$$\varepsilon = \frac{T_B - \overline{T}_{out}}{T_B}, \tag{5.1}$$

where T_B is the temperature at the top of the boundary layer and $\overline{T}_{out}$ is the average outflow temperature (as shown in Chapter 1.1). The thermodynamic efficiency of TC (a first-order approximation) is also affected by the cold sink associated with the TC outflow. As the atmosphere becomes more stabilized in warmer climates, the thermodynamic efficiency is reduced in the global warming simulation. However, higher TCs can also become more thermodynamically efficient, which would strengthen their intensities relative to present-day cyclones because atmospheric temperature decreases with altitude.

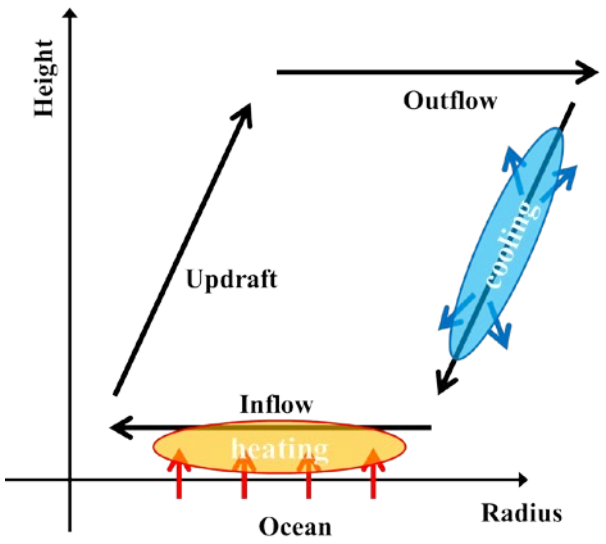

Fig. 5.2. Schematic of the Carnot heat engine framework based on Emanuel (1986).

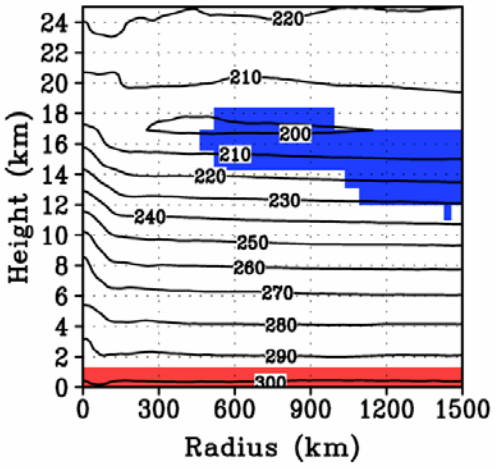

Fig. 5.3. Sample of the radius–height temperature cross sections of a matured TC in the present-day simulation. The blue-colored region is defined as the outflow region. The red-colored region is below 1.5 km in altitude.

In fact, we estimate the thermodynamic efficiency using Eq. 5.1. The outflow region is defined as a region in which the radial wind turns from the center of a TC to the outward direction. The swirling flow is counterclockwise (clockwise) circulation in the Northern (Southern) Hemisphere, and the absolute value of the product of the outflow and the swirling flow is more than 10 m^2 s^{-2}. The top of the boundary layer is defined as an altitude in 1.5 km. Figure 5.3 exemplifies the outflow regions of a mature TC, which is are colored blue. Figure 5.4 shows a scatter plot of the mean outflow temperature and the mean temperature at a height of 1.5 km as functions of minimum SLP.

Estimated thermodynamic efficiencies as function of minimum SLP are shown in Fig. 5.5. The average thermal efficiencies of matured TCs were 0.2604 and 0.2596 in the GW and PD, respectively. Thus, the thermal efficiency was almost unchanged under warmer conditions. Therefore, TCs in the GW must be taller than those in the PD to achieve to the same intensity as those in the PD.

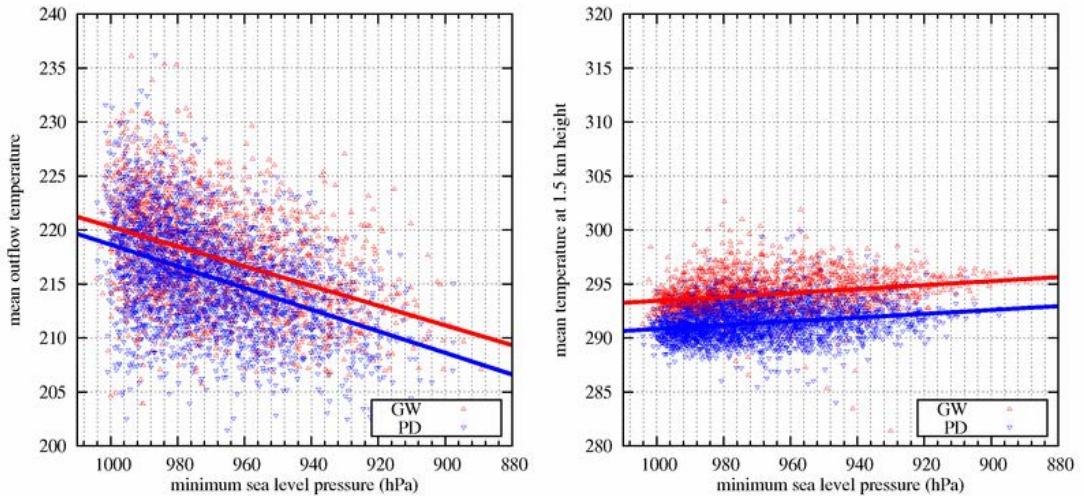

Fig. 5.4. Scatter plots of the mean outflow temperature (left) and the mean temperature at a height of 1.5 km (right) versus minimum SLP for the simulated TCs. The blue inverted and red upright triangles indicate the present-day simulation (PD) and the global warming simulation (GW), respectively. The blue and red lines show the regression lines of the PD and GW results, respectively.

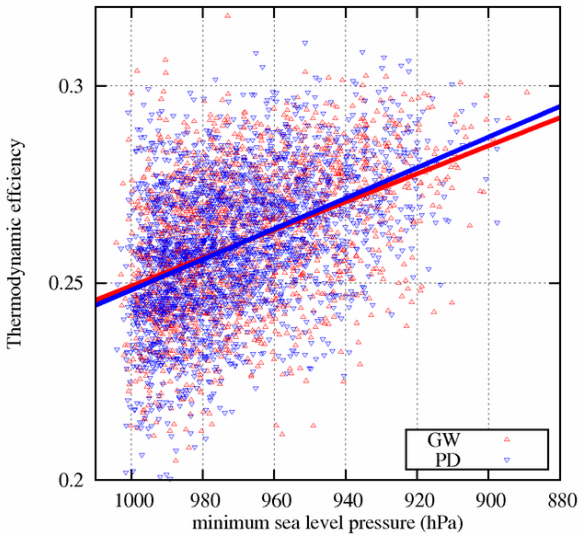

Fig. 5.5. Scatter plots of thermodynamic efficiency versus minimum SLP for the simulated TCs. The blue inverted and red upright triangles indicate the present-day simulation (PD) and the global warming simulation (GW), respectively. The regression line equations of the PD (blue line) and GW (red line) data are $f(x) = 0.636–0.039x$ and $g(x) =0.605–0.035x$, respectively, where x denotes the minimum SLP (Pa).

5.2 LWP and IWP associated with tropical cyclones

In the previous subchapter, we reported that the cloud tops of TCs become higher under warmer conditions. The rise of the eyewall should influence the ice and liquid water contents. Thus, we analyzed the radial distributions of the ice and liquid water paths (IWP and LWP, respectively) in the simulated TCs.

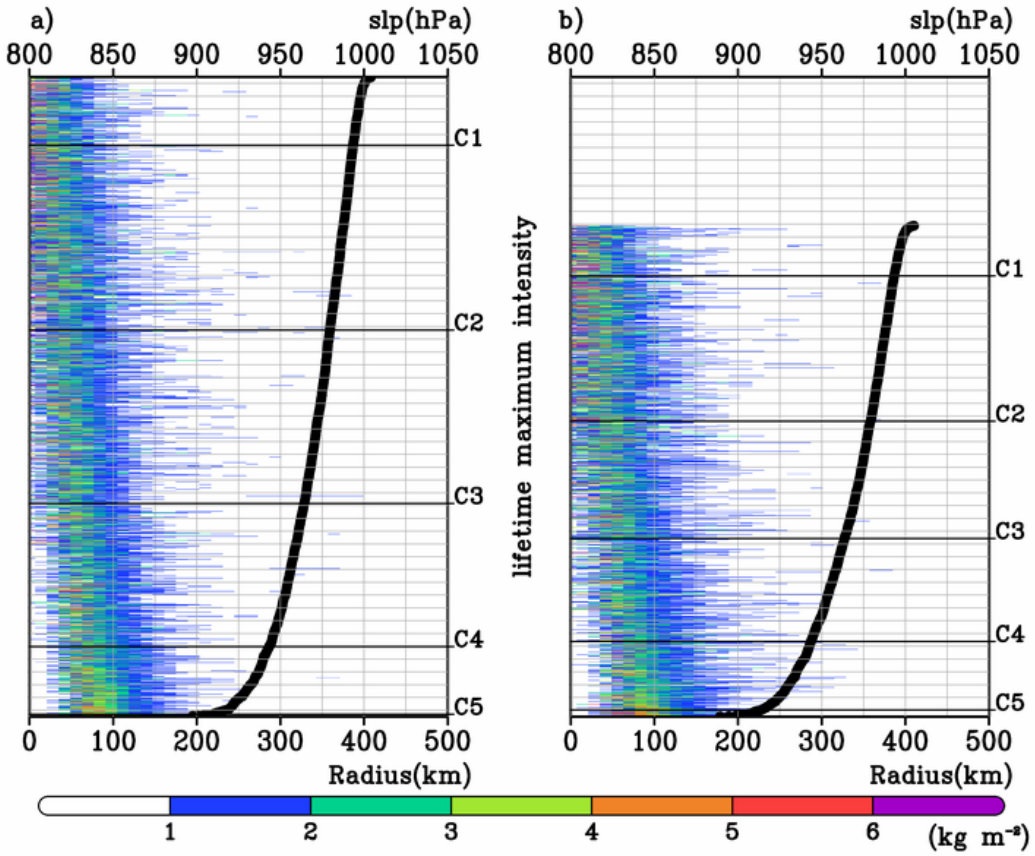

Fig. 5.6. Relationships between the minimum SLP and radial distribution of the tangentially averaged ice water path (IWP) in all simulated TCs at their lifetime maximum intensity obtained by the (a) present-day and (b) global warming simulations. The vertical axes represent separate TCs sorted by their SLP. Shades and dots show the amount of IWP (kg m^{-2}) and minimum SLP (hPa), respectively. The marks on the right vertical axes indicate intensity categories, as shown in Table 4.2.

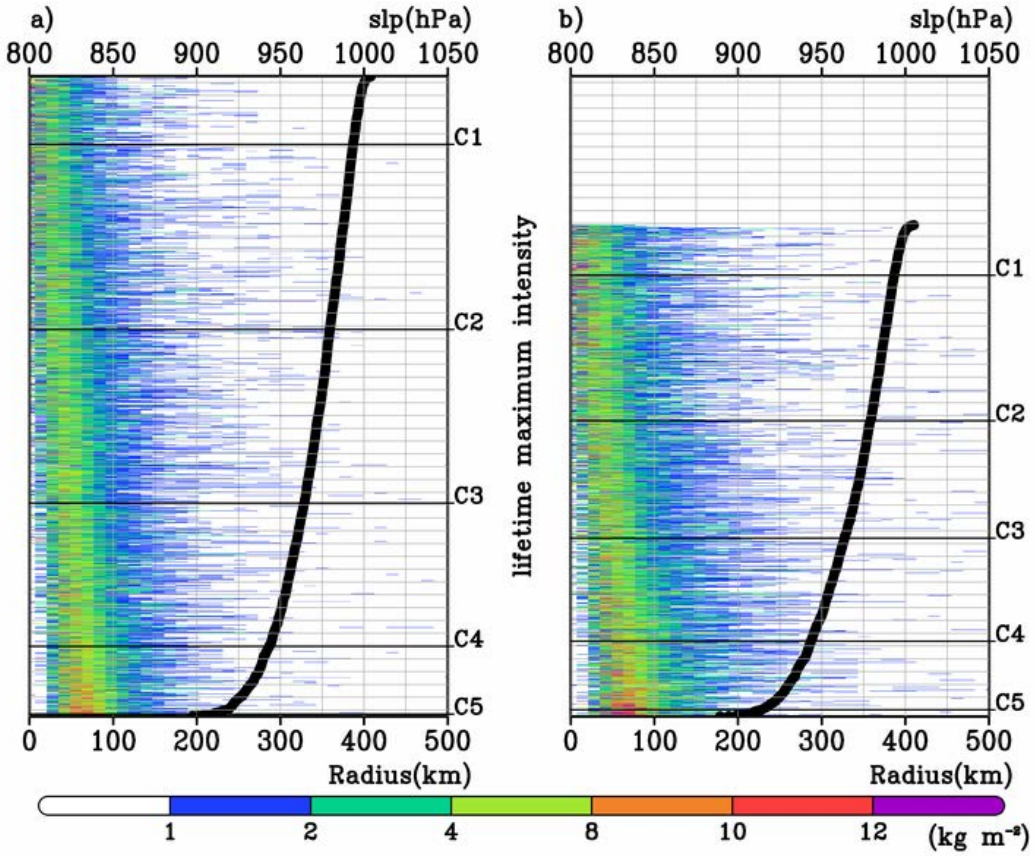

Fig. 5.7. Similar to Fig. 5.6, but for the liquid water path.

Figures 5.6 and 5.7 plot the radial distributions of the azimuthally averaged IWP and LWP, respectively, and the minimum central SLP of the individual TCs at their lifetime maximum intensities. In these plots, the vertical axes represent separate TCs ordered by their minimum central SLPs. The deepest SLPs in the PD and GW were 898 and 889 hPa, respectively. With respect to intense TCs more than C1 TCs, the maximum IWP (or LWP) locates almost at the eyewall in the radial direction. Precisely, the maximum IWP has a larger radius than the maximum LWP since the IWP mainly resides in the upper levels, and the eyewalls incline outward with increasing altitude. Later, we will demonstrate this phenomenon in a vertical structure of eyewall. For a moderately strong cyclone (less intense than C4 TCs), the radius of the eyewall

generally increases as the TC intensity increases (see Figs. 5.6 and 5.7).

As the SLP decreases further, the radius of the eyewall seems to be unchanged (Fig. 5.8). Using aircraft reconnaissance data, Weatherford and Gray (1988) found that the TC eyewall cloud widens proportionally with cyclone intensity and shrinks again in very intense cyclones. NICAM tends to reproduce Weatherford and Gray's (1988) findings, but does not completely simulate this feature because smaller, intense TCs are poorly resolved with the 14-km grid spacing. Thus, a quantitative discussion of the eyewall structure must be made with caution.

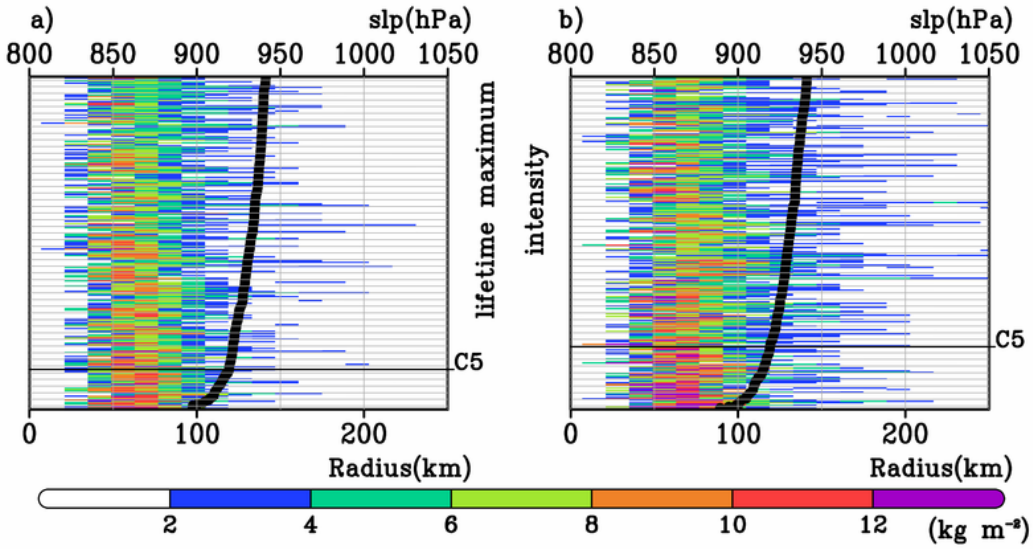

Fig. 5.8. Same as Fig. 5.7, but for the 250 most intense TCs.

Figure 5.9 shows composites of the IWP and LWP for the PD and GW, respectively. Comparing the PD and GW, we observe that the IWP and LWP increase under warmer conditions. However, the maximum radii of IWP and LWP vary with TC intensity. It seems that these variations neutralize changes in IWP and LWP. As discussed in Chapter 1.2, previous studies have reported that eyewalls locate relative to the RMW (Jorgensen 1984a, b). We normalized the IWP and LWP by their RMWs (Fig. 5.10).

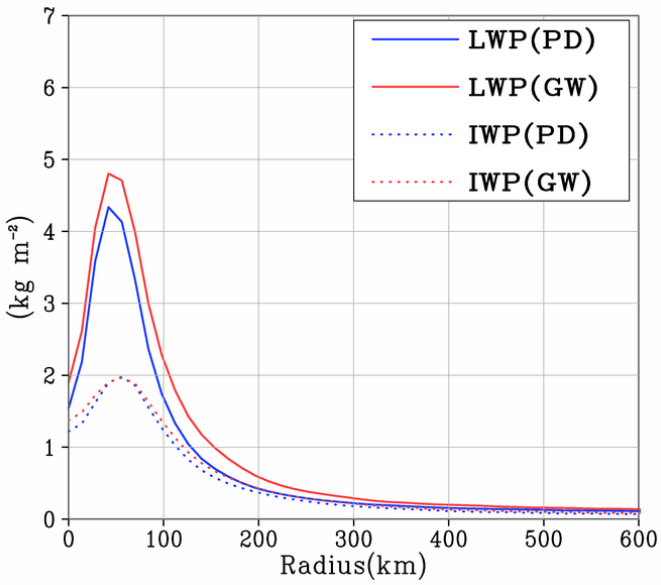

Fig. 5.9. Composites of the radial distributions of the ice water path (IWP) and liquid water path (LWP). Blue lines show the LWP (solid) and IWP (dotted) results in the PD simulation. Red lines show the LWP (solid) and IWP (dotted) results in the GW simulation.

Figure 5.10 is the same as Fig. 5.9 except that the radii are normalized by the RMW. The normalized radius of the maximum LWP is approximately 1.0; that is, the radii of the maximum LWP and maximum wind are almost equal, whereas the radius of the maximum IWP is larger (normalized radius = ~1.2). This indicates that NICAM reproduces the observed outward slope of the eyewall (Jorgensen 1984a, b; Stern and Nolan 2009; Hazelton and Hart 2013; Stern et al. 2014). The difference in LWP (IWP) between the PD and GW shows that LWP (IWP) is generally larger in the GW than in the PD, particularly the LWP in the outer edge of the eyewall.

Figure 5.11 shows the composite vertical structures of the ice water content (IWC) and liquid water content (LWC) in the PD and GW simulations. The isotherms are also shown. As the temperature increases in the GW, the vertical extent of the LWC increases, and the maximum LWC increases due to an increase in water vapor under

warmer conditions. The vertical extent of LWC and the increases in LWC explain why the maximum LWP increases from 5.1 to 6.0 kg m^{-2} (see Fig. 5.9).

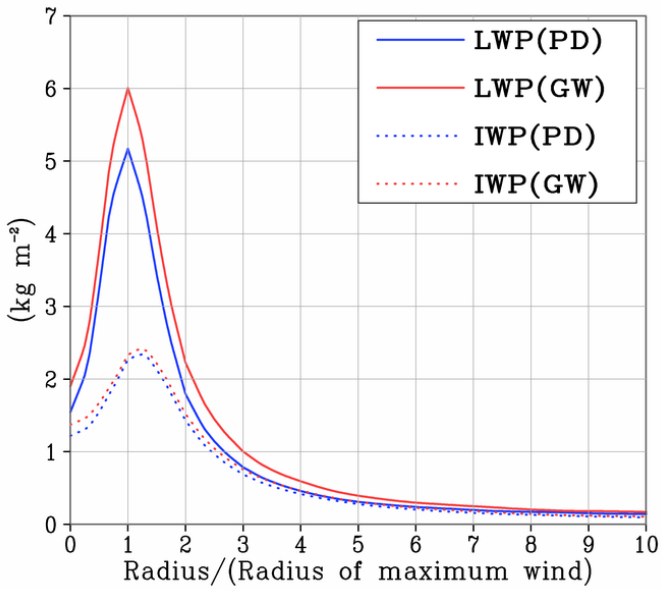

Fig. 5.10. Same as Fig. 5.9 except that the radius is normalized by the radius of maximum wind.

The maximum IWC also increases. In the GW simulation, the melting level (designated by the 0°C isotherm) and the tropopause height (−70°C isotherm) increase, but the vertical extent of the IWC does not change appreciably. Furthermore, the air density decreases with increasing height. Under these combined effects, the IWP increases to a lesser extent than the LWP; as shown in Fig. 5.9, the maximum IWP changes from 2.3 to 2.4 kg m^{-2}.

From Figs. 5.6–5.11, we can define the areas of the IWP and LWP associated with the TC and isolate them from the environment. We define the TC-IWP (or TC-LWP) as the horizontally averaged IWP (LWP) within 500 km of the TC center at its lifetime maximum intensity. This is because close to 500 km, the color shades in Figs. 5.6 and 5.7 almost vanish, implying that both IWP and LWP are reduced to below 1 kg m^{-2} at this radius. The IWP and LWP decrease to less than 5% of their peak values at

500 km (see Fig. 5.9).

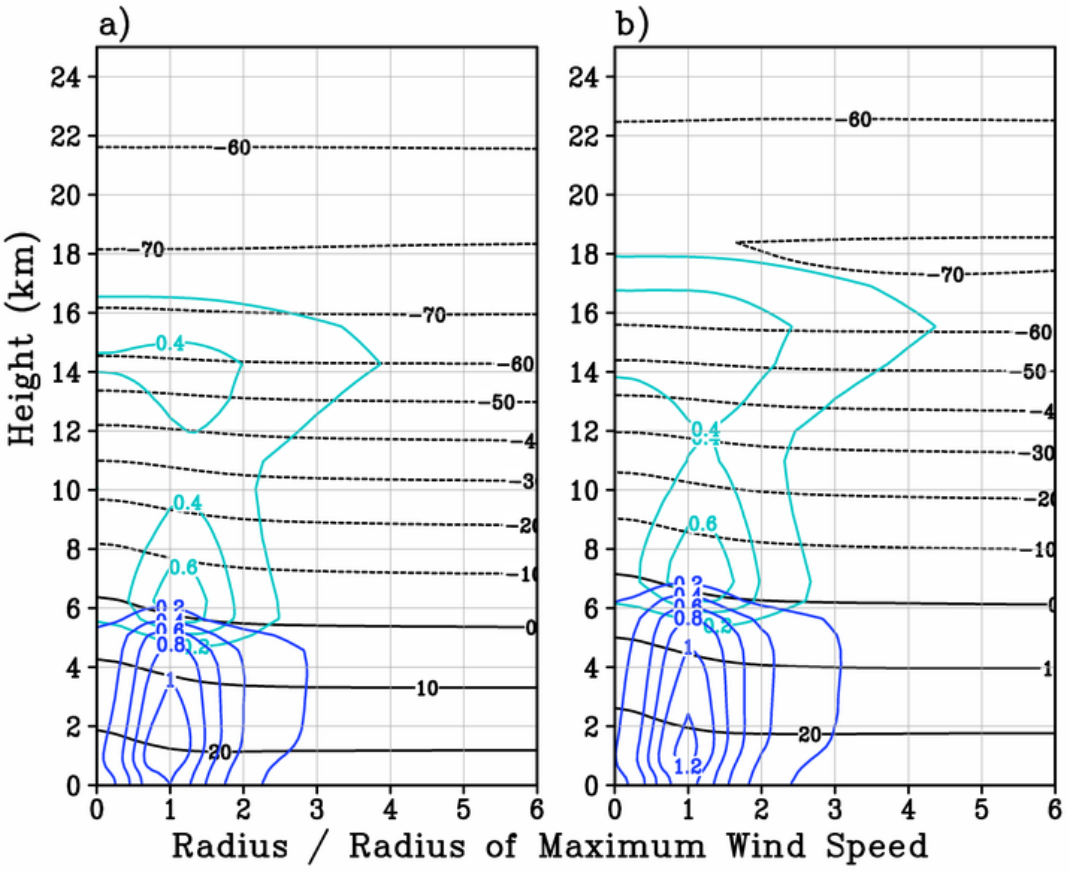

Fig. 5.11. Composites of the vertical structures of the ice and liquid water contents around each TC center in (a) the present-day and (b) global warming simulations. The light and dark-blue contours denote the ice and liquid water contents (g m^{-3}), respectively. The black contours show the isothermal (°C) values (the dotted contours are below-freezing-point values).

Figure 5.12 plots the relationships between the minimum SLP and TC-IWP (TC-LWP) in the PD (blue) and GW (red) simulations. Both TC-IWP and TC-LWP generally increase as the minimum SLP decreases, while large scatter is seen in these panels. Comparing the TC-IWP and TC-LWP trends in the PD and GW (Fig. 5.12), we find that in TCs of the same intensity, the TC-IWP and TC-LWP become more abundant under the warmer condition; the same result can be inferred from Figs. 5.11. The rise of the eyewall due to global warming increases the IWP and LWP, particularly the LWP.

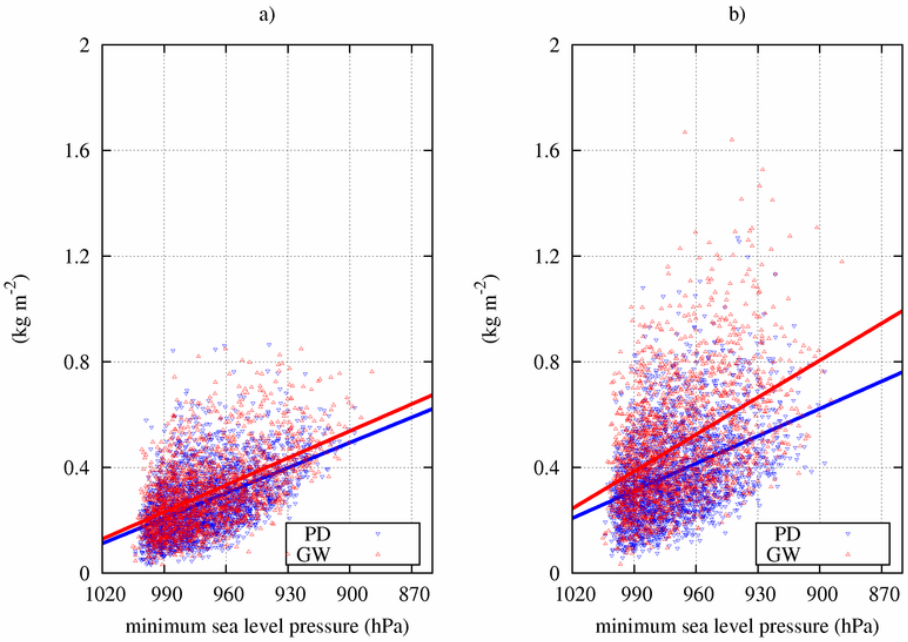

Fig. 5.12. Relationships between the minimum SLP and amount of (a) averaged ice water path and (b) averaged liquid water path in one TC. Solid lines denote the regression lines. The results of the PD and GW simulations are presented in blue and red, respectively.

5.3 Radial distribution of tangential wind velocity

Previous studies have revealed that the horizontal size of a TC reflects the stage in its life cycle and is also related to the surrounding environment and (to a lesser extent) the intensity of the cyclone (Merill 1984; Weatherford and Gray 1988; Chavas and Emanuel 2010, 2014; Miyamoto and Takemi 2013).

For instance, Miyamoto and Takemi (2013) depicted the variations in maximum wind speed and its radius from the stage of TC intensification to the mature stage using a RCM. In the intensification stage, the radius of maximum wind speed contracts while significantly fluctuating. The radius becomes nearly constant once the mature stage is reached. Furthermore, Merill (1984) showed that the mean horizontal size of a TC in the decaying stage is larger than that in the intensification stage,

although both intensities are similar.

In the previous subchapter, NICAM simulation showed that the RMW is approximately consistent with that of the maximum LWP (Fig. 5.10), which fluctuates with the minimum SLP (Figs. 5.6 and 5.7). This suggests that we should categorize TCs according to their intensity when discussing future changes in their horizontal sizes. In the present subchapter, *intensity* refers to the SLP at the cyclone center.

To distinguish structural changes in TCs due to fluctuations in their life cycles and global warming, we will focus on the lifetime maximum intensities of TCs throughout their life cycles and categorize the cyclones according to their intensity (categories listed in Table 4.2). Figure 5.13 depicts the radial distributions of the composite azimuthal mean tangential wind velocity at a height of 10 m (V_{T10}) from the cyclone center to around 200 km. The mean radii of the maximum V_{T10} in the PD and GW are in accordance for each cyclone intensity category. These radial distributions of V_{T10} show systematic responses to global warming with the exceptions of TCs in the C0 and C1 categories. The V_{T10} in the GW increases outside the radius of maximum V_{T10} (RMW10) (C5) or slightly outside (C2–4), and decreases inside, compared with the PD. This increase is more prominent as the intensity category is larger. The radial distribution of V_{T10} is associated with that of SLP through the gradient wind balance concept, although the effects of surface friction are not ignored within the boundary layer.

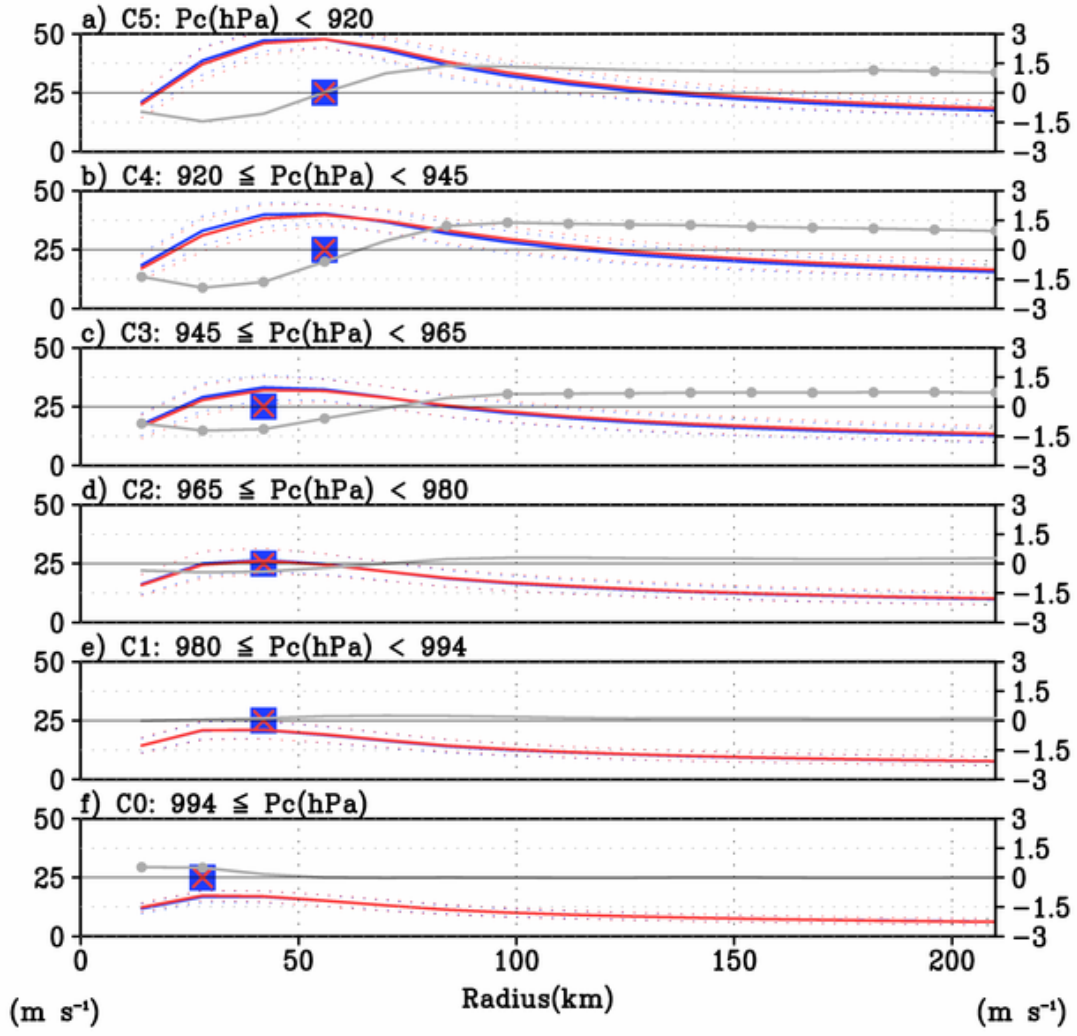

Fig. 5.13. Composite radial profiles of azimuthal mean 10-m tangential wind velocity (V_{T10}) of TCs in each intensity category at their lifetime minimum SLP. The signs of V_{T10} are reversed for TCs in the southern hemisphere. Blue and red solid lines denote the PD and GW, respectively, and these are scaled by the left y-axis. The dotted lines indicate the standard deviation of V_{T10}. The black lines are the differences in V_{T10} scaled by the right y-axes. The circles indicate a significant change at the 90% confidence level (two-sided Welch's *t*-test; Welch 1947). The panels show different intensity categories: (a) C0 (> 994 hPa), (b) C1 (980–994 hPa), (c) C2 (965–979 hPa), (d) C3 (945–964 hPa), (e) C4 (920–944 hPa), and (f) C5 (< 920 hPa). The blue squares and red crosses indicate the radius of the maximum V_{T10} for PD and GW, respectively.

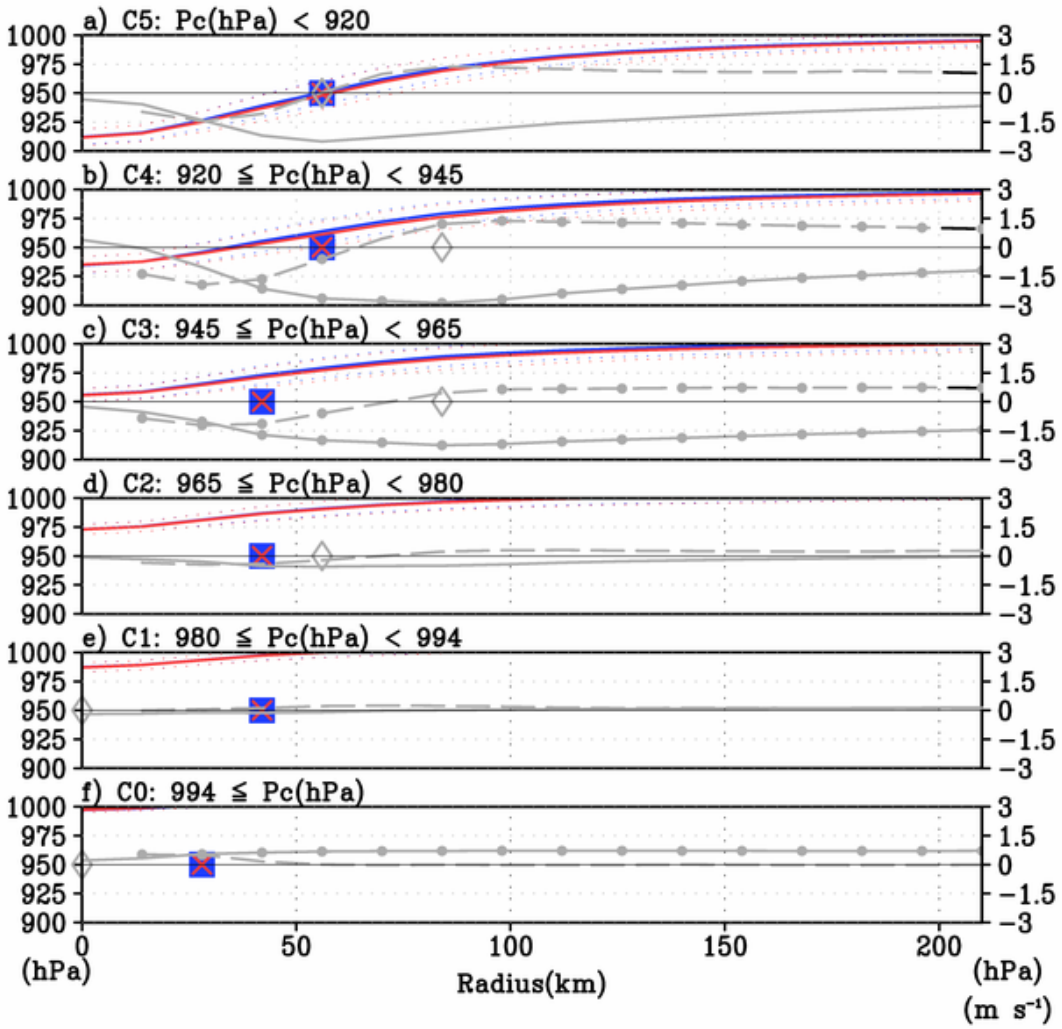

Fig. 5.14. As in Fig. 5.13 except for the SLP and diamonds indicate the radii of the maximum of SLP decrease. Dashed lines are the differences in azimuthal mean 10-m tangential wind velocity scaled by the right y-axes.

Figure 5.14 shows the radial distributions of the composite azimuthal mean SLP; RMW10s are superimposed with the blue squares and red crosses for the PD and GW, respectively. The radii of the maximum decrease in SLPs (RSLPs) are plotted on Fig 5.14 with diamonds for each intensity category. RSLPs correspond to RMW10 in C5, are larger than RMW10s in C2, C3, and C4, and correspond to the center of TCs in C0 and C1. The TCs in C3 and C4 show statistically significant differences in V_{T10} in the PD and GW simulations; V_{T10} in the GW simulation increases outside RSLP, and

decreases inside. We speculate that having a maximum value of decrease in SLP increases the pressure gradient outside RSLP and decreases it inside RSLP.

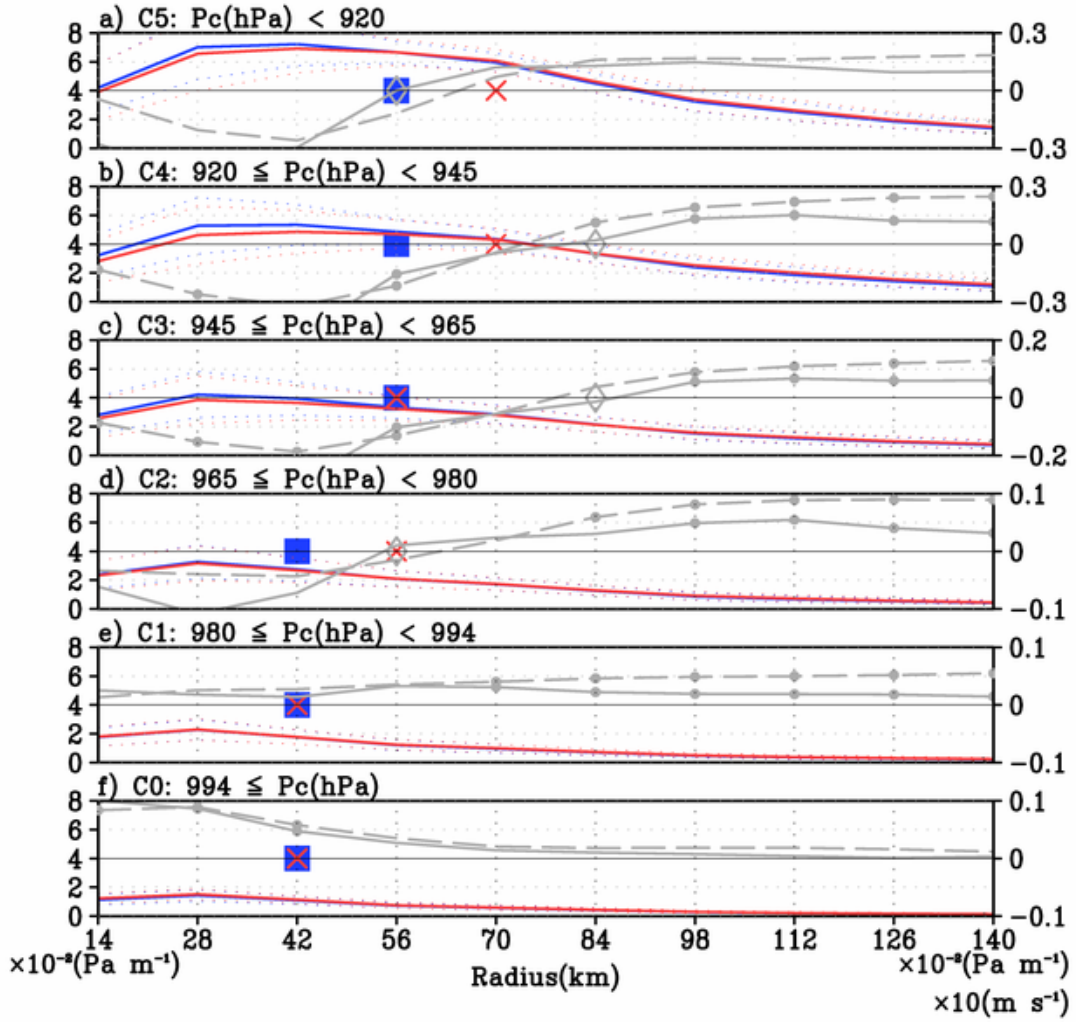

Fig. 5.15. As in Fig. 5.14 but for the radial gradient of pressure at a height of 1.5 km. Dashed lines are the differences in azimuthal mean tangential wind velocity at a height of 1.5km scaled by the right y-axes.

To verify this hypothesis, Fig. 5.15 reveals the distributions of the radial pressure gradient, on which radii of maximum tangential wind velocity (RMWs) and maximum decrease in pressure (RPSs) are superimposed. To neglect surface friction, these panels are plotted by using variables at a height of 1.5 km. These differences in pressure gradient show inverse signs inside and outside the RPS (as expected), as

indicated by a diamond for each intensity category.

In Fig. 5.15, the differences in the tangential wind velocity (V_T) at a height of 1.5 km between the GW and PD are depicted with the dashed lines. The signs of the differences in V_T are consistent with those of the pressure gradient at all radii except RPS. The gradient balance concept supports this result. At the same radius, the gradient balance equations for the present-day and future climate conditions are written as

$$\frac{V_{pd}^{\ 2}}{r} + f_{pd}V_{pd} = \frac{1}{\rho_{pd}}\frac{\partial P_{pd}}{\partial r} \tag{5.2}$$

and

$$\frac{V_{gw}^{\ 2}}{r} + f_{gw}V_{gw} = \frac{1}{\rho_{gw}}\frac{\partial P_{gw}}{\partial r}, \tag{5.3}$$

where V (m s^{-1}) is the gradient wind velocity, r (m) is the radius, P (Pa) denotes the pressure, f (s^{-1}) is the Coriolis parameter, and ρ (kg m^{-3}) is the density. Subscripts *pd* and *gw* refer to the present-day and global warming climate conditions, respectively. Differences in the radial gradient of pressure and Coriolis parameter are replaced as

$$\Delta\frac{\partial P}{\partial r} \equiv \frac{\partial P_{gw}}{\partial r} - \frac{\partial P_{pd}}{\partial r} \tag{5.4}$$

and

$$\Delta f \equiv f_{gw} - f_{pd}. \tag{5.5}$$

Subtracting Eq. 5.2 from 5.3, we obtain the difference in V:

$$\Delta V = V_{gw} - V_{pd}$$

$$= \left(\frac{V_{gw}+V_{pd}}{r} + f_{pd}\right)^{-1}\left[\frac{1}{\rho_{gw}}\frac{\partial P_{pd}}{\partial r}\left\{\frac{\rho_{pd}-\rho_{gw}}{\rho_{pd}} + \Delta\frac{\partial P}{\partial r}\left(\frac{\partial P_{pd}}{\partial r}\right)^{-1}\right\} - \Delta f V_{gw}\right] \tag{5.6}$$

It is obvious that the density, radius, and Coriolis parameter are positive values, while the radial gradient of pressure and gradient wind velocity are positive values in cyclonic

circulation. The sign of the difference in V_T is determined by the sum of the three terms in square brackets in Eq. 5.6. The first term in the square brackets in Eq. 5.6 is the product of pressure gradient force and the change rate of density (TERM1). The second term includes the rate of change of the pressure gradient and the pressure gradient force (TERM2). Finally, the last term is the product of *V* in GW and difference in the Coriolis parameters (TERM3).

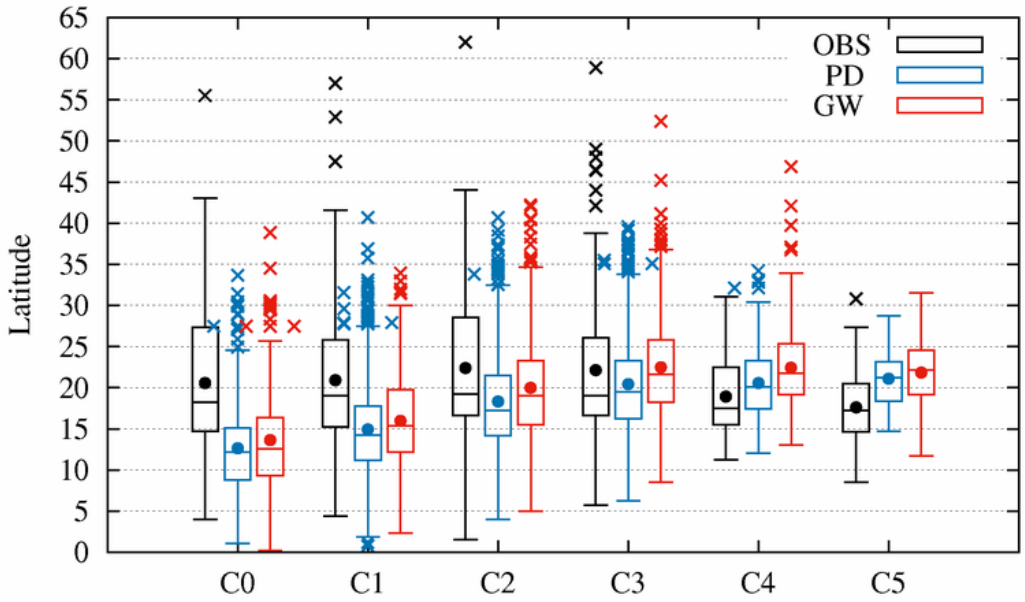

Fig. 5.16. Boxplot of latitudes where TCs achieve the minimum SLP in their life cycle stratified by the intensity categories. Black, blue, and red indicate observation (OBS), present-day simulation (PD), and global warming simulation (GW), respectively. Circles indicate the mean values. Crosses indicate outliers. OBS is calculated from a portion of IBTrACS because all data in IBTrACS do not include SLP. The sample number is 1046.

Comparing the magnitude of the three terms using the outputs of NICAM, we estimate which term dominates the difference between V_{pd} and V_{gw}. Figure 5.16 shows the latitudes where TCs achieve the minimum SLP in their life cycle stratified by the intensity categories. The mean latitudes in PD are more southward than those in OBS for C0−3 and more northward for C4 and C5. Table 5.1 lists the mean latitudes and

differences in the Coriolis parameter. The differences in the Coriolis parameter is an order of 10^{-6} s^{-1} [O (10^{-6} s^{-1})]. V_T is in ranges between 10−100 m s^{-1}. Thus, the TERM3 has a scale of O (10^{-5}–10^{-4} m s^{-2}).

Table 5.1. Lists of the mean latitude (degree) where TCs achieve the minimum SLP in their life cyclone stratified by the intensity categories (C0–5) for observation (OBS), the PD simulation, and the GW simulation. Diff (10^{-6} s^{-1}) indicates differences in the Coriolis parameter between PD and GW.

	C0	C1	C2	C3	C4	C5
OBS (º)	20.5	20.9	22.4	22.1	18.9	17.6
PD (º)	12.6	14.9	18.3	20.4	20.5	21.1
GW (º)	13.6	16.0	20.0	22.5	22.4	21.8
Diff (s^{-1})	2.48 × 10^{-6}	2.70 × 10^{-6}	4.09 × 10^{-6}	4.97 × 10^{-6}	4.50 × 10^{-6}	1.66 × 10^{-6}

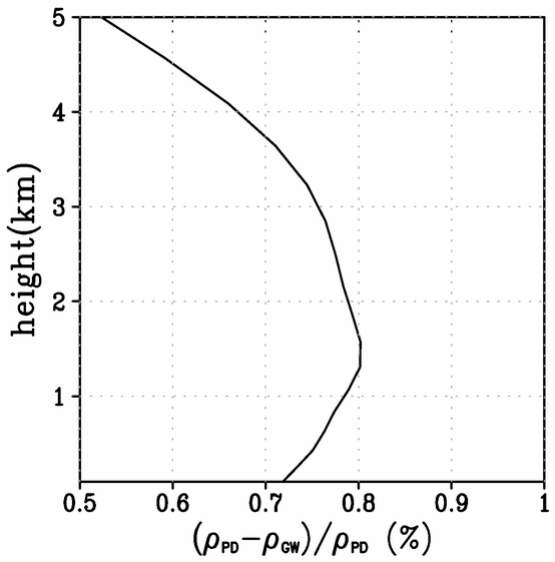

Fig. 5.17. Vertical profile of the change rate of density between present-day and global warming simulation.

With respect to the TERM1, the densities in PD and GW are nearly equal to one. Thus, the pressure gradient force has a magnitude of O (10^{-3} m s^{-2}; Fig. 5.15). The change rate of the mean density over the tropics (30° S–30° N) between the PD and GW

is less than 1%, and its magnitude is *O* (1%; Fig. 5.17). The first term has a scale of *O* (10^{-5} m s^{-2}).

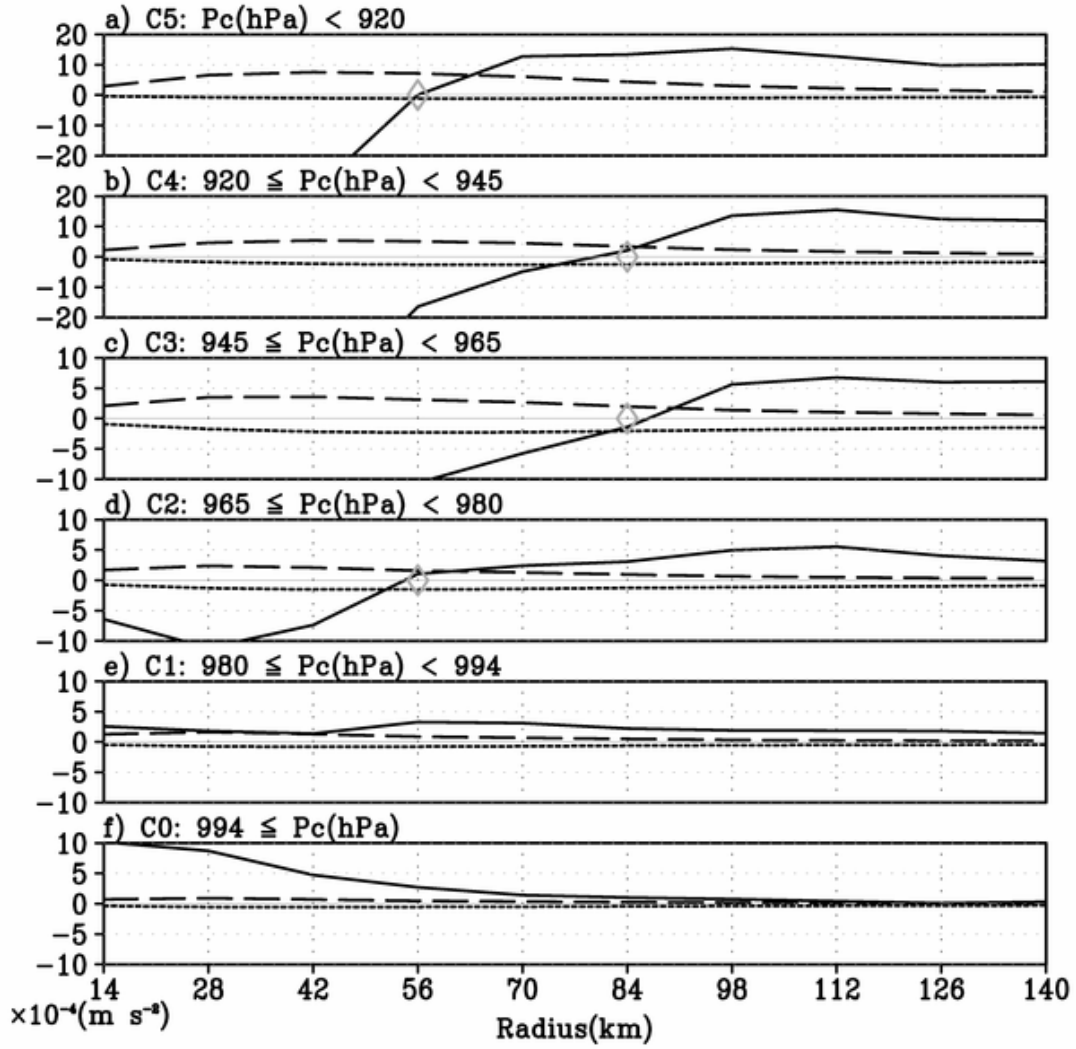

Fig. 5.18. Composite radial profiles of the first (long dashed lines), second (solid lines), and third (dashed lines) terms in the square brackets of Eq. 5.6 in each intensity category at their lifetime minimum SLP. These terms are calculated from the PD and GW simulations at a height of 1.5 km. Differences in the Coriolis parameter are listed in Table 5.1. Diamonds indicate RPS.

TERM2 includes the rate of change of the pressure gradient. Figure 5.15 shows that the rate of change varies with radius. To compare magnitude among the three terms, Fig. 5.18 depicts radial distributions of the three terms calculated from outputs of

NICAM simulations. The amplitude of the second term is the largest among the three terms, except for around RPS. Thus, future change in pressure is consistent with changes in V_T or V_{T10}; V_T increases outside RPS and decreases inside RPS (Figs. 5.14 and 5.15).

Next, we examine why distribution of pressure changes due to global warming. As reported in Chapter 5.2, NICAM simulations demonstrated that the RMW is in accordance with the maximum LWP and lies inside the maximum IWP (Fig. 5.10). In observed TCs, the RMW is located within the eyewall, which slopes outward with height (Jorgensen 1984b). NICAM reproduces this relationship between the RMW and eyewall.

As described in Chapter 5.1, NICAM simulations projected that the height of the eyewall cloud top increases under warmer climates; this phenomenon is associated with the rise of the tropopause caused by global warming (Manabe and Strickler 1964; Manabe and Wetherald 1967). The increase in eyewall cloud top height may contribute to altering the distribution of pressure surrounding a TC. TCs in categories C4 and 5 exhibit apparent changes in SLP (Fig. 5.14) and V_{T10} (Fig. 5.13). Since the number of samples in C4 is larger than that in C5 (Table 4), we focus on C4 cyclones in the subsequent analysis.

Figure 5.19 shows the composite radius-height cross-sections of water contents (g kg^{-1}) for TCs in category C4. Changes in the radial direction are shown below the melting level (designated by the 0^{o}C isotherm with thin dotted lines in Fig. 5.19). These water contents increase (decrease) in the outer (inner) edge of the eyewall. This dipole structure indicates that the eyewall shifts outward due to global warming. Significant changes in the vertical direction are shown at the melting level and tropopause height

(thin dashed lines in Fig. 5.19). As tropopause height and melting level increase under warmer conditions, water contents increase in the upper troposphere and near the melting level, and decrease between the tropopause and melting level.

The water contents in Fig. 5.19 include stratiform and convective clouds. Diabatic heating is related to condensation heating due to convection. To focus on convective clouds, Fig. 5.20 depicts the radius-height cross-sections of diabatic heating (K s^{-1}). The diabatic heating for PD and GW is less than 1.0×10^{-3} (K s^{-1}) at altitudes above 13 km (PD; Fig. 5.20a) and 14 km (GW; Fig. 5.20b), respectively. Thus, the decrease in water content between the tropopause and melting level (Fig. 5.19b) is associated with the rise of stratiform clouds.

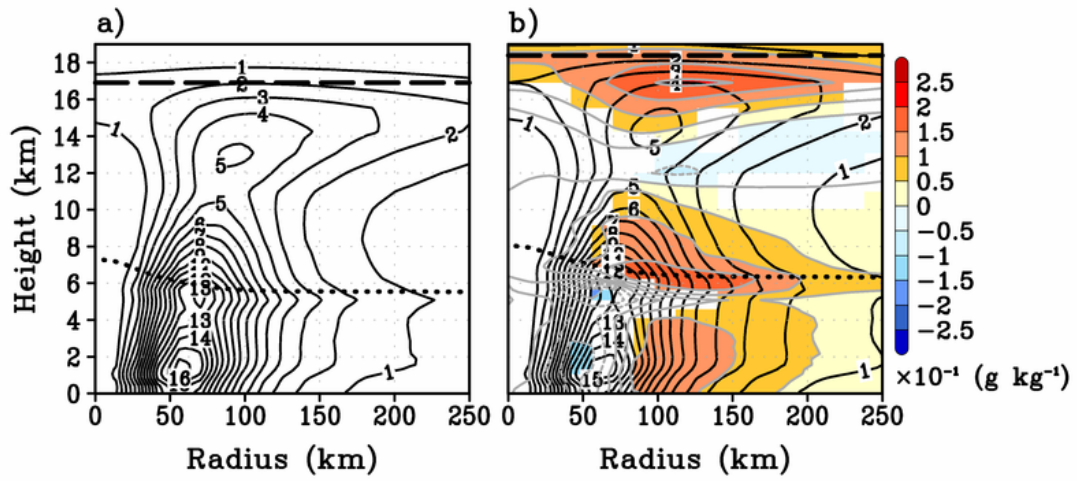

Fig. 5.19. Composites of azimuthal mean water contents (g kg^{-1}) of C4 TCs at their lifetime minimum SLP obtained in the PD and GW simulations. The thin black lines are the radius-height cross-sections of the water contents (g kg^{-1}). Panels a) and b) show the PD and GW simulations, respectively. The gray lines depict the differences between GW and PD simulations [shaded areas show where the differences are statistically significant at the 90% confidence level (two-sided Welch's *t*-test)]. The contour intervals of the black and gray lines are 1×10^{-1} (g kg^{-1}). The thick dashed line indicates the tropopause height, and the thick dotted line represents the melting level.

Under warmer climate conditions, the diabatic heating increases in the upper

edges of convective clouds. This increase becomes evident at radii exceeding 50–150 km, and its maximum is observed at a radius of 80 km (Fig. 5.20b). This radius corresponds to the RPS (Fig. 5.18b). Thus, we speculate that an increase in diabatic heating contributes to a decrease of pressure.

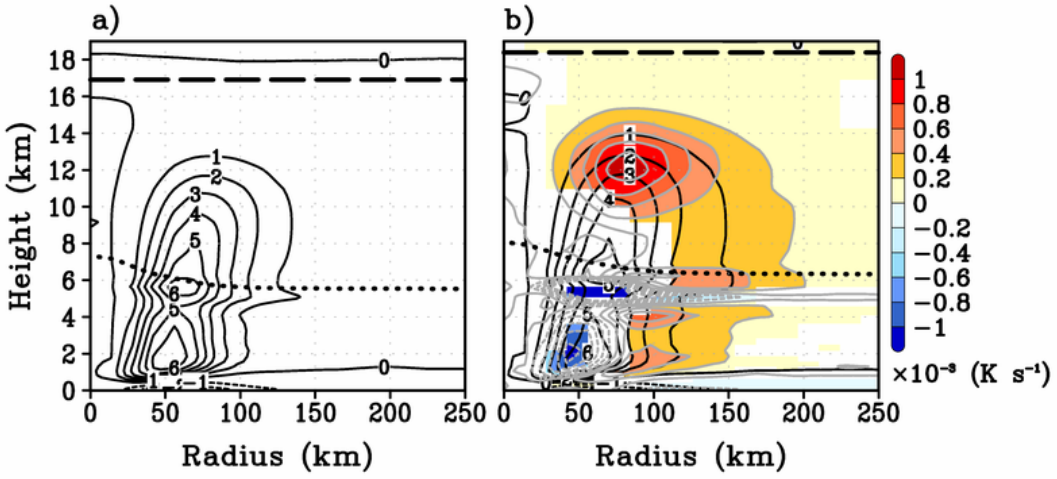

Fig. 5.20. Similar to Fig. 5.19 except for diabatic heating (K s^{-1}). The contour intervals of the black and gray lines are 1×10^{-3} (K s^{-1}).

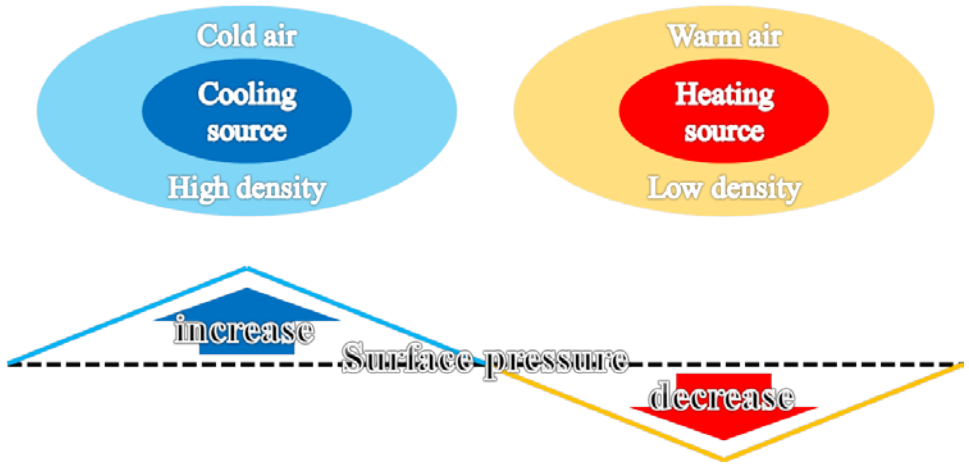

Fig. 5.21. Schematic of hydrostatic adjustment.

Previous studies (Smith 1981; Wang 2009) suggested a relationship between the heating of an atmospheric column and the surface pressure underneath the column (i.e., hydrostatic adjustment). Hydrostatic adjustment means that an atmosphere is

heated or cooled by a heating source, and the density of the heated or cooled air decreases or increases, respectively. Thus, the heating (cooling) of an atmospheric column decreases (increases) the surface pressure underneath the column (Fig. 5.21).

For instance, Wang (2009) evaluated the effects of phase change-induced diabatic heating on TC structure and intensity by artificially modifying the heating and cooling rate due to cloud processes in the model. The results revealed that the heating (cooling) of outer spiral rainbands decreases (increases) the surface pressure underneath those rainbands, affecting TC structure and intensity.

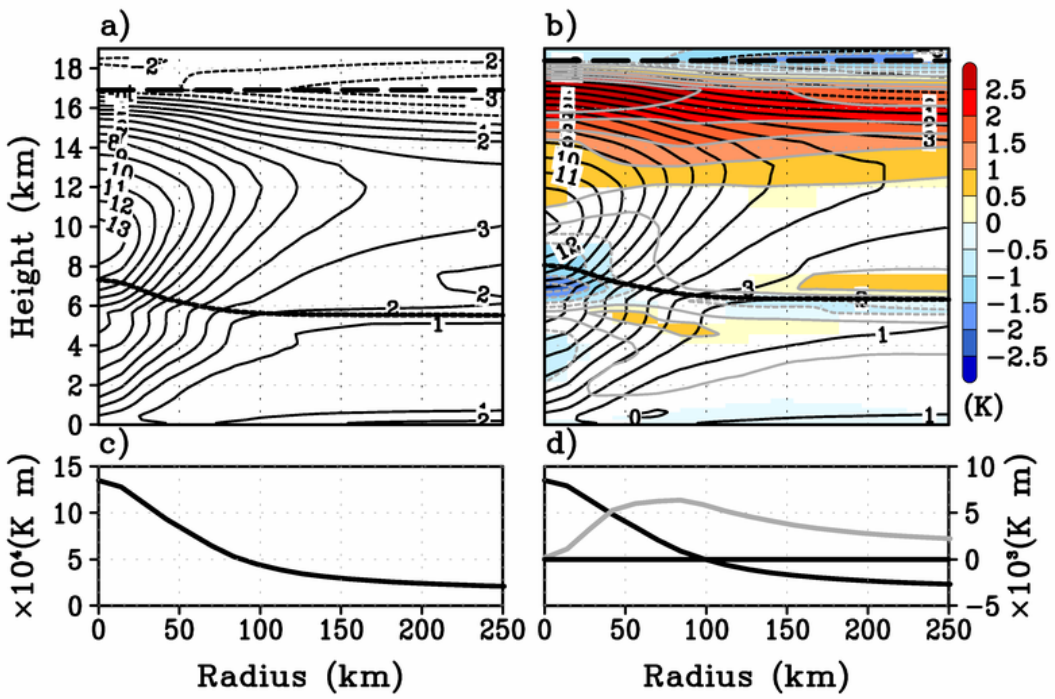

Fig. 5.22. The figure is similar to Fig. 5.19, except for the temperature anomaly (K). The contour intervals of the black and gray lines are 1 K s^{-1}. The temperature anomaly is defined relative to the mean temperature outside of 1500 km. Bottom panels show column-integrated temperature anomaly from the surface to tropopause height (thin dashed line) in the present-day (PD; c) and global warming (GW; d) simulations. The gray line in panel *d* indicates the difference between the PD and GW simulations.

Herein, increases in diabatic heating within the eyewall seem to play a similar

role as the outer rainbands in Wang (2009). To confirm the effect of hydrostatic adjustment in the present study, Fig. 5.22 shows the radius-height cross-sections of temperature anomalies (K) relative to the mean temperature outside of 1500 km. The change in the temperature anomaly (Fig. 5.22b) near the center of the TC exhibits cooling around the melting level and warming in the upper troposphere, suggesting the elevation of the warm core. The temperature anomalies increase in the outer edge of the eyewall (radii exceeding 50–150 km above the melting level). Comparing Fig. 5.22 with 5.20, we speculate that these increases are associated with the increases in diabatic heating due to convective clouds. The increases in temperature anomaly decreases pressure underneath the outer edge of the eyewall.

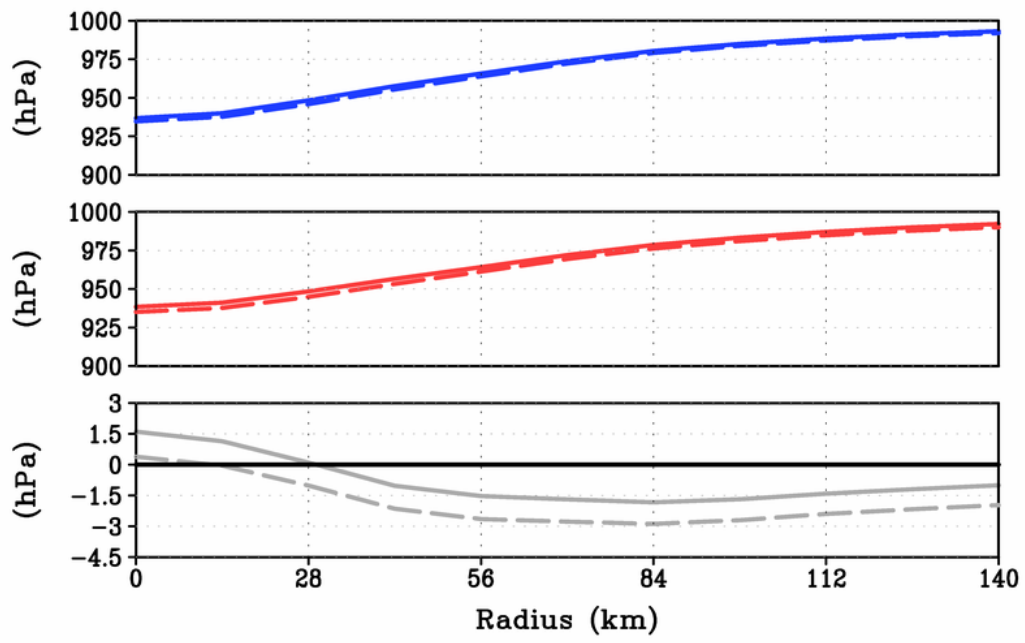

Fig. 5.23. Composite radial profiles of the column-integrated product of density and gravitational acceleration (solid lines) and SLP (dashed lines) for C4 TCs. Top, middle, and bottom panels show results of the PD and GW simulations and the differences between them, respectively.

Figure 5.23 shows comparisons between SLP and the column-integrated dry air mass from surface to the model top (38 km). The column integral is consistent with SLP

despite ignoring the effect of moisture. The differences in both plots between the PD and GW have similar radial profiles, and positions of the maximum decreases correspond to a radius of 84 km. At this radius, the column integral contributes more than 50% to the change in SLP. Thus, hydrostatic adjustment plays a key role in the responses of the radial profile of tangential wind to global warming (Fig. 5.13).

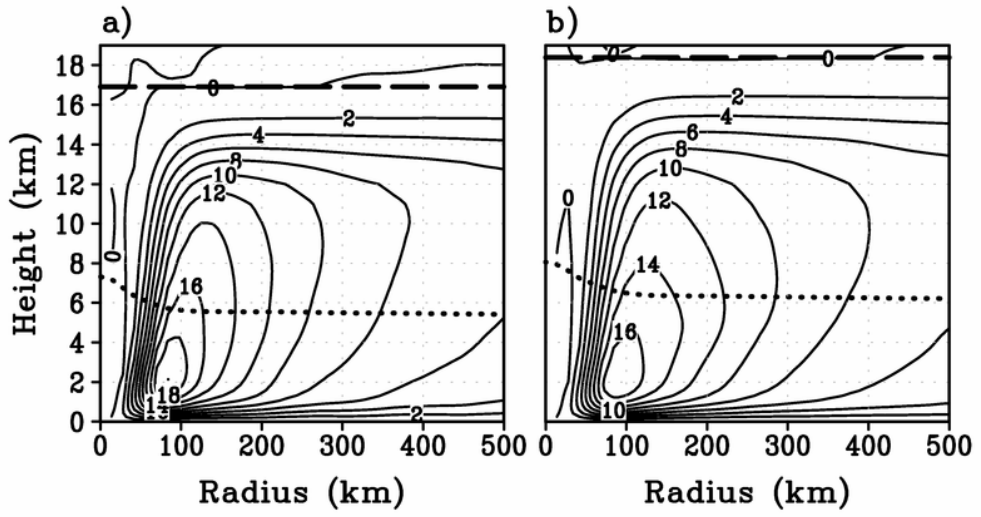

Fig. 5.24. Composites of mass-weighted stream function (kg s^{-1}) of C4 TCs at their lifetime minimum SLP obtained in the present-day (PD) and global warming (GW) simulations. The thin black lines are the radius-height cross-sections of the water contents. Panels a) and b) show the PD and GW simulations, respectively. The contour intervals of the black line are 1×10^3 kg s^{-1}. The thick dashed line indicates the tropopause height, and the thick dotted line represents the melting level.

Using the Sawyer–Eliassen model, Shapiro and Willoughby (1982) showed that heating affects spatial distribution of secondary circulation. To examine the effects of increases in diabatic heating on secondary circulation in the NICAM simulation, Fig. 5.24 depicts the mass-weighted stream function. As TCs become taller under warmer climates, the secondary circulation extends in the vertical and radial directions. For instance, the contour lines at 8 km reach a radius of 400 km in the GW

but not in the PD. Since secondary circulation is widened, the TCs in GW transport angular momentum from a greater distance to their center compared to in PD.

The absolute angular momentums in PD and GW are shown in Fig. 5.25. Under the warmer condition, the absolute angular momentums increase above the melting layer. Increases above the melting layer appear to be related to changes in the warm core and the elevation of tropopause height. As depicted in Fig. 5.22, the isothermals widen in the radial direction above the melting level, and the radial gradient of temperature decreases. To satisfy the thermal wind balance, the vertical gradient of tangential wind is decreased by the reduction in the radial gradient of temperature. Thus, the absolute angular momentum in the GW is larger than those in the PD at higher altitude. A dipole structure is observed below the melting level, and the absolute angular momentum increases outside eyewall region and decreases inside it. This dipole structure is linked to the future change in pressure gradient due to the rise of the eyewall.

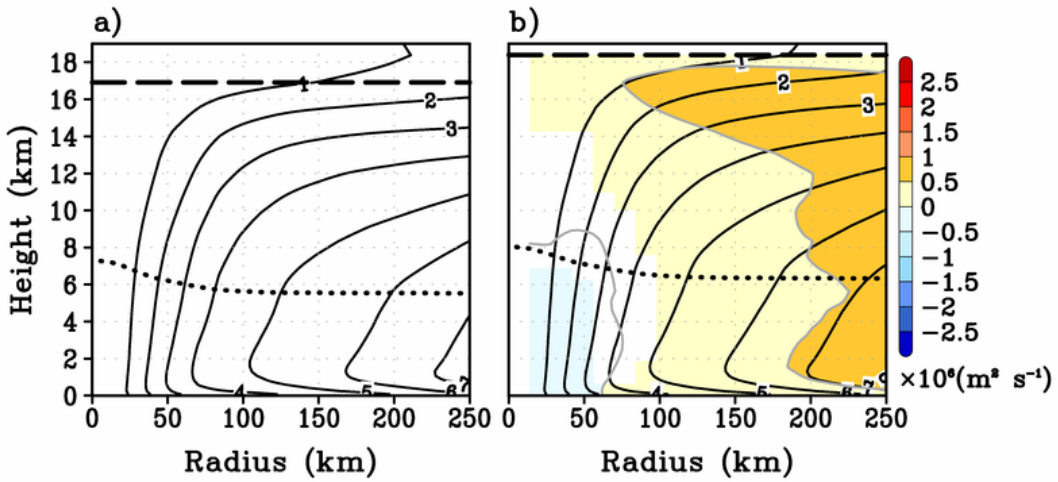

Fig. 5.25. Similar to Fig. 5.19 except for absolute angular momentum (m^2 s^{-1}). The contour intervals of the black and gray lines are 1×10^6 m^2 s^{-1}.

Within the boundary layer, Fig. 5.24 depicts a weakening of inflow at a radius of 84 km. This weakening results from the future changes in pressure gradient. In the

inner edge of the eyewall, the pressure gradient is reduced under the warmer condition (Fig. 5.15). Thus, surface inflows in the GW do not reach to more inward than those in the PD (Fig. 5.26). In the upper troposphere, Fig. 5.26 shows a significant decrease in radial velocity and a significant increase above the decrease. This change is associated with the upward shit of outflow due to the increase in tropopause height.

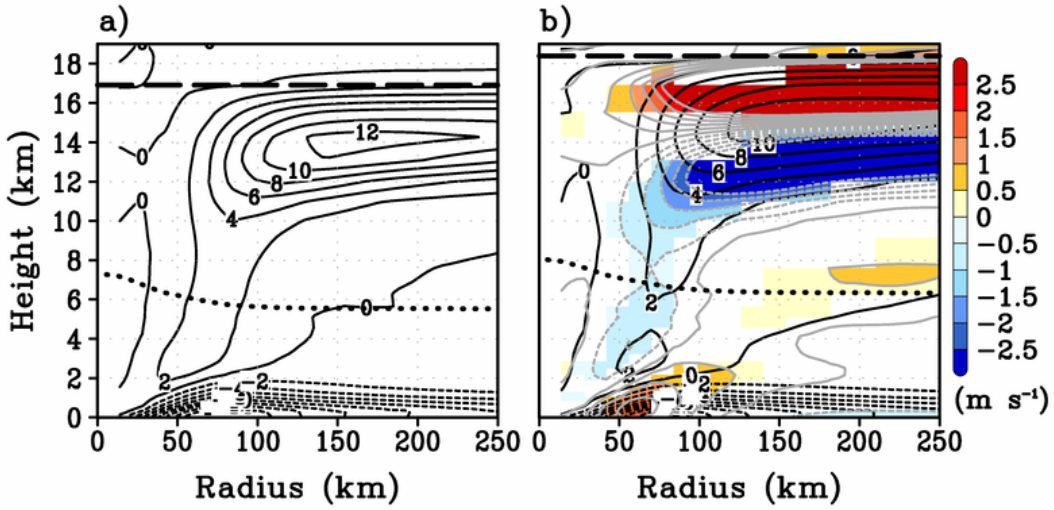

Fig. 5.26. Similar to Fig. 5.19 except for radial velocity (m s^{-1}). The contour intervals of the black and gray lines are 5 m s^{-1}.

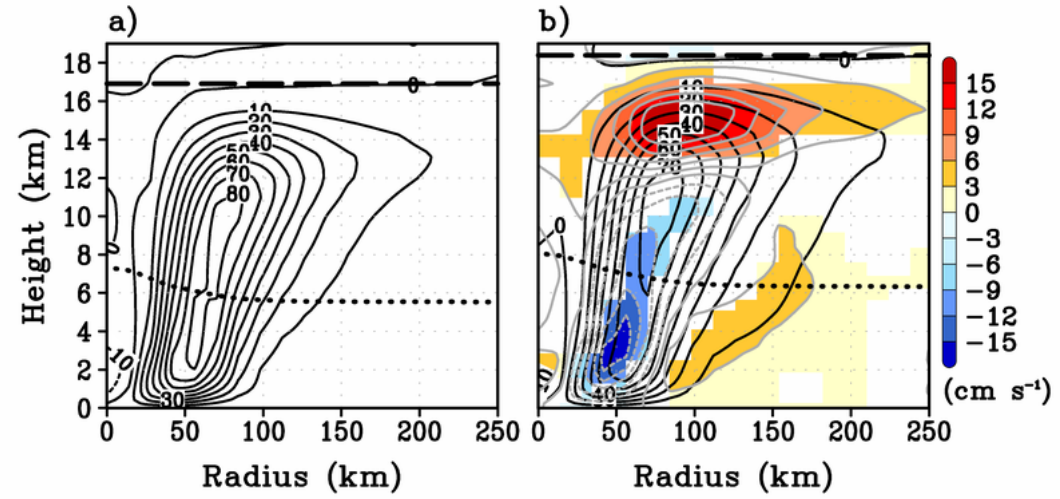

Fig. 5.27. Similar to Fig. 5.19 except for vertical velocity (cm s^{-1}). The contour intervals of the black and gray lines are 10 cm s^{-1}.

Figure 5.27 shows the radius-height cross-sections of vertical velocity. As seen in Fig. 5.26, the low-level convergence is weakened by a reduction in the pressure gradient in the inner edge of the eyewall. Updrafts seem to become weaker under warmer conditions. However, the updrafts shift outward because of the weakening of the low-level convergence. Thus, the updraft area within the eyewall is widened, and the upward mass flux within TCs in the GW is larger than that in the PD. This finding was discussed in Satoh et al. (2015).

The size of RMW varies from TC to TC (Weatherford and Gray 1988; Kimball and Mulekar 2004). To examine future changes in the degree of variation, Fig. 5.28 shows the probability density functions of TC frequency as function of RMW at a height of 1.5 km for each intensity category. Using NICAM with 14-km mesh, the GW simulation predicts that more of the TCs developing less than 980 hPa will form large maximum wind radii than in the PD simulation.

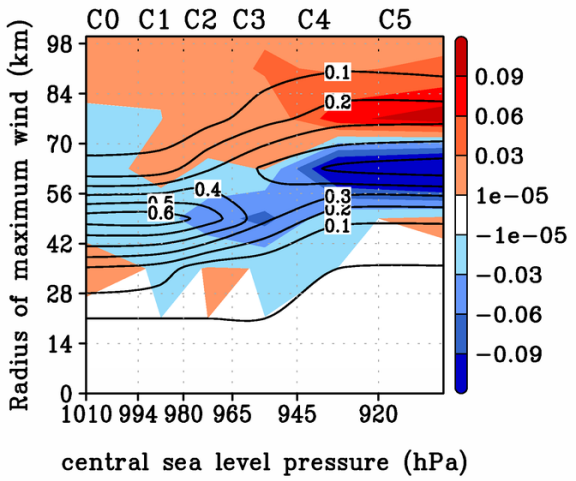

Fig. 5.28. Probability density functions of TC frequency as a function of RMW (km) at a height of 1.5 km for each intensity category. Simulated TCs are tabulated in classes of 14 km (vertical axes) and intensity category (C0–5; horizontal axes). The black lines show the probability density functions for the each category. The color indicates the difference in frequencies between the GW and PD simulations.

Table 5.2 lists the mean and median radii for each intensity category under both climate conditions calculated from the samples in Fig. 5.28. The mean and median RMW increase with deepening central SLP, with the exception of the mean radius in C5 TCs. Kimball and Mulekar (2004) documented the relationship between RMW and TC intensity using the observed dataset for the Atlantic. They showed that the size of median radius decreases from 55.5 to 27.8 km as the TCs become more intense. This result (Fig. 5.28) does not agree with the conclusions of Kimball and Mulekar (2004), and the RMW simulated in NICAM is larger than the observed RMW. Thus, that 14-km grid interval appears to be insufficient to completely resolve the RMW.

Table 5.2. Mean and median RMW (km) for each intensity category (C0–5) for the present-day simulation (PD) and global warming simulation (GW).

	C0	C1	C2	C3	C4	C5
PD [mean]	42.5	44.4	51.8	57.5	61.3	58.9
PD [median]	42.0	42.0	42.0	56.0	56.0	56.0
GW [mean]	40.5	46.2	53.7	61.8	66.8	62.9
GW [median]	42.0	42.0	42.0	56.0	70.0	70.0

The mean RMWs become larger under warmer climate, with the exception of C0 TCs. Changes in RMW size are not statistically significant, and the RMW predicted by 14-km NICAM is larger than the observed value. However, we found that the response of tangential velocity to increases in diabatic heating due to the rise of the eyewall is statistically significant (Figs. 5.13b and c); tangential velocity increases outside the eyewall. This increase seems to widen a gale wind radius of TC, which is defined as the azimuthally-averaged radius of 15 m s^{-1} (R15) in the present study. Figure

5.29 is the probability density functions of TC frequency as function of R15 at a height of 10 m for each intensity category. The GW simulation shows that more of the TCs will form large R15 than in the PD simulation.

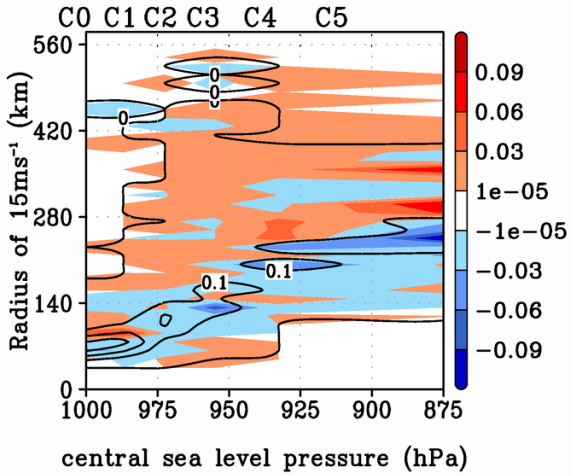

Fig. 5.29. Similar to Fig. 5.28 except for R15 (km).

The increase in tangential velocity outside the eyewall seems to be sensitive to the degree of the eyewall slope. The eyewall slope should determine a spatial distribution of diabatic heating. In Chapters 6 and 7, we discuss the sensitivity of eyewall slope to the horizontal grid spacing using the outputs of the 7-km NICAM simulation and the effect of eyewall slope on the distribution of tangential velocity using the Sawyer–Eliassen model (Pendergrass and Willoughby 2009).

Chapter 6 Dependency on Horizontal Resolution

Previous studies using RCM documented that the eyewall slope does not converge in a horizontal grid spacing of <10 km (Fierro et al. 2009; Gentry and Lackmann 2010; Sun et al. 2013). Based on the results of these studies, the size of RMW will become smaller and the eyewall slope will become more upright as the horizontal grid spacing becomes finer. In this chapter, we determined if NICAM simulations could reproduce the relationship between the size of the RMW and the eyewall slope by applying horizontal grid intervals of 7 and 14 km. In the previous chapters, the 14-km simulation was described; however, in this chapter, the present-day and warmer simulations in the 7-km simulation were investigated and are abbreviated as PD07 and GW07, respectively.

6.1 Model settings and experimental design

The model settings of the sensitivity simulation were exactly same as the PD and GW simulations (Table 2.2) except for the horizontal grid spacing, which was 7 km in this sensitivity experiment. The physical processes in this experiment were previously described in Chapter 2.2. The SST in PD07 was nudged toward a weekly interpolated National and Atmospheric Administration (NOAA)-Optimum Interpolated (OI) SST (Reynolds et al. 2002). Future changes were processed in the same manner as the GW simulations.

Unlike the 14-km simulation, the 7-km simulation was not conducted for more than 30 years because of a restriction of computational resources. The 7-km simulation

followed a time-slice method (Bengtsson et al. 1996); moreover, all of the simulations in the PD07 simulation were conducted from 1 June to 31 October for the following years: 1994, 1997, 1998, 1999, 2005, 2011, 2012, 2013, and 2014. The simulation for 2004 was extended from 1 Jun 2004 to 31 May 2005. Figure 6.1 shows a schematic of the simulation period for all the PD07 simulations. The GW07 simulations started on 1 May for the same years as PD07. The first month in the GW07 simulation was regarded as the spin-up period. As the ERA-40 dataset did not include data after 2002, the initial atmospheric conditions in both simulations were taken from the JRA-55 dataset (Ebita et al. 2011).

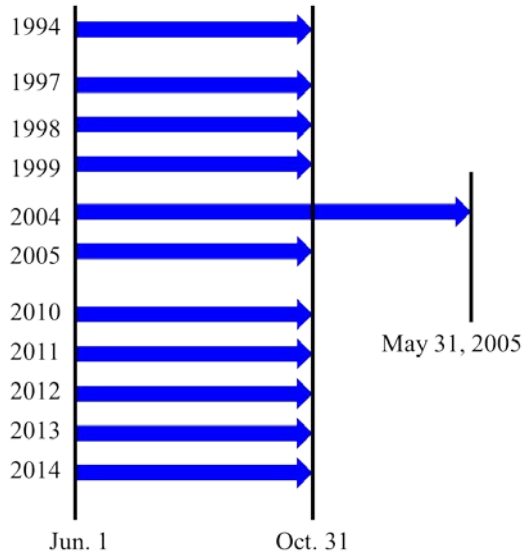

Fig. 6.1. Schematic of the simulation periods for all of the PD07 simulations.

The criterion of the relative vorticity for the tracking method was 1.55×10^{-3} s^{-1}. This value was optimized to match the number of annual global mean TCs in the present-day simulations for 2004 with the observed number. The other parameters were exactly the same as the 14-km simulation.

6.2 Results

Table 6.1 lists the TC frequencies for each intensity category. The TCs were categorized using the same manner as that listed in Table 4.2. The GW07 simulation predicted a 26.4% reduction in the total TC frequency relative to the PD07 simulation, as well as an increase in the rate of intense TCs (C4–C5) to total TCs from 15.5% to 18.8%. These findings were consistent with previous studies (Knutson et al. 2010; IPCC 2013) and the 14-km simulation.

Table 6.1. TC frequencies categorized by the lifetime minimum central SLP (Pc). Results are presented for the PD07 and GW07 simulations.

Category	Central pressure (hPa)	PD (Num.)	GW (Num.)
C5	Pc ＜ 920	11	12
C4	920 ≦ Pc ＜ 945	64	55
C3	945 ≦ Pc ＜ 965	145	86
C2	965 ≦ Pc ＜ 980	115	71
C1	980 ≦ Pc ＜ 994	104	79
C0	994 ≦ Pc	46	54
C6 (C2–C4)	920 ≦ Pc ＜ 980	324	213
Total		485	357

We compared the size of the RMW between the 14- and 7-km simulations (Tables 5.2 and 6.2). In the 7-km simulation, the mean and median sizes of the RMW decreased for each intensity category relative to the 14-km simulation; moreover, they

were close to previously observed values (Kimball and Mulekar 2004). These results were consistent with the previous studies using the RCM. The 7-km simulation appeared to improve the ability to simulate the RMW. Thus, the observed relationship between the minimum SLP and the maximum wind speed was close to the empirical relationship described in Atkinson and Holiday (1977). This improvement is shown in Fig. 6.2.

Table 6.2. Lists of the mean and median RMW (km) for the each intensity category (C0–C5) for the present-day simulation (PD) and global warming simulation (GW), respectively.

	C0	C1	C2	C3	C4	C5
PD [mean]	34.8	31.0	38.2	42.6	44.3	44.5
PD [median]	28.0	28.0	35.0	35.0	42.0	35.0
GW [mean]	33.8	28.9	36.3	40.0	41.0	40.3
GW [median]	28.0	28.0	35.0	35.0	42.0	35.0

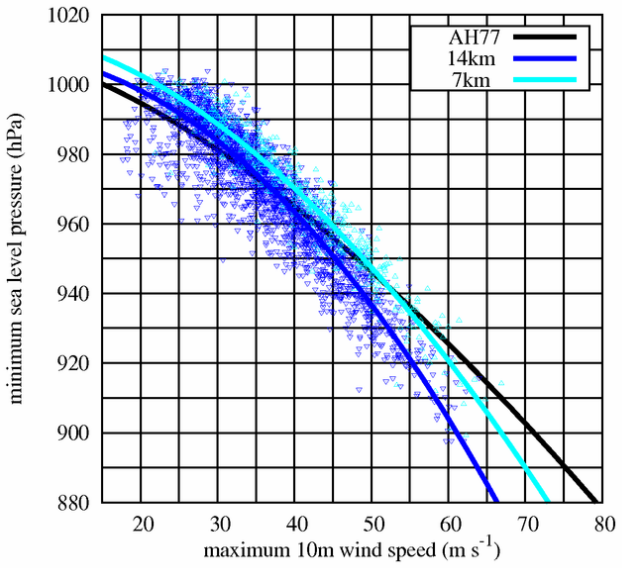

Fig. 6.2. As in Fig. 3.7 except for superimposed the result on 7-km simulation.

The 14- and 7-km simulations displayed opposite responses to the size of the RMW to global warming, indicating that we could not conclude future change in the RMW obtained by analyzing the 14-km simulation. The discrepancy might be caused form a fact that the number of TCs in the 7-km simulation was less than 20% relative to that in the 14-km simulation.

The eyewall slope can be determined by the RMW, updrafts, absolute angular momentum, or 20-dBZ reflectivity isosurface (Stern and Nolan, 2009; Hazelton and Hart, 2013; Stern et al., 2014). In this study, the eyewall slope was estimated by the RMW. Figure 6.3 shows the procedure that was used to calculate the eyewall slope. First, we detected the RMW at each altitude between heights of 2 and 11 km. Then, the best-fit line was calculated by the least-squares method. Finally, we defined the slope of eyewall as θ°, which was the angle between the best-fit line and the horizontal line.

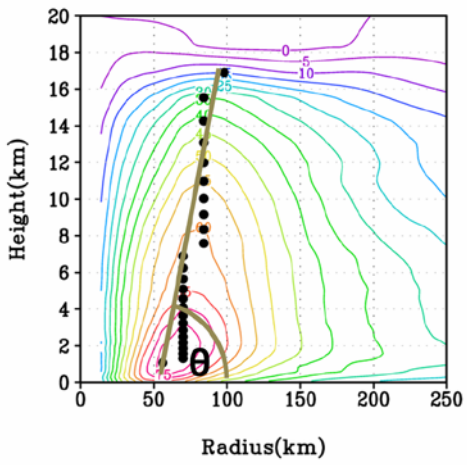

Fig. 6.3. Definition of the eyewall slope (θ°). Circles indicate the RMW at each altitude. The gray line is the best fit line passing those circles, which was calculated using the least-squares method.

Figure 6.4 shows the eyewall slope for the each intensity category in the PD, GW, PD07, and GW07 simulations. The relationship between the size of the RMW and eyewall slope was consistent with the results of Stern and Nolan (2009). The eyewall

slope (θ°) became smaller as the size of the RMW became larger. The GW and GW07 simulations predicted that the eyewall slope will become slightly more upright, although these changes were not statistically significant because of large fluctuation.

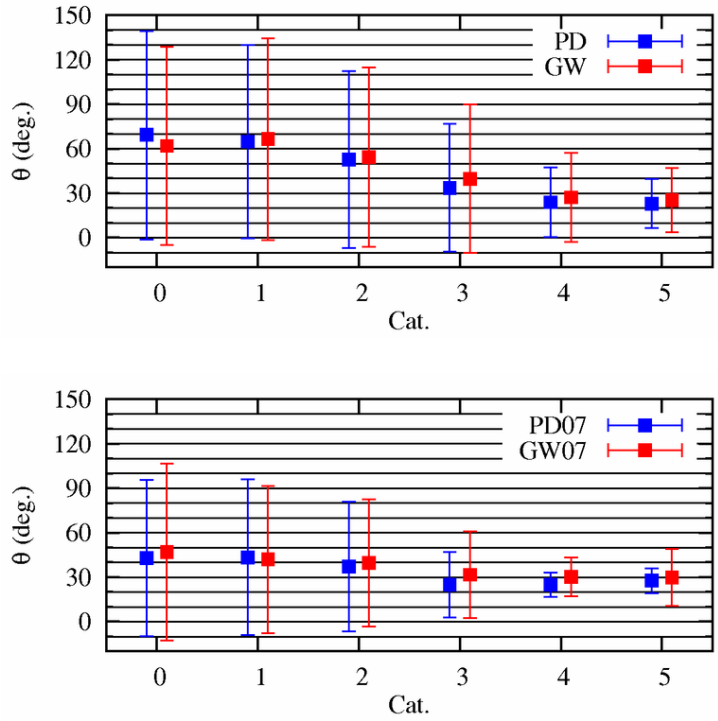

Fig. 6.4. Comparison of the eyewall slopes for the 14- and 7-km simulations calculated by the method described in Fig. 6.3 for the each intensity category. The upper and lower panels show the results from the 14- and 7-km simulations, respectively. The blue and red boxes with standard deviations indicate the present-day and global warming simulations, respectively.

Next, we examined if the effect of diabatic heating on the radial distribution of tangential velocity in the 7-km simulation was the same as the effect observed for the 14-km simulation described in Chapter 5.3. The number of TCs produced in the 7-km simulation was fewer than that in the 14-km simulation. In the 14-km simulation, TCs categorized as C2–C5 showed the same response of the radial profiles of tangential velocity. Because the C5 TCs did not include the upper limit of intensity, they were excluded in this analysis. In this chapter, we considered the composite mean for C2–C4,

which is referred to as C6; moreover, the size of the RMW had a large variation. We normalized the horizontal scale of diabatic heating by the size of the RMW.

Figure 6.5 shows the radial-height cross-sections of the composite of azimuthal mean diabatic heating. Under warmer climate conditions, the 7-km simulation predicted a rise of diabatic heating which is produced by the convective cloud, and the diabatic heating increased within the convective cloud region. This increase was obvious in the upper edge of the convective cloud, and its maximum was located around the normalized radius of 1.5 at a height of 12 km.

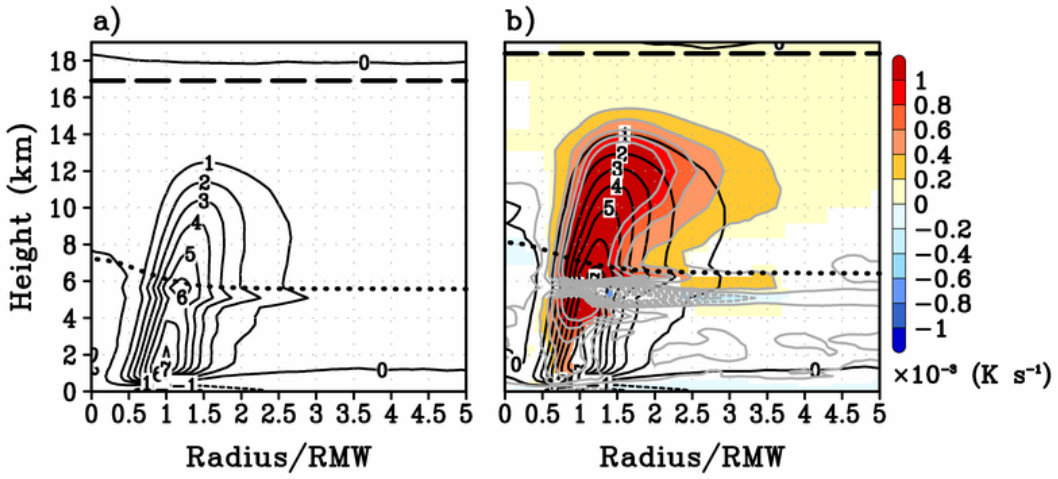

Fig. 6.5. Composites of azimuthal mean diabatic heating (K s^{-1}) of C6 TCs at their lifetime minimum SLP, obtained in the PD07 and GW07 simulations. The horizontal scale was normalized by the size of the RMW at a height of 1.5 km. The thin black lines represent the radius–height cross-sections of diabatic heating (K s^{-1}). Panels a) and b) show the PD07 and GW07 simulations, respectively. The gray lines depict the differences between the GW and PD simulations [shaded areas show where the differences are statistically significant at the 90% confidence level (two-sided Welch's *t*-test)]. The contour intervals of the black and gray lines are 1×10^{-3} (K s^{-1}). The thick dashed line indicates the tropopause height, and the thick dotted line represents the melting level.

The responses of the pressure and 10 m tangential velocity (V_{T10}) to increases in diabatic heating are shown in Fig. 6.6; however, this analysis employed a wider

intensity range (C2–C4) than that used in the 14-km simulation (C4) and the variation of intensity was larger. Thus, we displayed the normalized pressure anomaly (Pa) by Pa at the center of the TCs, and normalized V_{T10} by the absolute value of the maximum V_{T10}. Note that Pa was defined relative to the mean pressure outside of 1500 km.

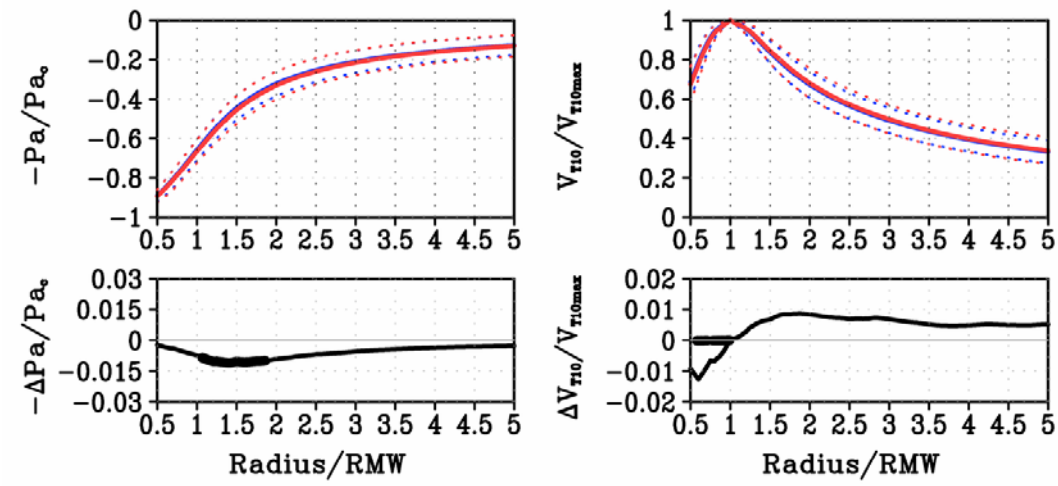

Fig. 6.6. Composites of normalized pressure anomalies at sea level relative to the mean pressure outside of 1500 km (Pa; left-side panels) and of normalized tangential velocity at a height of 10 m (V_{T10}; right-side panel) for C6 TCs. The horizontal scale was normalized by the size of the RMW at a height of 10 m. The Pa and V_{T10} values were normalized by Pa at the center of the TC and by the absolute value of the maximum V_{T10}, respectively. The upper panel shows the radial profile of the Pa of each variable in the PD07 simulation (blue line) and GW07 simulation (red line) with the standard deviation (dotted lines). The bottom panel shows the difference in each variable between the GW07 and PD07 simulations. The circles indicate a significant change at the 90% confidence level (two-sided Welch's *t*-test; Welch 1947).

Under warmer climates, Pa was observed to decrease between 1 and 2 normalized radii at a statistically significant at the 90% confidence level (two-sided Welch's *t*-test). The V_{T10} values increased outside the RMW, though the changes in V_{T10} were not statistically significant since variances of V_{T10} were larger than those of Pa. The 7-km simulation supported the response of SLP and V_{T10} to an increase in diabatic heating, as seen in the 14-km simulation.

Chapter 7 General Discussion

7.1 Characterization of the eyewall slope

In this study, there was an increase in tangential velocity outside the outer edge of the eyewall because of the air warmed by an increase in diabatic heating in the upper edge of convective clouds because of a rise of tropopause height under warmer climate conditions; moreover, this mechanism follows hydrostatic adjustment (Smith 1981; Wang 2009). In this mechanism, the model should reproduce the locus of an increase in diabetic heating, which is linked to the eyewall slope.

Previous studies using RCMs indicated that the eyewall slope varies even though RCMs employ horizontal grid spacing smaller than a few kilometers (Fierro et al. 2009; Gentry et al. 2010; Sun et al. 2013). Therefore, the 7- and 14-km models may not have completely reproduced the eyewall slope in the current study. Hazelton and Hart (2013) observed that the mean slope of the eyewall is 31.5° (±5°) from horizontal, which is consistent with the C4 TCs in the 14-km simulation (Fig. 6.4 upper panel). However, the eyewall slope reported by Hazelton and Hart (2013) was calculated from 124 flight legs obtained from 15 TCs over the Atlantic Ocean. Their result included all the stages between lifecycles of 15 TCs, which developed into different intensities. Therefore, the relationship between the hydrostatic adjustment and the eyewall slope should be tested.

The artificial adjustment of the eyewall slope is difficult to achieve in the simulated models. The Sawyer–Eliassen model diagnoses the effect of heating and momentum sources on the secondary circulation of a balanced vortex (Shapiro and

Willoughby, 1982). A change in secondary circulation coincides with that in pressure and tangential velocity (primary circulation). Shapiro and Willoughby (1982) revealed that the responses of pressure and primary circulation alter by displacing the locus of the heating source. The displacement of the heating source in the Sawyer–Eliassen model is expected to result in an increase in diabatic heating in the upper edge of the eyewall due to global warming, as seen in Chapter 5.3. In this method, we can artificially adjust the eyewall slope. Thus, this method can analytically estimate the sensitivity of future changes in pressure and tangential velocity to a locus of heating.

In this study, we employed the Sawyer–Eliassen model in height coordinates, as described by Pendergrass and Willoughby (2009). Note that the definitions of each symbol in this subchapter are listed in Table 7.1.

Table 7.1. Description of symbols used in the Sawyer–Eliassen model (Eqs. 7.1–7.5).

Symbol	Description	Unit
$b = g \ln\left(\frac{\theta}{273.16}\right)$	Buoyancy	(m s^{-2})
c_p	The specific heat at constant pressure for dry air	(m^2 s^{-2} K^{-1})
f	Coriolis parameter	(s^{-1})
g	Gravitational acceleration	(m s^{-2})
p	Pressure	(Pa)
q	Heating rate	(m^2 s^{-3})
r	Radius	(m)
t	Time	(s)
u	Radial velocity	(m s^{-1})
v	Tangential velocity	(m s^{-1})
w	Vertical velocity	(m s^{-1})
z	Height	(m)
$B = \frac{\partial b}{\partial r}$	Radial gradient of buoyancy	(s^{-2})
M	Surface friction	(m s^{-2})

Table 7.1. (*Continued*)

Symbol	Description	Unit
$N^2 = \frac{\partial b}{\partial z}$	Vertical gradient of buoyancy	(s^{-2})
$Q = \frac{gq}{c_p \theta}$	Diabatic buoyancy source	(m s^{-3})
R	The gas constant for dry air	(m^2 s^{-2} K^{-1})
$S = \frac{\partial v}{\partial z}$	Vertical gradient of tangential velocity	(s^{-1})
$\zeta = \frac{\partial v}{\partial r} + \frac{v}{r} + f$	Vorticity	(s^{-1})
θ	Potential temperature	(K)
$\pi = \left(\frac{p}{1000}\right)^{\frac{R}{c_p}}$	Exner function	Dimensionless
ρ	Density	(kg m^{-3})
Ψ	Mass stream function	(kg s^{-1})

Pendergrass and Willoughby (2009) derived a form of the Sawyer–Eliassen model in height coordinates from equations of tangential momentum (Eq. 7.1), thermodynamic energy (Eq. 7.2), radial momentum (Eq. 7.3), and vertical momentum (Eq. 7.4):

$$\frac{\partial v}{\partial t} + \varsigma u + Sw = M\,, \tag{7.1}$$

$$\frac{\partial b}{\partial t} + Bu + N^2 w = Q\,, \tag{7.2}$$

$$\frac{v^2}{r} + fv = c_p \theta \frac{\partial \pi}{\partial r}\,, \tag{7.3}$$

and

$$\frac{\partial \pi}{\partial z} = -\frac{g}{c_p \theta}\,. \tag{7.4}$$

The Sawyer–Eliassen model is written as follows:

$$
\begin{aligned}
&N^2\frac{\partial^2\psi}{\partial r^2}-2B\frac{\partial^2\psi}{\partial z\partial r}+I^2\frac{\partial^2\psi}{\partial z^2}\\
&-\left(\frac{N^2}{R_\rho}-\frac{B}{H_\rho}+N^2\frac{\partial\gamma}{\partial z}\right)\frac{\partial\psi}{\partial r}\\
&-\left(\frac{I^2}{H_\rho}-\frac{B}{R_\rho}-\frac{3\xi S}{r}-N^2\frac{\partial\gamma}{\partial r}\right)\frac{\partial\psi}{\partial r}\\
&=r\rho\left[\frac{\partial Q}{\partial r}-\frac{\partial}{\partial z}(\xi M)+\gamma\frac{\partial Q}{\partial z}\right]
\end{aligned}
\qquad \text{(Eq. 7.5)}
$$

where $\gamma=\frac{1}{g}\left(\frac{v^2}{r}+fv\right)$, $\xi=\frac{2v}{r}+f$, $H_\rho^{-1}=\rho^{-1}\frac{\partial\rho}{\partial z}$, $R_\rho^{-1}=r^{-1}+\rho^{-1}\frac{\partial\rho}{\partial r}$, and $I^2=\varsigma\xi-\gamma B$, respectively. To focus on the heating source, we neglected the effect of surface friction (*M* in Eqs. 7.1 and 7.5). By solving Eq. 7.5 for a vortex satisfying thermal wind balance with a heating source, the mass stream function is obtained. Then, tangential and vertical velocities were calculated from the mass stream function:

$$u=-\frac{1}{r\rho}\frac{\partial\psi}{\partial z}, \qquad (7.6)$$

and

$$w=\frac{1}{r\rho}\frac{\partial\psi}{\partial r}, \qquad (7.7)$$

where the tendency of vertical velocity was calculated from Eq. 7.1.

The balanced vortex satisfies thermal wind balance with a sectionally continuous tangential wind profile (Willoughby et al. 2006). Its primary circulations are formulated by the following equations:

$$V_i=V_{\max}(z)\left[\frac{r}{R_{\max}(z)}\right]^n, \quad 0\le r\le R_1(z), \qquad (7.8)$$

$$V_o=V_{\max}(z)\exp\left[\frac{r-R_{\max}(z)}{D_e}\right], \qquad R_2(z)\le r, \qquad (7.9)$$

where V_i and V_o are the tangential wind profiles inside and outside the eye, respectively; $V_{max}(z)$ and $R_{max}(z)$ are the maximum wind speed and the RMW; and D_e is the e-folding distance. The parameter n was defined as 1.5, and D_e was defined as 300 km. These two segments were smoothly connected via a transition zone between $R_1(z)$ and $R_2(z)$:

$$V_{Trans} = V_i[1 - A(x)] + V_o A(x), \qquad R_1(z) \le r \le R_2(z). \tag{7.10}$$

where $x = \dfrac{r - R_1(z)}{R_1(z) - R_2(z)}$. The $A(x)$ term is a polynomial weighting function, which is also referred to as a ramp function (Willoughby et al. 2006). Ramp functions are formulated as follows:

$$A_1(x) = x^2(3 - 2x), \tag{7.11}$$

$$A_2(x) = x^3[10 - x(15 - 6x)], \tag{7.12}$$

$$A_3(x) = x^4\{35 - x[84 - x(70 - 20x)]\}, \tag{7.13}$$

$$A_4(x) = x^5\langle 126 - x\{420 - x[540 - x(315 - 70x)]\}\rangle. \tag{7.14}$$

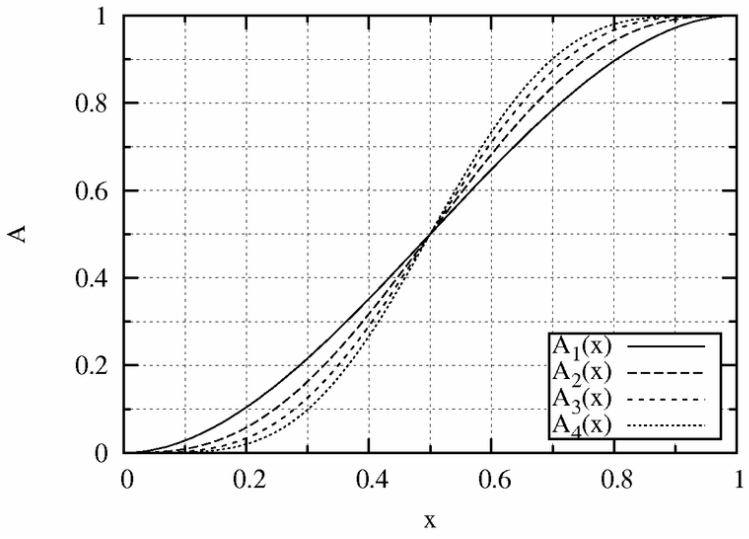

Fig. 7.1. Polynomial ramp functions computed from Eqs. 7.11–7.14.

For $0 \le x \le 1$, each function varied from 0 to 1 as seen in Fig. 7.1. The *A(x)* term was defined as 0 for $x \le 0$, and 1 for $1 \le x$, respectively. Following Pendergrass and

Willoughby (2009), Eq. 7.12 was employed as a weighting function for determining the radial profile of tangential wind of the balanced vortex.

For a vortex satisfying thermal wind balance, the tangential wind decreases as the altitude becomes higher. Using Eq. 7.12, the vertical profile of the maximum wind was specified as follows:

$$V_{max}(z) = V_{maxb} A_2(y), \tag{7.15}$$

where V_{maxb} is the maximum wind at the bottom level in the model, and $y(z) = \dfrac{z_{top} - z}{z_{top}}$.

The mass and thermodynamic fields were iteratively calculated from the gradient balance (Eq 7.3) and the hydrostatic balance (Eq. 7.4) for the balanced vortex (Pendergrass and Willoughby 2009). As the lapse rate was 6.67 K km^{-1}, the environmental temperature profile was defined as 300 − 6.67 × 10^{-3}z K below the tropopause, and a constant value of 200 K above.

Based on Ohno and Satoh (2015), the diabatic buoyancy sources imposed on the balanced vortex were characterized as the following functions:

$$Q_H(r,z) = Q_0 \left[r_q (1 - r_q) \right]^3 A_2(y_q), \tag{7.16}$$

$$Q_L(r,z) = Q_0 \left[r_q (1 - r_q) \right]^3 A_4(y_q), \tag{7.17}$$

where $\dfrac{|r - R_{q\,max}(z)|}{L_h} \le \dfrac{1}{2}$, $0 \le y_q \le \dfrac{1}{2}$, $r_q = \dfrac{|r - R_{q\,max}(z)|}{L_h} + \dfrac{1}{2}$, $y_q = \dfrac{z_{qtop} - z}{z_{qtop}}$, R_{qmax} is the radius of maximum heating, z_{qtop} is the height of heating, and L_h is the width of heating. In this study, the ramp functions in Eqs 7.16 and 7.17 varied from 0.5 to 0 for the range of y_q. As seen in Fig. 7.1, the high-order ramp function approached 0 more quickly with x approaching 0, and Q_H was larger than Q_L at a higher altitude. The

difference in vertical profile between Q_H and Q_L was as attributed to an increase in diabatic heating within the upper edge of the eyewall. These heat sources were scaled by Q_0 to produce a 1 m s^{-1} updraft with lower-tropospheric static stability ($w = Q/N^2$).

Hazelton and Hart (2013) indicated that the variation of eyewall slopes to horizontal ranged from 13° to 42°. In this study, the slope of the RMW was chosen as 12.5°, 22.5°, and 45°. The size of the RMW was 30 km at the bottom of model. The slopes of R_{qmax} were the same as those of RMW, but R_{qmax} was 28 km at a distance of 2 km within the RMW. Note that the top of the vortex was 18 km, and the latitude was considered as 10°. Figure 7.2 shows the balanced vortices with high and low heating rates for each slope.

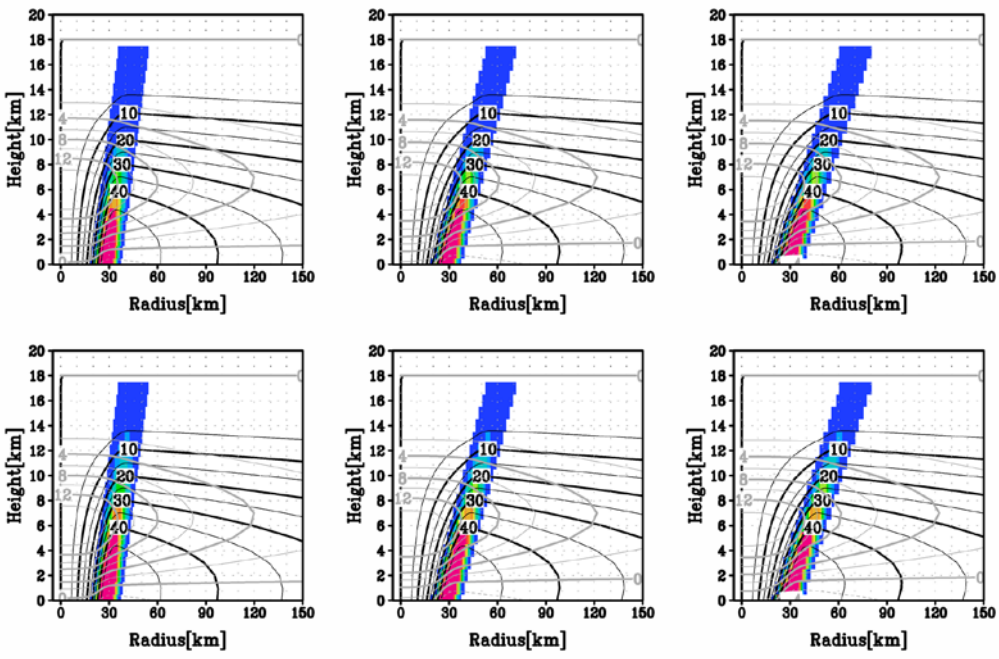

Fig. 7.2. Radius-height cross-sections of tangential wind (m s^{-1}: black lines), temperature anomalies relative to an environment (K: gray lines), and heating rate (m s^{-3}: color). The upper panels show balanced vortices with Q_L (Eq. 7.17), and the bottom panels show balanced vortices with Q_H (Eq. 7.16). The left, center, and right panels indicate eyewall slopes of 45°, 22.5°, and 12.5° to horizontal, respectively.

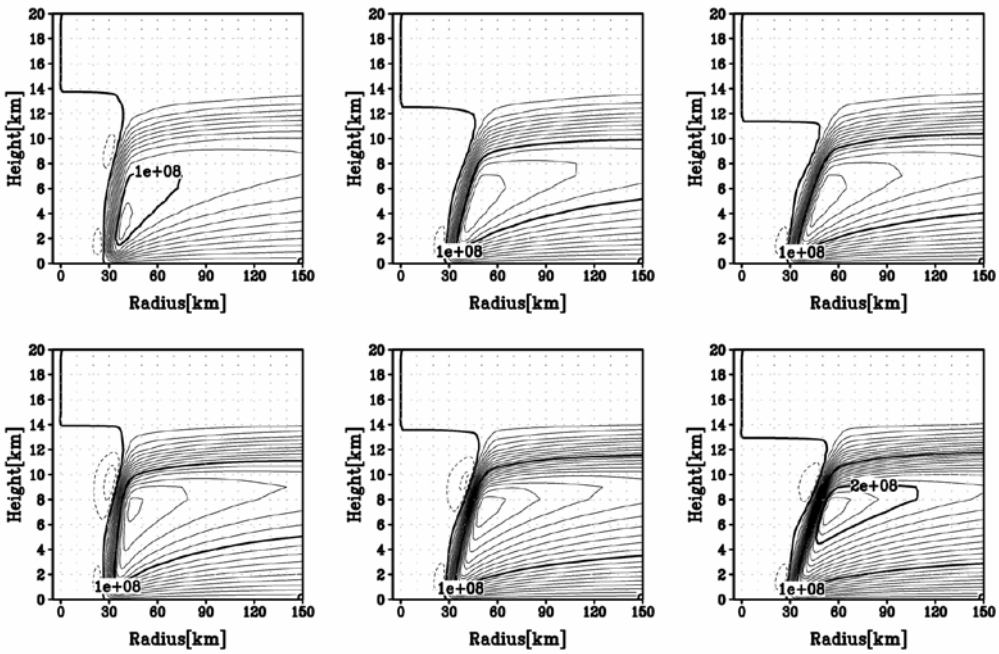

Fig. 7.3. Similar to Fig. 7.2 except for mass stream function (kg s^{-1}).

Figure 7.3 shows the mass stream functions for each vortex calculated from the Sawyer–Eliassen model. As the eyewall slopes more outward, the amplitude of the mass stream function becomes larger, which is a common feature of the balanced vortices with Q_H and Q_L. The surface tendencies of tangential wind were calculated from the mass stream function and Eqs 7.1, 7.6, and 7.7. For all these cases, the tendencies indicated that the tangential wind induced by the heat rate increased outside of the eyewall, and decreased inside (Fig 7.4 upper panels). Shapiro and Willoughby (1982) reported the same response as this study to the displacement of heating rate (Fig. 15; Shapiro and Willoughby 1982).

The differences in the tendency between the vortices with Q_H and Q_L are shown in the bottom panels of Fig 7.4. As heating rate increased in the upper edge of the eyewall, the tendencies became larger outside of the inner edge of the eyewall. This increase in the tendency was basically independent of the eyewall slope, although its

maximum shifted outward as the eyewall sloped more outward.

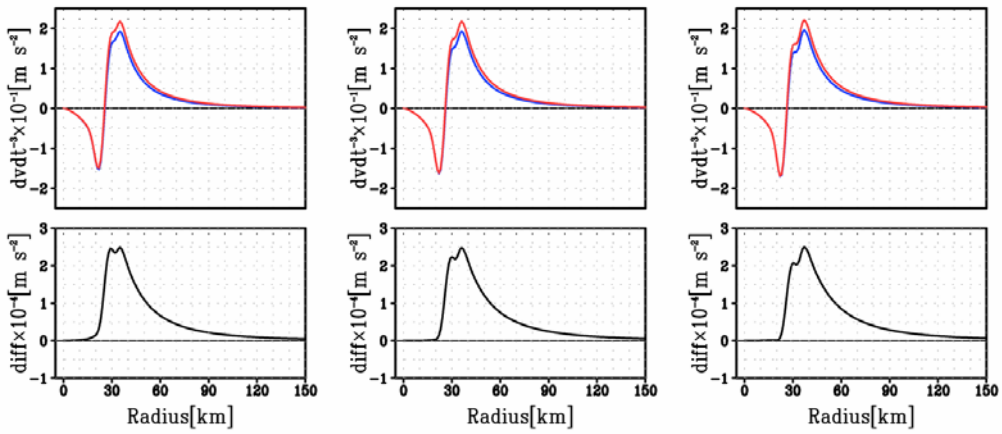

Fig. 7.4. The surface tendencies of tangential wind (m s^{-2}) induced by the heat rate. The upper panels show the tendencies for the balanced vortices with Q_L (Eq. 7.17; blue line) and Q_H (Eq. 7.16; red line). The bottom panels depict differences in the tendencies between the balanced vortices with Q_L and Q_H at the same eyewall slopes. The left, center, and right panels indicate eyewall slopes of 45°, 22.5°, and 12.5° to horizontal, respectively.

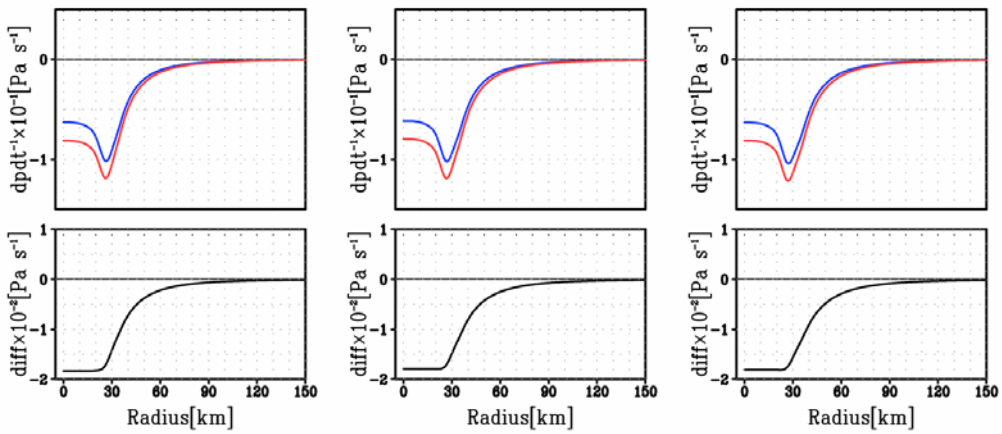

Fig. 7.5. Similar to Fig. 7.4 except for the surface tendency pressure (Pa s^{-1}) induced by the heating rate.

The upper panels of Fig. 7.5 depict the tendencies of surface pressure induced by the heating rate for each eyewall slope. The tendencies were maximized under the eyewall region for the vortices with Q_H and Q_L. This decrease resulted from an increase in the heating rate, which was consistent with the hydrostatic adjustment. The balanced

vortices with Q_H showed deeper pressure drops than those with Q_L (bottom panels of Fig. 7.5) for each eyewall slope. The slope of the eyewall did not influence the difference in the tendency of pressure between the vortices with Q_H and Q_L.

The Sawyer–Eliassen model confirmed that an increase in heating within the upper edge of the eyewall enhanced the tangential wind outside of the eyewall, which was independent of the eyewall slope. This supported the results of 14-km NICAM simulation, which showed an increase in the tangential wind outside of the eyewall because of a rise of the eyewall under warmer climate condition.

7.2 Effect of cumulus parameterization on tropical cyclone structures

We have discussed the future changes of the TC structure using outputs of the 14-km NICAM simulation without a cumulus parameterization (Kodama et al. 2015; Satoh et al. 2015). In this study, the outward slope of the eyewall plays an important role in the future change of the TC structure. This structure did not converge in spite of models employing a horizontal grid spacing of a few kilometers (Fierro et al. 2009; Gentry and Lackmann 2010; Sun et al. 2013). Generally, a horizontal grid spacing of 14 km was too coarse to simulate TCs, in which a cumulus parameterization should be implemented. In this subchapter, we investigated the effect of a cumulus parameterization on the eyewall of TCs simulated by the 14-km NICAM.

Figure 7.6 shows a composite structure of vertical velocity of C4 TCs simulated by the 14-km NICAM with a cumulus parameterization, which is referred to as a Chikira scheme (Chikira and Sugiyama 2010). The model configurations were similar to the AMIP-type NICAM simulation except for the use of the Chikira scheme.

This simulation was conducted for three months: from June to August 2004, and the number of C4 TCs was 3. Although the sample number was low, a clear eye was reproduced in the center of the TC.

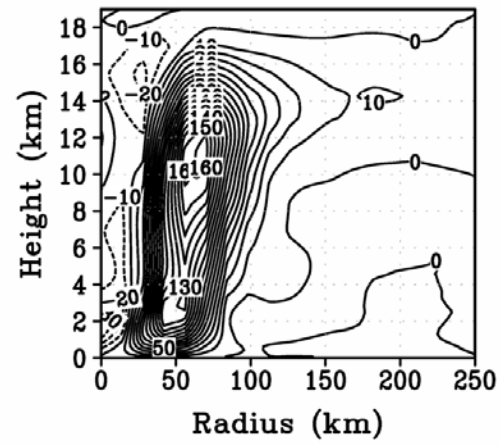

Fig. 7.6. Composites of vertical velocity (cm s^{-1}) of C4 TCs at their lifetime minimum SLP, obtained in the 14-km NICAM simulation with a Chikira scheme. The thin black lines are the radius–height cross-sections of the vertical velocity. The contour interval of the black lines is 1 (cm s^{-1}).

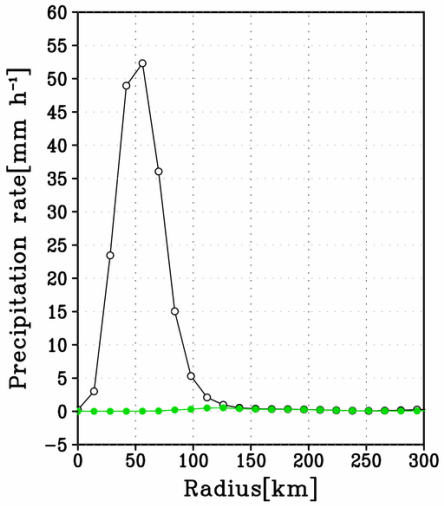

Fig. 7.7. Composites of two-type precipitations (mm h^{-1}) of C4 TCs at their lifetime minimum SLP, obtained in the 14-km NICAM simulation with a Chikira scheme. The black and green lines

Precipitations associated with TCs are typically separated into two-type precipitations, as seen in Fig. 7.7. One of them was calculated by a microphysical

process (Tomita 2008), and the other was calculated by the cumulus parameterization (Chikira and Sugiyama 2010). The precipitation by the cumulus parameterization is generally less than that of the microphysical process; thus, the cumulus parameterization contributed little to the precipitation associated with TCs simulated in this sensitivity experiment.

Based on Figs. 5.27 and 7.6, the 14-km NICAM simulation appeared to reproduce the outward slope of the eyewall with or without the use of a Chikira scheme. Manganello et al. (2014) discussed a composite structure of TCs simulated using a 16-km ECMWF model with a cumulus parameterization. Their TCs did not exhibit a clear eye of TC, as its eyewall did not slope outward; however, despite using a cumulus parameterization, the MRI AGCM simulated an eye of a TC (Murakami et al. 2012). The MRI AGCM may reproduce outward slope of the eyewall. This indicates that the slope of eyewall simulated in models is sensitive to the type of parameterization scheme implemented in the model. This issue should be discussed using outputs of many high-resolution models that include various cumulus parameterizations.

The World Climate Research Programme has planned the High Resolution Model Intercomparison Project, which is documented at the following location: http://www.wcrp-climate.org/index.php/modelling-wgcm-mip-catalogue/429-wgcm-hiresmip. Under this project, we will be able to obtain outputs of many high-resolution models, as well as examine the mechanisms of eyewall structure depending on different models and cumulus parameterization schemes.

Chapter 8 General Conclusion

TCs cause severe natural disasters, and the magnitude of damage by TCs is determined by their frequency, intensity, and horizontal scales. Moreover, the gain energy from oceans (Emanuel 2003), and the increase in SST enhances the intensity of TCs (Emanuel 1986). Since SST increases under warmer conditions, understanding how global warming influences the activities of TCs is important. Many researchers have investigated future changes in the activity of TCs such as the genesis frequency and intensity using AGCMs (Knutson et al. 2010). The previous studies projected decreases in the global frequency of TCs, but increases in rate of intense TCs to total TCs. A few studies focused on the structural change of TCs due to global warming under realistic conditions. Observational studies indicated that the structure of a TC such as the size of the RMW changes between stages of its lifecycle. Even though TCs are in the same stage, their structure varies from TC to TC, and the intensity of TCs slightly influences the horizontal scale (Merill 1984; Weatherford and Gray 1988; Kimball and Mulekar 2004). These variations impose a statistical comparison between TC structures in the present-day and warmer climate conditions.

Recently, as computational performance has rapidly improved, we can conduct a simulation with a high-resolution model. Kodama et al. (2015) completed an AMIP-type simulation using a horizontal 14-km mesh NICAM without a cumulus parameterization, which was conducted for more than 30 years (June 1978 to December 2008), and reproduced global TC genesis that is consistent with observed TC genesis. Moreover, they conducted a future simulation (June 2074 to December 2104) using the same model, which was configured with the same setting. These simulations provided

TC information for 30 years in the present-day and in future climate conditions for us. In this thesis, we statistically investigated future changes in the TC structure by using their outputs.

In Chapter 3, we demonstrated that NICAM could reproduce TC activities, such as cyclone genesis, intensity, seasonal cycle, and interannual variability. The present-day simulation successfully simulated the seasonal cycle but did not completely reproduce the geographical distribution of TC genesis. For instance, NICAM simulated fewer TCs over the Atlantic compared to observations. This discrepancy was linked to precipitation bias, which was reported by Kodama et al. (2015) and discussed by McDonald et al. (2005). Therefore, models should completely simulate TC activity in the present-day climate condition to project more reliable future changes in the TC activity, and we should disclose what causes the precipitation bias.

In Chapter 4, future changes in the TC activity were shown, where the genesis ratio of intense TCs to total TCs increased, although the global number of generated TCs reduced. This result was consistent with the results of previous studies (Knutson et al., 2010), even though a nonhydrostatic model without a cumulus parameterization was employed. Note that mechanisms of changes in TC frequencies were not discussed in this study; however, using the same outputs, Satoh et al. (2015) determined that that rate of convective mass flux associated with TCs to the total convective mass flux in the tropics is proportional to the intensity of the TC, and the rate is almost unchanged between both climate conditions. Moreover, they proposed a constraint on the genesis of TCs through a diagnostic relation based on the convective mass flux, where intense TCs increase due to global warming and consequently the number of TCs decreases.

In Chapter 5, we showed future changes in TC structures, which were

simulated by the 14-km NICAM simulation. First, NICAM projected that the cloud top height of TCs became taller with increasing intensity. Under warmer climate conditions, the height was taller than that in the present-day climate condition even though TCs had the same SLP for both climate conditions. The response to global warming is linked to a rise of tropopause height (Manabe and Strickler 1964; Manabe and Wetherald 1967). These results were first documented in Yamada et al. (2010) using outputs of another 14-km NICAM simulation. In this thesis, Their finding was reconstructed using the outputs of Kodama et al. (2015), because the present-day simulation of Kodama et al. (2015) simulated about fifty times as many TCs as that of Yamada et al. (2010). The results from the present study are consistent with Yamada et al. (2010).

The elevation of the top height influenced the amount of water contents associated with TCs. The NICAM projected that IWP and LWP increased because of global warming; moreover, these increases resulted from increases in the melting level and tropopause height due to an increase in water vapor under warmer climates. Accordingly, the water contents associated with TCs increased due to global warming. A similar result has been described in Yamada and Satoh (2013), which used outputs of Yamada et al. (2010). In this study, their results were reconstructed using the outputs of Kodama et al. (2015). In this simulation, the RMW was consistent with the maximum radius of the LWP, which is characterized as the eyewall radius. Furthermore, observational studies (Jorgensen 1984a,b) showed the same relationship between the positions of the RMW and the eyewall radius. The NICAM simulated that these radii became wider with their SLP deepening, where intense TCs (C2–C5) exhibited a clear eye, but weak TCs (C0–C1) did not, and the radius of maximum IWP was larger than that of the LWP (i.e., the eyewall sloped outward with height in the 14-km NICAM

simulation).

Radial profiles of tangential wind velocity were compared between the same intensity categories for the present-day and future simulations. In the 14-km NICAM simulation, the tangential velocity increased outside the outer edge of the eyewall. These changes resulted from a decrease in SLP under warmer climates. The decrease in SLP was maximized under the outer edge of the eyewall, which increased the radial pressure gradient outside the outer edge of the eyewall. Consequently, the tangential velocity increased outside of the outer edge of eyewall due to global warming. This finding was supported by the 7-km NICAM simulation (Chapter 6). The 14-km simulation predicted that the RMW was widened under warmer conditions. However, the 7-km simulation did not support the increases in the size of RMW. We could not conclude a response of the size of RMW to global warming.

The decrease in SLP was related to the elevated tropopause height under global warming. The top of the eyewall reached the elevated tropopause height and increased the diabatic heating in the upper edge of the eyewall. The increased diabatic heating warms the atmosphere and decreases the SLP underneath the heating area primarily by hydrostatic adjustment (Smith 1981; Wang 2009), which alters the radial pressure gradient. The mechanism of increase in tangential velocity is schematically presented in Fig. 8.1.

As the eyewall slopes outward with height, the decrease in SLP maximizes under the outer edge of the eyewall. The eyewall slope determines the radius of the maximum decrease in the SLP, and plays a primary role in this mechanism. Observational studies indicated that the eyewall slopes outward with height (Jorgensen 1984b; Stern and Nolan 2009; Hazelton and Hart 2013; Stern et al. 2014) as seen in the

14-km NICAM simulation. Using the RCM, the degree of eyewall slope does not converge even though the RCM employs a simulated horizontal grid spacing of a few kilometers (Fierro et al. 2009; Gentry and Lackmann 2010; Sun et al. 2014). These simulations showed that the eyewall slope becomes more upright as the horizontal grid interval becomes smaller.

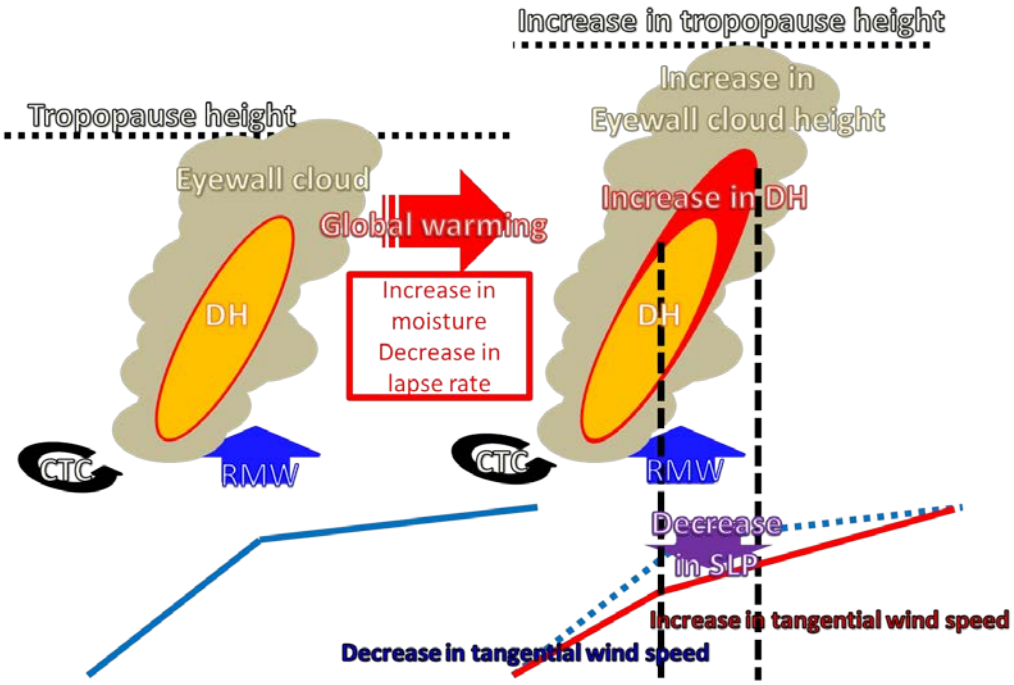

Fig. 8.1. Schematic showing the effect of an upward extension of the eyewall cloud height on the tangential wind speed. The radial distributions of SLP in the present-day climate (blue solid and dotted lines) and under a warmer climate (red solid line) are shown. The CTC, RMW, and DH are the abbreviated terms for the center of the TC, radius of maximum wind, and diabatic

The effect of the eyewall slope on the increase in tangential wind outside the outer edge of the eyewall is important and should be investigated. In Chapter 7, the Sawyer–Eliassen model (Pendargrass and Willoughby, 2009) was applied to artificially adjust the locus of diabatic heating, which is controlled by the slope of the eyewall. Following Hazelton and Hart (2013), the slope of eyewall was chosen as 12.5°, 22.5°, and 45° to the horizontal. As the heating rate was observed to increase in the upper edge

of eyewall for each slope, all the cases showed that the SLP decreased under the eyewall due to the increase in heating rate, which caused the tangential velocity to increase on the outside. The increase in tangential wind outside the eyewall was independent of the degree of the eyewall slope. Based on these results, we concluded that the tangential velocity outside the outer edge of the eyewall was enhanced due to global warming when TCs in the present-day and warmer climate conditions were compared at the same intensity category.

Acknowledgments

I am most grateful to Prof. Masaki Satoh for supporting all of my research activities. I also thank Prof. Masahide Kimoto and Dr. Masato Sugi for important advice and many useful discussions throughout the project. Several other comments and suggestions were provided by Prof. Hiroshi Niino, Prof. Hiroaki Miura, Prof. Akira Oka, and Prof. Yukari N. Takayabu at the University of Tokyo. Appreciation is extended to Dr. Chihiro Kodama, Dr. Masuo Nakano, Dr. Akira T. Noda, Dr. Tomoe Nasuno, Dr. Tatsuya Seiki, Dr. Ying-Wen Chen, Dr. Kazuyoshi Oouchi, Dr. Akira Yamazaki, Dr. Hiroaki Tatebe, Dr. Keigo Matsuda, Dr. Kozo Nakamura, Dr. Shingo Watanabe and Ms. Mikiko Ikeda of the Japan Agency Marine-earth Science and Technology; also to Dr. Wataru Yanase, Dr. Takashi Sakamoto, Dr. Tomoki Miyakawa, Dr. Tomoki Ohno, Dr. Woosub Roh, Dr. Hiroyasu Kubokawa, Dr. Naomi Kuba, Mr. Yuki Nishikawa and Mr. Daisuke Takasuka at the University of Tokyo; also to Dr. Yoshiaki Miyamoto, Dr. Ryuji Yoshida, Dr. Yoshiyuki Kajikawa, Dr. Hisashi Yashiro, Dr. Shin-ichi Iga, Dr. Tsuyoshi Yamaura, Dr. Sachiho A. Adachi and Dr. Hirofumi Tomita at the RIKEN Advanced Institute for Computational Science; and to Dr. Hiroshi Taniguchi, Dr. Masayuki Hara, Dr. Kazuyoshi Kikuchi, Dr. Sachie Kanada, Dr. Fumichika Uno and Dr. Hiroaki Kawase. I also thank Prof. Tetsuya Takemi at Kyoto University. Their advice and cooperation have consistently helped my studies and life. Finally, I am grateful to my parents.

Appendix

Consideration of the thermal wind balance and conservation of angular momentum explains the outward slope of the RMW. To satisfy the thermal wind balance in a vortex with a warm core in its center, the tangential velocity and absolute angular momentum decreases with height.

At point A, which is the RMW of any altitude (z), the absolute angular momentum (M_a) is written as follows:

$$M_a = M(r,z) = v(r,z)r + \frac{1}{2} fr^2, \tag{A.1}$$

where r, z, v, and f indicate the RMW, height, tangential velocity, and the Coriolis parameter. The M_b value is the angular momentum at point B, which moved from A to higher altitudes along a curve that connected RMWs at each altitude, and is written as follows:

$$M_b = M(r+\Delta r, z+\Delta z) = v(r+\Delta r, z+\Delta z)(r+\Delta r) + \frac{1}{2} f(r+\Delta r)^2, \tag{A.2}$$

where $\Delta r << r$, $0 < \Delta z << z$. The Taylor expansion of Eq. A.2 is as follows:

$$\begin{aligned} & M_b \\ & = (r+\Delta r)\left(v + \frac{\partial v}{\partial r}\Delta r + \frac{\partial v}{\partial z}\Delta z + \frac{\partial^2 v}{\partial r \partial z}\Delta r \Delta z + ... \right) + \frac{1}{2} f(r+\Delta r)^2 \\ & \approx vr + r\frac{\partial v}{\partial r}\Delta r + r\frac{\partial v}{\partial z}\Delta z + v\Delta r + \frac{1}{2} fr^2 + fr\Delta r, \end{aligned} \tag{A.3}$$

where the products of infinitesimals were ignored. To satisfy the thermal wind balance, the tangential velocity becomes weaker with height. Consequently, $M_a > M_b$. Subtracting Eq. A.1 from Eq. A.3,

$$M_b - M_a = \left(r\frac{\partial v}{\partial r} + v + fr \right)\Delta r + r\frac{\partial v}{\partial z}\Delta z < 0. \tag{A.4}$$

$$\frac{\Delta z}{\Delta r} < -\left(\frac{\partial v}{\partial r} + \frac{v}{r} + f\right)\left(\frac{\partial v}{\partial z}\right)^{-1}. \quad \text{(A.5)}$$

Because $r = RMW$, $\frac{\partial v}{\partial r} = 0$. Eq. A.5 is rewritten as follows:

$$\frac{\Delta z}{\Delta r} < -\left(\frac{v}{r} + f\right)\left(\frac{\partial v}{\partial z}\right)^{-1}. \quad \text{(A.6)}$$

We can obtain the upper limit of the slope of the RMW curve as follows:

$$\frac{\Delta z}{\Delta r} < -\left(\frac{v}{r} + f\right)\left(\frac{\partial v}{\partial z}\right)^{-1}. \quad \text{(A.7)}$$

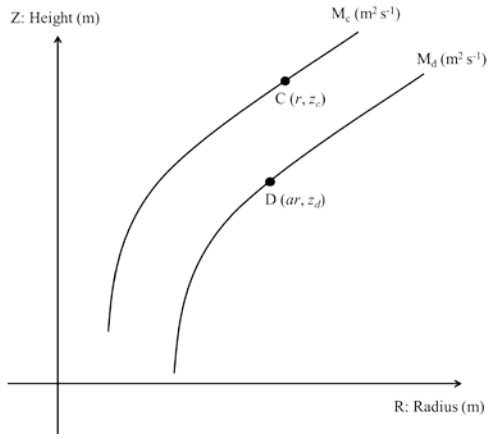

Fig. A.1. Schematic of definition of points C and D.

Next, we assume a maximum tangential velocity at point C(r, z_c) as shown in Fig. A.1. The absolute angular momentum at C is defined as follows:

$$M_c = vr + \frac{1}{2} fr^2. \quad \text{(A.8)}$$

We define point D(ar, z_d) at which the wind velocity equals the maximum tangential velocity at C, where $z_d < z_c$. The absolute angular momentum at D is defined as follows:

$$M_d = avr + \frac{1}{2} a^2 fr^2. \quad \text{(A.9)}$$

Eliminating v from Eqs. A.8 and A.9,

$$M_d - aM_c = \frac{1}{2} fr^2 a(a-1). \quad \text{(A.10)}$$

If $a = 1$, then $M_d = M_c$, which does not satisfy the thermal wind balance. If $0 < a < 1$, then Eq. A.10 is rewritten as $M_d - aM_c < 0$. Here because $M_d > M_c$, aM_c should not be larger than M_d. If $a > 1$, then Eq. A.10 is rewritten as $M_d - aM_c > 0$. Note that only this condition is satisfied in the three conditions. Considering point E(r, z_d), the tangential velocity at E should be larger than that at C in order to satisfy the thermal wind balance. The RMW at a height of z_d is located within point E. Thus, a bottom limit of the RMW slope is written as follows:

$$0 < \frac{\Delta z}{\Delta r}. \quad \text{(A.11)}$$

From Eqs. A.7 and A11, we obtain the range of the RMW slope:

$$0 < \frac{\Delta z}{\Delta r} < -\left(\frac{v}{r} + f\right)\left(\frac{\partial v}{\partial z}\right)^{-1}. \quad \text{(A.12)}$$

References

Adler, R. F., and Coauthors, 2003: The version-2 global precipitation climatology project (GPCP) monthly precipitation analysis (1979–present). J. Hydrometeorol., 4, 1147–1167, doi:10.1175/1525-7541(2003)004<1147:TVGPCP>2.0.CO;2.

Atkinson, G. D., and C. R. Holliday, 1977: Tropical cyclone minimum sea level pressure/maximum sustained wind relationship for the western North Pacific. Mon. Wea. Rev., 105, 421–427, doi:10.1175/1520-0493(1977)105<0421:TCMSLP>2.0.CO;2.

Bengtsson, L., M. Botzet, and M. Esch, 1996: Will greenhouse gas-induced warming over the next 50 years lead to higher frequency and greater intensity of hurricanes? Tellus A, 48, 57–73, doi:10.1034/j.1600-0870.1996.00004.x.

Bister, M., and K. A. Emanuel, 1998: Dissipative heating and hurricane intensity. Meteorol. Atmos. Phys., 65, 233-240, doi:10.1007/BF01030791.

Bister, M., and K. A. Emanuel, 2002: Low frequency variability of tropical cyclone potential intensity: 1. Interannual to interdecadal variability. J. Geophys. Res., 107(D24), 4801, doi: 10.1029/2001JD000776.

Broccoli, A. J., and S. Manabe, 1990: Can existing climate models be used to study anthropogenic changes in tropical cyclone climate? Geophys. Res. Lett., 17, 1917–1919, doi:10.1029/GL017i011p01917.

Camargo, S. J., A. H. Sobel, A. G. Barnston, and K. A. Emanuel, 2007: Tropical cyclone genesis potential index in climate model. Tellus, 59A, 428–443, doi:10.1111/j.1600-0870.2007.00238.x.

Camargo, S. J., 2013: Global and regional aspects of tropical cyclone activity in the CMIP5 models. J. Climate, 26, 9880–9902, doi:10.1175/JCLI-D-12-00549.1.

Chan, J. C. L., 1985: Tropical cyclone activity in the northwest Pacific in relation to the El Niño/Southern Oscillation phenomenon. Mon. Wea. Rev., 113, 599–606. doi:10.1175/1520-0493(1985)113<0599:TCAITN>2.0.CO;2.

Chavas, D. R., and K. A. Emanuel, 2010: A QuickSCAT climatology of tropical cyclone size. Geophys. Res. Lett., 37, L18816, doi:10.1029/2010GL044558.

Chavas, D. R., and K. Emanuel, 2014: Equilibrium tropical cyclone size in an idealized state of axisymmetric radiative-convective equilibrium. J. Atmos. Sci., 71, 1663–1680, doi:10.1175/JAS-D-13-0155.s1.

Chikira, M., Sugiyama, M., 2010: A Cumulus Parameterization with State-Dependent Entrainment Rate. Part I: Description and Sensitivity to Temperature and Humidity Profiles. J. Atmos. Sci., 67, 2171–2193, doi:10.1175/2010JAS3316.1.

Chu, J. –H., C. R. Sampson, A. S. Levine, and E. Fukada, 2002: The Joint Typhoon Warming Center tropical cyclone best-tracks, 1945-2000. NRL Tech. Rep. NRL/MR/7540-02-16. [Available online at http://www.usno.navy.mil/NOOC/nmfc-ph/RSS/jtwc/best_tracks/TC_bt_report.html]

Dee, D. P., and the coauthors, 2011: The ERA-Interim reanalysis: configuration and performance of the data assimilation system. Quart. J. Roy. Meteor. Soc., 137, 553–597, doi:10.1002/qj.828.

Ebita, A., S. Kobayashi, Y. Ota, M. Moriya, R. Kumabe, K. Onogi, Y. Harada, S. Yasui, K. Miyaoka, K. Takahashi, K. Kamahori, C. Kobayashi, H. Endo, M. Soma, Y. Oikawa, and T. Ishimizu, 2011: The Japanese 55-year reanalysis “JRA-55”: An interim report. SOLA, 7, 149–152, doi:10.2151/sola.2011-038.

Eliassen, A., 1951: Slow thermally or frictionally controlled meridional circulation in a circular vortex. Astrophys. Norv., 5, 19–60. [Available online at http://adsabs.harvard.edu/full/1951apnr....5...19e]

Emanuel, K. A., 1986: An air-sea interaction theory for tropical cyclone. Part I: steady-state maintenance, J. Atmos. Sci., 43, 585–604, doi:10.1175/1520-0469(1986)043<0585:AASITF>2.0.CO;2.

Emanuel, K. A., 1987: The dependence of hurricane intensity on climate. Nature, 326, 483–485, doi:10.1038/326483a0.

Emanuel, K. A., 1995: Sensitivity of tropical cyclones to surface exchange coefficients and a revised steady-state model incorporating eye dynamics. J. Atmos. Sci., 52, 3969-3976, doi:10.1175/1520-0469(1995)052<3969:SOTCTS>2.0.CO;2.

Emanuel, K. A., 2003: Tropical cyclones. Annu. Rev. Earth Planet. Sci., 31, 75-104, doi:10.1146/annurev.earth.31.100901.141259.

Emanuel, K. A., and D. S. Nolan, 2004: Tropical cyclone activity and global climate. Preprints, 26th Conf. on Hurricanes and Tropical Meteorology, Miami, FL, Amer. Meteor. Soc., 240–241. [Available online at https://ams.confex.com/ams/26HURR/techprogram/paper_75463.htm]

Emanuel, K. A., R. Sundararajan, and H. Williams, 2008: Hurricanes and global warming: results from downscaling IPCC AR4 simulations. Bull. Amer. Metor. Soc., 89, 347–367, doi:10.1175/BAMS-89-3-347.

Fierro, A. O., R. F. Rogers, and F. D. Marks, D. S. Nolan, 2009: The impact of horizontal grid spacing on the microphysical and kinematic structures of strong tropical cyclones simulated with the WRF-ARW model. Mon. Wea. Rev., 137, 3717-3743, doi: 10.1175/2009MWR2946.1.

Gates, W. L., 1992: AMIP - The atmospheric model intercomparison project. Bull. Amer. Meteor. Soc., 73, 1962–1970, doi:10.1175/1520-0477(1992)073<1962:ATAMIP>2.0.CO;2.

Gentry, M. S., and G. M. Lackmann, 2010: Sensitivity of simulated tropical cyclone structure and intensity to horizontal resolution. Mon. Wea. Rev., 138, 688-704, doi: 10.1175/2009MWR2976.1.

Gray, W. M., 1968: Global view of the origin of tropical disturbances and storms. Mon. Wea. Rev., 96, 669–700, doi:10.1175/1520-0493(1968)096<0669:GVOTOO>2.0.CO;2.

Gray, W. M., 1998: The formation of tropical cyclones. Meteorol. Atmos. Phys., 67, 37–69, doi:10.1007/BF01277501.

Hazelton, A. T., and R. E. Hart, 2013: Hurricane eyewall slope as determined from airborne radar reflectivity data: Composites and case studies. Weath. And Forecsting, 28, 368-386, doi:10.1175/WAF-D-12-00037.1.

Holland, G. J., 1980: An analytic model of the wind and pressure profiles in hurricanes. Mon. Wea. Rev., 108, 1212-1218, doi:10.1175/1520-0493(1980)108<1212:AAMOTW>2.0.CO;2.

IPCC, 2013: Climate Change 2013: The Physical Science Basis. Contribution of Working Group I to the Fifth Assessment Report of the Intergovern-mental Panel on Climate Change [Stocker, T.F., D. Qin, G.-K. Plattner, M. Tignor, S.K. Allen, J. Boschung, A. Nauels, Y. Xia, V. Bex and P.M. Midgley (eds.)]. Cambridge University Press, Cambridge, United Kingdom and New York, NY, USA, 1535 pp.

Jarvinen, B. R., C. J. Neumann, and M. A. S. Davis, 1984: Atropical cyclone data tape for the North Atlantic basin, 1886-1983: Contents, limitations, and uses. NOAA Tech. Memo. NWS NHC 22, 21 pp. [Available online at http://www.nhc.noaa.gov/pdf/NWS-NHC-1988-22.pdf]

Jorgensen, D. P., 1984a; Mesoscale and convective-scale characteristics of mature hurricanes. Part I: General observations by research aircraft. J. Atmos. Sci., 41, 1268–1286, doi:10.1175/1520-0469(1984)041<1268:MACSCO>2.0.CO;2.

Jorgensen, D. P., 1984b; Mesoscale and convective-scale characteristics of mature hurricanes. Part II: Inner core structure of hurricane Allen (1980). J. Atmos. Sci., 41, 1287–1311, doi:10.1175/1520-0469(1984)041<1287:MACSCO>2.0.CO;2

Jung, T., and Coauthors, 2012: High-resolution global climate simulations with the ECMWF model in Project Athena: Experimental design, model climate and seasonal forecast skill. J. Climate, 25, 3155–3172, doi:10.1175/JCLI-D-11-00265.1.

Kanada, S., A. Wada, and M. Sugi, 2013: Future changes in structures of extremely intense tropical cyclones using a 2-km mesh nonhydrostatic model. J. Climate, 26, 9986–10 005, doi:10.1175/JCLI-D-12-00477.1.

Kimball, S. K, and M. S. Mulekar, 2004: A 15-year climatology of North Atlantic

tropical cyclone. Part I: Size Parameters. J. Climate, 17, 3555-3575, doi:10.1175/1520-0442(2004)017<3555:AYCONA>2.0.CO;2.

Knapp, K. R., and M. C. Kruk, 2010: Quantifying interagency differences in tropical cyclone best-track wind speed estimates. Mon. Wea. Rev., 138, 1459–1473, doi:10.1175/2009MWR3123.1

Knapp, K. R., M. C. Kruk, D. H. Levinson, H. J. Diamond, and C. J. Neumann, 2010: The International Best Track Archive for Climate Stewardship (IBTrACS): Unifying tropical cyclone data. Bull. Amer. Meteor. Soc., 91, 363–376, doi:10.1175/2009BAMS2755.1.

Knutson, T. R., and R. E. Tuleya, 1999: Increased hurricane intensities with CO2-induced warming as simulated using GFDL hurricane prediction system, Climate Dyn., 15, 503–186, doi:10.1007/s003820050296.

Knutson, T. R., and Coauthors, 2010: Tropical cyclones and climate change, Nature Geosci., 3, 157–163, doi:10.1038/NGEO779.

Kodama, C., and Coauthors, 2015: A 20-year climatology of a NICAM AMIP-type simulation. J. Meteor. Soc. Japan, 93, 393–424, doi:10.2151/jmsj.2015-024.

Malkus, J. S., 1958: On the structure and maintenance of the mature hurricane eye. J. Meteor., 15, 337–349, doi:10.1175/1520-0469(1958)015<0337:OTSAMO>2.0.CO;2.

Manabe, S., and R. F. Strickler, 1964: Thermal Equilibrium of the atmosphere with a convective adjustment. J. Atmos. Sci., 21, 361-385, doi:10.1175/1520-0469(1964)021<0361:TEOTAW>2.0.CO;2.

Manabe, S., and R. Wetherald, 1967: Thermal equilibrium of the atmosphere with a given distribution of 319 relative humidity. J. Atmos. Sci., 24, 241–259, doi:10.1175/1520-0469(1967)024<0241:TEOTAW>2.0.CO;2.

Manganello, J. V., and Coauthors, 2012: Tropical cyclone climatology in a 10-km global atmospheric GCM: toward weather-resolving climate modeling. J. Climate, 25, 3867–3893, doi:10.1175/JCLI-D-11-00346.1.

Manganello, J. V., and Coauthors, 2014: Future changes in the western north pacific tropical cyclone activity projected by a multidecadal simulation with a 16-km global atmospheric GCM. J. Climate, 27, 7622–7646, doi:10.1175/JCLI-D-13-00678.1.

McDonald, R. E., D. G. Bleaken, D. R. Cresswell, V. D. Pope, C. A. Senior, 2005: Tropical storms: representation and diagnosis in climate models and the impacts of climate change. Climate Dyn., 25, 19–36, doi:10.1007/s00382-004-0491-0.

Meehl, G., C. Covey, T. Delworth, M. Latif, B. McAvaney, J. Mitchell, R. Stouffer, and K. Taylor, 2007: The WCRP CMIP3 multimodel dataset: A new era in climate change research. Bull. Amer. Meteorol. Soc., 88, 1383–1394, doi:10.1175/BAMS-88-9-1383.

Merril, R. T., 1984: A comparison of large and small tropical cyclone. Mon. Wea. Rev., 112, 1408–1418, doi:10.1175/1520-0493(1984)112<1408:ACOLAS>2.0.CO;2.

Miyamoto, Y., and T. Takemi, 2013: A transition mechanism for the spontaneous axisymmetric intensification of tropical cyclones. J. Atmos. Sci., 70, 112−129, doi:10.1175/JAS-D-11-0285.1

Mizuta, R., Y. Adachi, S. Yukimoto, and S. Kusunoki 2008: Estimation of the future distribution of sea surface temperature and sea ice using the CMIP3 multi-model ensemble mean, Tech. Rep. 56, Meterol. Res. Inst., Tsukuba, Japan, doi:10.11483/mritechrepo.56.

Mori, M., and Coauthors, 2013: Hindcast prediction and nearfuture projection of tropical cyclone activity over the western North Pacific using CMIP5 near-term experiments with MIROC. J. Meteor. Soc. Japan, 91, 431–452, doi:10.2151/jmsj.2013-402.

Murakami, H., and M. Sugi, 2010: Effect of model resolution on tropical cyclone climate projections.SOLA, 6, 73–76, doi:10.2151/sola.2010-019.

Murakami, H., and Coauthors, 2012: Future changes in tropical cyclone activity projected by the new high-resolution MRI-AGCM. J. Climate, 25, 3237–3260. doi:10.1175/JCLI-D-11-00415.1.

Murakami, H., P. - C. Hsu, O. Arakawa, T. Li, 2014: Influence of model biases on projected future changes in tropical cyclone frequency of occurrence. J. Climate, 27, 2159–2181, doi:10.1175/JCLI-D-13-00436.1.

Nakanishi, M. and H. Niino, 2006: An improved Mellor-Yamada level-3 model: Its numerical stability and application to a regional prediction of advection fog. Boundary-Layer Meteorol., 119, 397–407, doi:10.1007/s10546-005-9030-8.

Noda, A. T., K. Oouchi, M Satoh, H. Tomita, S. Iga, and Y. Tsushima, 2010: Importance of the subgrid-scale turbulent moist process: Cloud distribution in global cloud-resolving simulations. Atmos. Res., 96, 208–217, doi:10.1016/j.atmosres.2009.05.007.

Ohno, T., and M. Satoh, 2015: On the warm core of a tropical cyclone formed near the tropopause. J. Atmos. Sci., 72, 551-571, doi: 10.1175/JAS-D-14-0078.1.

Oouchi, K., J. Yoshimura, H. Yoshimura, R. Mizuta, S. Kusunoki, and A. Noda, 2006; Tropical cyclone climatology in a global-warming climate as simulated in a 20 km-mesh global atmospheric model: frequency and wind Intensity analyses. 84, 259–276, doi: http://doi.org/10.2151/jmsj.84.259

Pendergrass, A. G., H. E. Willoughby, 2009: Diabatically induced secondary flows in tropical cyclones. Part I: Quasi-Steady forcing. Mon. Wea. Rev., 137, 805–821, doi:10.1175/2008MWR2657.1.

Rayner, N., D. Parker, E. Horton, C. Folland, L. Alexander, D. Rowell, E. Kent, A. Kaplan, 2003: Global analyses of sea surface temperature, sea ice, and night marine air temperature since the late nineteenth century. J. Geophys. Res., 108(D14), 4407, doi:10.1029/2002JD002670

Reynolds, R. W., N. A. Rayner, T. M. Smith, D. C. Stokes, and W. Q. Wang, 2002: An improved in situ and satellite SST analysis for climate, J. Clim., 15, 1609–1625, doi:10.1175/1520-0442(2002)015<1609:AIISAS>2.0.CO;2.

Roberts, M. J., P. L. Vidale, M. S. Mizielinski, M.-E. Demory, R. Schiemann, J.

Strachan, K. Hodges, R. Bell, and J. Camp, 2015: Tropical cyclones in the UPSCALE ensemble of high-resolution global climate models. J. Climate, 28, 574–596, doi: http://dx.doi.org/10.1175/JCLI-D-14-00131.1

Satoh, M., T. Matsuno, H. Tomita, H. Miura, T. Nasuno, S. Iga, 2008: Nonhydrostatic Icosahedral Atmospheric Model (NICAM) for global cloud resolving simulations. Journal of Computational Physics, 227, 3486–3514, doi:10.1016/j.jcp.2007.02.006.

Satoh, M., and Coauthors, 2012: The Intra-Seasonal Oscillation and its control of tropical cyclones simulated by high-resolution global atmospheric models. Climate Dyn., 39, 2185–2206, doi:10.1007/s00382-011-1235-6.

Satoh, M., and Coauthors, 2014: The non-hydrostatic icosahedral atmospheric model: description and development. Progress in Earth and Planetary Science, 1, 18, doi:10.1186/s40645-014-0018-1.

Satoh, M., Y. Yamada, M. Sugi, C. Kodama, and A. T. Noda, 2015: Constraint on future change in global frequency of tropical cyclones due to global warming. J. Meteor. Soc. Japan, 93, 489–500, doi:10.2151/jmsj.2015-025.

Sekiguchi, M. and T. Nakajima, 2008: A k-distribution-based radiation code and its computational optimization for an atmospheric general circulation model. J. Quant. Spectrosc. Radiat. Transfer, 109, 2779–2793, doi:10.1016/j.jqsrt.2008.07.013.

Shapiro, L. J., and H. E. Willoughby, 1982: The Response of Balanced Hurricanes to Local Sources of Heat and Momentum. J. Atmos. Sci., 39, 378–394. doi: 10.1175/1520-0469(1982)039<0378:TROBHT>2.0.CO;2.

Skamarock, W. C., J. B. Klemp, J. Dudhia, D. O. Gill, D. M. Barker, W. Wang, and J. G. Powers, 2005: A description of the Advanced Research WRF Version 2. NCAR Tech. Note, NCAR/TN-4681ST, 88 pp.

Smith, R. K., 1981: The cyclostrophic adjustment of vortices with application to tropical cyclone modification. J. Atmos. Sci., 38, 2021–2030, doi: 10.1175/1520-0469(1981)038<2021:TCAOVW>2.0.CO;2.

Strachan, J., P. L. Vidale, K. Hodges, M. Roberts, and M.-E. Demory, 2013: Investigating global tropical cyclone activity with a hierarchy of AGCMs: The role of model resolution. J. Climate, 26, 133–152, doi:10.1175/JCLI-D-12-00012.1.

Stern, D. P., and D. S. Nolan, 2009: Reexamining the vertical structure of tangential winds in tropical cyclones: Observations and theory. J. Atmos. Sci., 66, 3579–3600, doi:10.1175/2009JAS2916.1.

Stern, D. P., J. R. Brisbois D. S. Nolan, 2014: An expanded dataset of hurricane eyewall sizes and slopes. J. Atmos. Sci., 71, 2747-2762, doi:10.1175/JAS-D-13-0302.1.

Sugi, M., A. Noda, N. Sato, 2002: Influence of the global warming on tropical cyclone climatology: An experiment with the JMA global model. J. Meteor. Soc. Japan, 80, 249–272, doi:10.2151/jmsj.80.249.

Sugi, M., H. Murakami, and J. Yoshimura, 2009: A reduction in global tropical cyclone frequency due to global warming. SOLA, 5, 1–4, doi:10.2151/sola.2009-042.

Sugi, M., and J. Yoshimura, 2012: Decreasing trend of tropical cyclone frequency in 228-year high-resolution AGCM simulations. Geophys. Res. Lett., 39, L19805, doi:10.1029/2012GL053360.

Sun, Y., L. Yi, Z. Zhong, Y. Hu, and Y. Ha, 2013: Dependence of model convergence on horizontal resolution and convective parameterization in simulations of tropical cyclone at gray-zone resolution. J. Geophys. Res., 118, 7715-7732, doi:10.1002/jgrd.50606.

Takata, K., S. Emori, and T. Watanabe, 2003: Development of the minimal advanced treatments of surface interaction and runoff. Global and Planetary Change, 38, 209–222, doi:10.1016/S0921-8181(03)00030-4.

Tomita, H., and M. Satoh, 2004: A new dynamical framework of nonhydrostatic global model using the icosahedral grid. Fluid Dyn. Res., 34, 357–400, doi:10.1016/j.fluiddyn.2004.03.003.

Tomita, H. 2008: New micorphysical schemes with five and six categories by diagnostic generation of cloud ice. J. Meteor. Soc. Japan, 86A, 121–142,

doi:10.2151/jmsj.86A.121.

Walsh, K. J. E., M. Fiorino, C. W. Landsea, and K. L. McInnes, 2007: Objectively determined resolution-dependent threshold criteria for the detection of tropical cyclones in climate models and reanalyses. J. Climate, 20, 2307–2314, doi:10.1175/JCLI4074.1.

Walsh, K., S. Lavender, E. Scoccimarro, and H. Murakami, 2013: resolution dependence of tropical cyclone formation in CMIP3 and finer resolution models. Climate Dyn., 40, 585–599, doi:10.1007/s00382-012-1298-z.

Walsh, K. J. E., and Coauthors, 2014: Hurricanes and climate: the U.S. CLIVAR working group on hurricanes. Bull. Amer. Meteor., 96, 997–1017, doi:10.1175/BAMS-D-13-00242.1.

Wang, Y., 2009: How do outer spiral rainbands affect tropical cyclone structure and intensity? J. Atmos. Sci., 66, 1250–1273, doi: 10.1175/2008JAS2737.1.

Weatherford, C. L., and W. M. Gray, 1988: Typhoon structure as revealed by aircraft reconnaissance. Part II: Structure variability. Mon. Wea. Rev., 116, 1044–1056, doi:10.1175/1520-0493(1988)116<1044:TSARBA>2.0.CO;2.

Wehner, M., Prabhat, K. A. Reed, D. Stone, W. D. Collins, and J. Bacmeister, 2015: Resolution dependence of future tropical cyclone projections of CAM5.1 in the U.S. CLIVAR Hurricane Working Group idealized configurations. J. Climate, 28, 3905–3925, doi:10.1175/JCLI-D-14-00311.1.

Welch, B. L., 1947: The generalization of ‘Student’s’ problem when several different population variances are involved, Biometrika, 34, 28–35, doi:10.1093/biomet/34.1-2.28.

Willoughby, H. E., 1979: Forced secondary circulations in hurricanes. J. Geophys. Res., 84, 3173–3183, doi: 10.1029/JC084iC06p03173.

Willoughby, H. E., R. W. R. Darling, M. E. Rahn, 2006: Parametric representation of primary hurricane vortex. Part II: a new family of sectionally continuous profiles. Mon. Wea. Rev., 134, 1102–1120, doi:10.1175/MWR3106.1.

Yamada, Y., K. Oouchi, M. Satoh, H. Tomita and W. Yanase, 2010: Projection of changes in tropical cyclone activity and cloud height due to greenhouse warming: global cloud-system-resolving approach. Geophys. Res. Lett., 37, L07709, doi:10.1029/2010GL042518.

Yamada, Y., and Satoh, M., 2013: Response of ice and liquid water paths of tropical cyclones to global warming simulated by a global nonhydrostatic model with explicit cloud microphysics. J. Climate, 26, 9931–9945. http://dx.doi.org/10.1175/JCLI-D-13-00182.1.

Yokoi, S., and Y. N. Takayabu, 2009: Multi-model projection of global warming impact on tropical cyclone genesis frequency over the western North Pacific. J. Meteor. Soc. Japan, 87, 525–538, doi:10.2151/jmsj.87.525.

Yokoi, S., Y. N. Takayabu, and J. C. L. Chan, 2009: Tropical cyclone genesis frequency over the western North Pacific simulated in medium-resolution coupled general circulation models. Climate Dyn., 33, 665–683, doi: 10.1007/s00382-009-0593-9.

Yokokawa, M., F. Shoji, A. Uno, M. Kurokawa, and T. Watanabe, 2011: The K computer: Japanese next-generation supercomputer development project. Proceedings of the 17th IEEE/ACM international symposium on low-power electronics and design, IEEE Press, 371–372. [Available online at http://dl.acm.org/citation.cfm?id=2016889]

Zhao, M., I. M. Held, S.-J. Lin, and G. A. Vecchi, 2009: Simulations of global hurricane climatology, interannual variability, and response to global warming using a 50-km resolution GCM. J. Climate, 22, 6653–6678. doi:10.1175/2009JCLI3049.1.